High-frequency nonlinear dynamics and optical chaos in a laser diode with phase-conjugated optical feedback

Guillaume Bouchez

Numéro national de thèse :
2022-CSUP-0002

CentraleSupélec

Ecole Doctorale C2MP

« Chimie Mécanique. Matériaux Physique » - n° 606

Laboratoire Matériaux Optiques, Photonique et Systèmes LMOPS EA-4423
Chaire Photonique

THÈSE DE DOCTORAT

Spécialité de doctorat : Physique

Soutenue le : 31 mars 2022

par :

Guillaume BOUCHEZ

High-frequency nonlinear dynamics and optical chaos in a laser diode with phase-conjugated optical feedback

Composition du jury :

Directeur de thèse :	Marc SCIAMANNA	Professeur (CentraleSupélec)
Co-directrice de thèse :	Delphine WOLFERSBERGER	Professeur (CentraleSupélec)
Rapporteurs :	Alexis FISCHER	Professeur (Université Sorbonne Paris-Nord)
	Massimo GIUDICI	Professeur (Université Côte d'Azur)
Examinateurs :	Ghaya BAILI	Docteur (Thales Research & Technology)
	Jordia TIANA-ALSINA	Docteur (Universitat de Barcelona)

Résumé en français

Le travail de cette thèse a consisté à montrer la richesse dynamique insoupçonnée d'une diode laser soumise à une rétroaction optique à conjugaison de phase (PCF, phase-conjugate feedback), en analysant à la fois numériquement et expérimentalement l'évolution de la puissance du laser, avec des vitesses de l'ordre de quelques dizaines de GHz.

D'abord, j'ai étudié le signal chaotique généré par un tel système, à la fois par des simulations et par l'expérience. Trois indicateurs étaient considérés : la bande-passante de chaos, c'est-à-dire l'étendue des fréquences sur lesquelles l'énergie du signal est répartie, la platitude spectrale, qui vérifie que l'énergie n'est pas concentrée sur une seule fréquence et l'entropie de permutation, qui étudie si des motifs se répètent dans le signal. J'ai observé que le chaos généré par un tel système était à la fois étendu sur un grand nombre de fréquences (bande passante de 30 GHz environ) et complexe (entropie de permutation jusqu'à 0,994), et sur une large plage de paramètres extérieurs au laser, dont la force de la rétroaction, le retard dans la rétroaction ou le courant d'alimentation du laser.

Ensuite, j'étudie les phénomènes périodiques très rapides précédemment observés avec le PCF, les modes de cavités externes (ECM, external cavity modes). Cette dynamique est marquée par une évolution périodique de la puissance du laser à une fréquence égale à un multiple de la fréquence associée au retard de la rétroaction. Nous étendons les précédentes études expérimentales en variant de nombreux paramètres du système, à savoir la force de la rétroaction, le retard dans la rétroaction et le courant d'alimentation du laser. En particulier, nous observons expérimentalement deux résultats qui avaient été prédits numériquement. D'une part, les ECM sont bistables, c'est-à-dire qu'avec les mêmes paramètres physiques ils peuvent avoir des fréquences différentes. D'autre part, nous montrons la fréquence des ECM ne change pas significativement si on change le retard sans changer les autres paramètres de l'expérience.

Enfin, nous étudions numériquement la possibilité de générer des ondes car-

rées avec une rétroaction optique à conjugaison de phase. Nous observons que la dynamique ainsi obtenue est semblable à celle obtenue avec une rétroaction optique non conjuguée en phase.

English summary

This thesis studied the dynamics of a laser diode subjected to a phase conjugate feedback (PCF). I analyzed both numerically and experimentally the evolution of the laser power, with speeds of the order of a few tens of GHz.

First, I studied the chaotic signal generated by such a system, both by simulations and by experiment. Three indicators were considered: the chaos bandwidth, i.e. the range of frequencies over which the energy of the signal is distributed, the spectral flatness, which verifies that the energy is not concentrated on a single frequency, and the permutation entropy, which studies whether patterns are repeated in the signal. I observed that the chaos generated by such a system was both broadband (bandwidth of about 30 GHz) and complex (permutation entropy up to 0.994). Such chaos was observed over a wide range of experimental parameters, including the feedback strength, the feedback delay, or the laser pump current.

Then, I study the very fast periodic phenomena previously observed with the PCF, the external cavity modes (ECM). The ECMs are regular self-pulsations of the laser power, at a frequency equal to a multiple of the frequency associated with the feedback delay. We extend previous experimental studies by varying the feedback strength, the feedback delay and the laser pump current. In particular, we observe experimentally two results that had only been numerically predicted. First, the ECMs are bistable, i.e. under the same experimental parameters they can have different frequencies. Secondly, we show that the frequency of the ECMs does not change significantly if we change the delay without varying the other parameters of the experiment.

Finally, we study numerically the generation of square waves with phase conjugate feedback. We observe that the resulting dynamics are similar to those obtained with non-phase conjugate optical feedback.

Remerciements

Je tiens à remercier particulièrement mon directeur et ma co-directrice de thèse, Marc Sciamanna et Delphine Wolfersberger, qui m'ont fait confiance et avec qui j'ai avancé tout le long de ma thèse.

J'ai une pensée pour tous mes anciens camarades doctorants, Chi-Hak Uy, Thomas Bouchet, Florian Denis, Jérémy Vatin, Nacera Bouldja et Yaya Doumbia, ainsi que les post-doctorants Stefan Bittner et Tushar Malica et mon stagiaire Neco Kriel. Nous avons eu de belles discussions, qu'elles soient scientifiques ou sociales. Du point de vue des résultats présentés dans cette thèse, je remercie Tushar et Neco avec qui j'ai pu travailler directement, ainsi que Stefan et Chi-Hak pour leurs coups de mains techniques. Je remercie également Mario, sans qui je n'aurais rien pu faire sur ma table d'expérience. Je remercie enfin Germano Montemezzani, Damien Rontani et Nicolas Marsal.

Je tiens également à remercier les différents collègue du campus de Metz, et en particulier Gilles Belin ainsi que les responsables administratives, qui ont toujours su m'aider, chacun dans son domaine.

Et je vous souhaite bonne chance, à vous qui lirez cette thèse pour continuer les recherches sur la dynamique des diodes lasers soumises à une rétroaction optique à conjugaison de phase.

Table of Contents

Introduction

The realization of the first lasers, or light amplification by stimulated emission of radiation, in 1960 opened new perspectives for signal processing and communications. The semiconductor laser, introduced in 1962, allowed breakthroughs, e.g. in telecommunications and sensing.

Our study is concerned with one aspect of this vast field of study, namely the non-linear dynamics obtained with semiconductor lasers. In particular, a laser diode destabilized by optical feedback can generate chaos, i.e. have an evolution that is both deterministic and unpredictable because it is sensitive to initial conditions. Such a chaotic signal allows for example encrypted telecommunications, more accurate sensors, or the generation of random numbers at very high rate.

More precisely, we study here a laser diode subjected to a phase conjugate feedback. The phase conjugate feedback was first seen as a way either to self-align feedback in a laser or rather to stabilize the laser output. However, the studies conducted since the introduction of phase conjugation have also shown a very important and new dynamic richness. This thesis is a continuation of this research.

We will present the state of the art in more detail in chapter 1. We will briefly describe the operation of a laser diode and the study of its nonlinearity, in particular when subjected to conventional optical feedback. We will then present the particularities induced by the phase conjugate feedback, then we will introduce the objectives of this thesis.

In chapter 2, we will present the experimental setup used during the thesis. We will first deal with the question of the practical realization of a phase

conjugate mirror to obtain a phase conjugate optical feedback. After a general approach, we will present in more detail the mirror used in this thesis, a self-pumped phase conjugate mirror realized in a barium titanate crystal. Then, we will present the characteristics of the lasers used during this thesis. The chapter will end with the description of the different measuring devices used.

Chapter 3 and 4 will study the chaos generated with the PCF through three indicators of its complexity and speed: the chaos bandwidth, the spectral flatness and the permutation entropy. Chapter 5 will introduce the study of the external cavity modes, the self-pulsed dynamics specific to the PCF. Finally, chapter 6 studies a variant of the PCF, the polarization-rotated phase conjugate feedback.

Chapter 7 will conclude this study and give several perspectives for future work.

Chapter 1

Background and motivations

This first chapter is an introduction into the subject of this thesis, i.e. the nonlinear dynamics of a laser diode subjected to phase-conjugate feedback.

First, section 1.1 introduces one of the most commonly used design in the world, the laser, especially the laser diode. Section 1.2 presents the background concepts necessary for the understanding of this thesis: the nonlinear dynamics in laser diodes. After a general introduction to non-linear dynamics and chaos, it presents an overview of the non-linear dynamics in laser diodes. Then, section 1.3 summaries the previous studies about the behavior of a laser under phase-conjugate feedback. Last, section 1.5 explains the objectives of the work presented in this thesis.

1.1 Laser

1.1.1 Principle

First, we start by a definition of the laser.

Laser is an acronym for Light Amplification by Stimulated Emissions of Radiations. This name is actually of good summary of its principle: the emission of radiations is stimulated to generate amplified light. That said, we have to be more precise. Light is both a wave, characterized by its wavelength λ and a set

of particles called photons, characterized by their energy E. Quantum physics told us that both the energy of the photons and the energy of the matter are quantified. In the case of the photon, its wavelength λ is related to its energy E through the following equation [1, 2]:

$$E = h\frac{c}{\lambda} \tag{1.1}$$

where h is the Planck constant and c the speed of light.

When light and matter interacts, three phenomena can occur:

- absorption: a photon is absorbed by the matter. The later transits from a low energy level to a higher energy level (excited level), the difference of energy being equal to the energy of the photon.
- spontaneous emission: it is the inverse phenomenon. The matter transits from an excited level to a lower energy level and a photon is emitted. Its energy is equal to the difference of energy between the concerned energy levels of the matter.
- stimulated emission: the matter interacts with an incoming photon. The matter transits from an excited level to a lower energy level, another photon being generated, with the same energy, polarization and direction than the incoming photon. To obtain that phenomenon, the difference between the concerned energy states of the matter must be close to the energy of the incoming photon.

To explain that more clearly, we illustrate in Fig. 1.1 the example of an atom with two levels of energy E_1 and $E_2 > E_1$. In the case of absorption (a), the atom absorb an incident photon of wavelength $\lambda = \frac{hc}{E_2 - E_1}$ and an electron moves from E_1 to E_2 energy levels. In spontaneous emission (b), the atom is at the energy level E_2. Its energy spontaneously reduces to E_1 and it emits a photon of wavelength $\lambda = \frac{hc}{E_2 - E_1}$. For stimulated emission, a photon, with wavelength $\lambda = \frac{hc}{E_2 - E_1}$, interacts with an excited atom, with energy E_2. The energy of the atom falls to E_1 and a new photon is emitted with a wavelength λ', similar to λ.

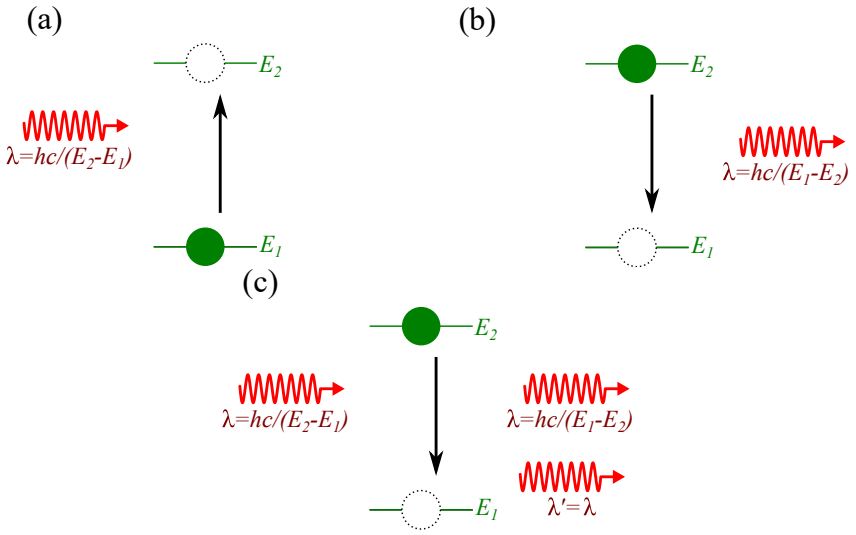

Figure 1.1: Principle of (a) absorption, (b) spontaneous emission and (c) stimulated emission, in the case of a two levels atom (energy E_1 and E_2).

Stimulated emission was first proposed by Einstein in 1916 [3] and experimentally observed in 1928 [4]. A cascade of stimulated emissions can create an amplification of light [5].

However, to use the "stimulated emission of radiation" to amplify light, the matter must be set initially in an excited state. That condition is called "inversion of population". To achieve it, the amplifying medium is pumped, either by another light beam (optical pump) or by an electrical current (electrical pump). The energy added by the pump has to be superior to the losses of energy of the atoms [5].

To ensure that all the photons have the same energy and directions, it is necessary to have a medium that control their wavelength. This is achieved using a cavity. Such cavity is generally made of two mirrors, with one of them being semi-transparent. That permits photons to leave the laser from that extremity.

A laser is therefore in practice made of a gain medium in a cavity, with an external pump. The first experimental laser was achieved in 1960 by Theodore Maiman. To pumped a cavity made of a ruby rod and silver reflectors, he used a flashlamp coiled around the ruby rod [6].

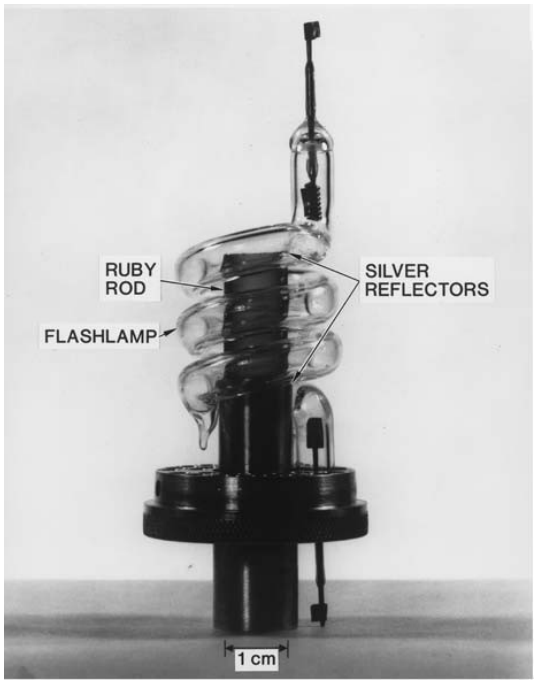

Figure 1.2: The first laser created by Theodore Maiman. It is made a ruby rod pumped by the light from a flashlamp. The cavity is delimited by silver reflectors. Photograph taken from Ref. [5].

1.1.2 Laser diodes

After the first ruby laser was demonstrated in 1960, the laser diode was developed during the following years.

A laser diode is a specific type of laser, whose gain medium is made of semiconductor materials. Therefore, laser diode and semiconductor laser are interchangeable expressions.

1.1.2.1 Semiconductor materials as laser amplification mediums

In semiconductors materials, such as silicon or gallium arsenide, the electrons can occupy low energy states in the conduction band and high energy states in the valence band. A bandgap separates these two possible energy bands. While at zero temperature all the electrons stay in the valence band, bandgap of semiconductors is short enough so that electrons can move to the conduction

band at room temperature. When electrons are in the conduction band, they are free charges, as are the electrons in metals. On the other side, an electron in the conduction band lead to a "hole" in the valence band. That missing electron is mobile, as an electron in the valence band can fill the hole but, in doing so, creates a new one as its place becomes vacant.

A semi-conductor can be doped by the addition of impurities. It is performed by introducing elements with superior or inferior numbers of valence electrons. For instance, adding Phosphorus (5 valence electrons) to a Silicon (4 valence electrons) lattice adds free electrons in the semiconductor. Similarly, adding Boron (3 valence electrons) to a Silicon lattice creates a lack of electrons, i.e. holes. Semiconductors with excess of holes are known as "p", for positive, while "n", or negative, indicates an excess of electrons.

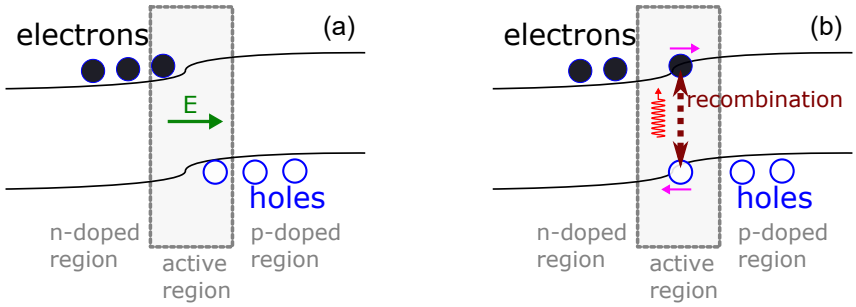

Figure 1.3: Principle of the p-n junction. (a) At thermodynamic equilibrium, the electrons and the holes are confined around the active region. A local electric field E (green arrow) prevent further movement of the charges. (b) If a bias current is applied, the electrons and the holes move into the active region (purple arrows), where they recombine.

When p-type and n-type semiconductors are adjacent, a p-n junction is created. At equilibrium (Fig. 1.3 (a)), supernumerary holes and electrons recombine in the so-called "active region", the frontier between the p-doped and n-doped zones. That region stops further diffusion because of the difference of potential between the holes in the p-doped zone and the electrons in the n-doped zone. Applying a bias voltage (Fig. 1.3 (b)) reduces the energy barrier between the p and n regions and induces an additional drifting motion of the supernumerary carriers into the opposite part, hence boosting the carrier

recombinations and photon emissions.

The first semiconductor laser was achieved in 1962 by Robert Hall and the General Electric Research Laboratory [7]. They used direct transition in gallium arsenide immersed in liquid nitrogen [8]. However, the carriers in such laser were hardly confined at room temperature. Therefore, high pump currents were necessary to maintien stimulated emission [9].

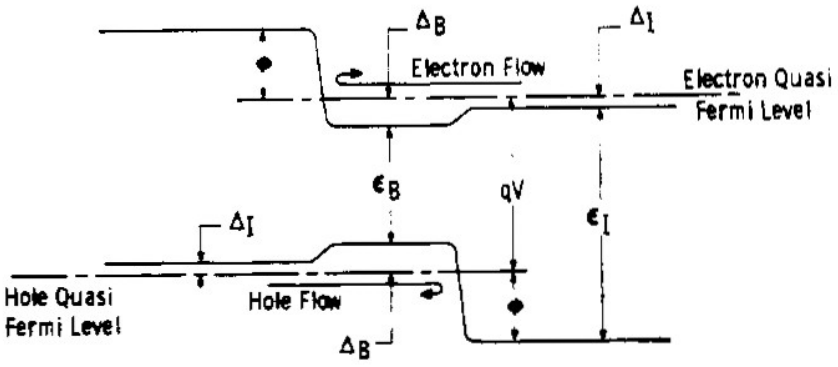

Figure 1.4: Kroemer's figure of the energy diagram in a double hetero-junction [10].

Herbret Kroemer proposed a new solution in 1963: the double hetero-structure (Fig. 1.4). The device is now made of three zones: two highly doped regions, typically p+ and n+, and a thinner region with a lower bandgap. The difference of energy gaps between the zones enables the confinement of the carriers in the active region [10]. The active region also acts as a longitudinal wave-guide to confine the light in a single direction since its lower energy bandgap yields also a higher refractive index than the surrounding semiconductor material [9].

1.1.2.2 Realisation of laser diodes

Typical laser diode are made with a Fabry-Pérot cavity. It is constituted by two partially-reflecting mirrors, placed at the two sides of the cavity (Fig. 1.5 (a)). A laser with such a cavity undergoes multimode operations: the photons in the cavity oscillate simultaneously at various wavelengths. The frequencies of the photon are multiples of the inverse of the round-trip time of the cavity.

Therefore, the Fabry-Pérot laser has a free spectral range $\Delta\nu$ equal to:

$$\Delta\nu = \frac{c}{n_g L} \tag{1.2}$$

where n_g is the group index of the active medium and L the round-trip length of the cavity. Generally, one of the mirrors has a reflectivity close to 100%, in order to have only one exit facet.

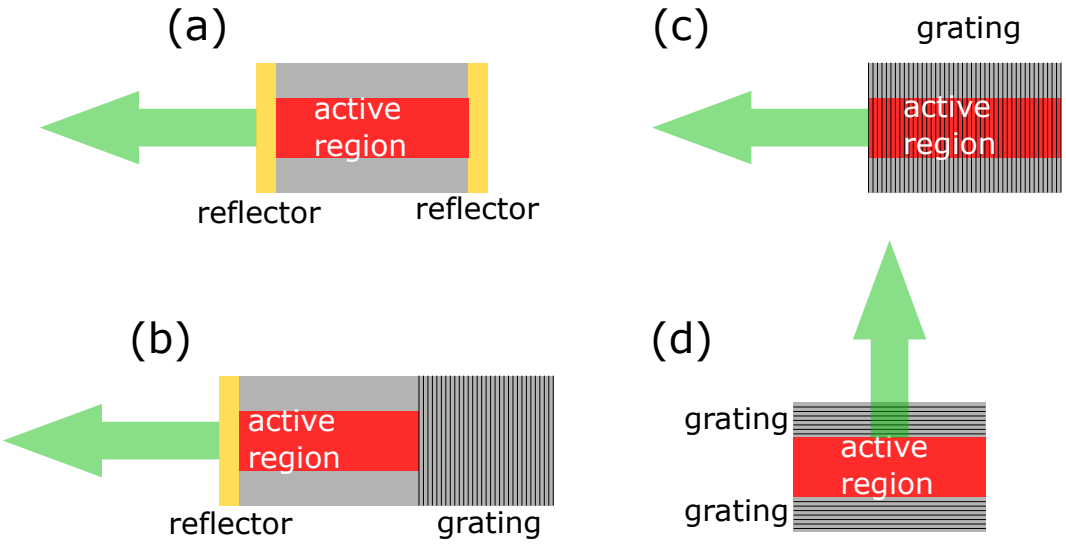

Figure 1.5: Four types of laser diodes: (a) Fabry-Pérot, (b) DBR laser, (c) DFB laser and (d) VCSEL.

Other types of semiconductor laser have been developed. Three are presented on Fig. 1.5:

- distributed Bragg reflector (DBR) laser (Fig. 1.5 (b)). One of the mirror is replaced by a Bragg reflector, i.e. a grating region. That grating region forces the selection of only one wavelength, directly related to its grating period. Therefore, DBR lasers have monochromatic emission.
- distributed feedback (DFB) laser (Fig. 1.5 (c)). It is similar to DBR laser but the grating is placed in the active region. It is considered as highly stable and monochromatic.
- vertical-cavity surface-emitting laser (VCSELs) (Fig. 1.5 (d)). In VCSELs, the distributed Bragg reflectors are placed on top and bottom of the

active region. Therefore, the emission is parallel to the semiconductor growth direction. Such configuration is useful in commercial application of semi-conductor lasers: lasers can be tested directly on the silicon wafer and their integration is easier [11]. However, the active region of VCSEL has typically a circular symmetry and an equal spatial distribution of the gain, hence making no preference in the polarization of the light: the light often switches between two possible linearly polarized orthogonal polarization states [12, 13]. To differenciate from the VCSELs, the laser diodes that emit parallel to the active region are named edge-emitting laser diodes or EELs.

Laser diodes are used in various fields. They can be massively produced and need low currents to operate [5]. These advantages are particularly true with VCSELs [14].

We give three examples of applications of laser diodes:

- In 1966, Kao (later recipient of the Nobel Prize in 2009) and Hockham proposed to use optical fibers as waveguide. They tested their hypothesis with two lasers, an helium neon gas laser and a gallium arsenide laser diode [15]. Laser diodes were soon preferred because of their low absorption in silicon at their wavelength of emission. The boom of Internet in the 1990s led to the development of highly effective laser diodes. The transparency of a standard optical fiber is maximized around 1.5 μm and telecommunication laser diodes operate in that range of wavelength [5].

- In lidars, i.e. sensors using light to determine ranges and spatial distribution of elements [16], laser diodes enable eye-safe, low-cost and small size lidars [17, 18]. Lasers are either emitting short pulses or a modulated continuous-wave. In that later case, laser diodes are easy to modulate through their pump current [17].

- Laser diodes can also be used to sense the presence of gas. The possibility to tune their emitting wavelength with the temperature led to the development of gas sensors based on a temperature-controlled laser diode [19–21].

Other applications of laser diodes require a peculiar modulation of the laser diode dynamics, to make them chaotic.

1.2 Non-linear dynamics and chaos in laser diodes

1.2.1 From lasers to non-linear dynamics and chaos

Since the start of the modern science, base on mathematical equations in the 17th century, modelling the physical mechanisms with equations seemingly enabled a perfect prediction of the future. The first example was the gravitation mechanism, that describes how a planet orbits around the sun. However, a question remains in that case: what will happen if a third astronomical body was added? In 1890, responding to a challenge proposed by King Oscar II of Sweden, Henri Poincaré concluded that no simple solution can be found and that a small perturbation in the initial conditions can lead to completely different planet trajectories. As an anecdote, Poincaré made a mistake in his memoir. He admitted it but the mathematician that publicly validated his work discreetly searched for all the erroneous copies of the memoir to destroy them, to protect his own reputation until the new memoir was printed [22].

While these results can be considered as the first statements of non-linear dynamics, the next important step was only achieved in the 1960s. The development of computer sciences then enabled the calculation of the dynamical evolution of complicated deterministic systems using integration methods. Lorenz, a weather researcher, tried to simulate atmospheric dynamics with three simple coupled equations. He observed not only "complex" non periodic dynamical states but also very different dynamics when modifying the initial conditions of the numerical simulations. First published in 1963 under the name *Deterministic Nonperiodic Flow* [23], his work was recognized in 1972 when he presented a conference talk entitled *Does the Flap of a Butterfly's Wings in Brazil Set Off a Tornado in Texas?* It was the birth of chaos theory.

Chaos is generally defined as irregular (a-periodic) fluctuations governed by

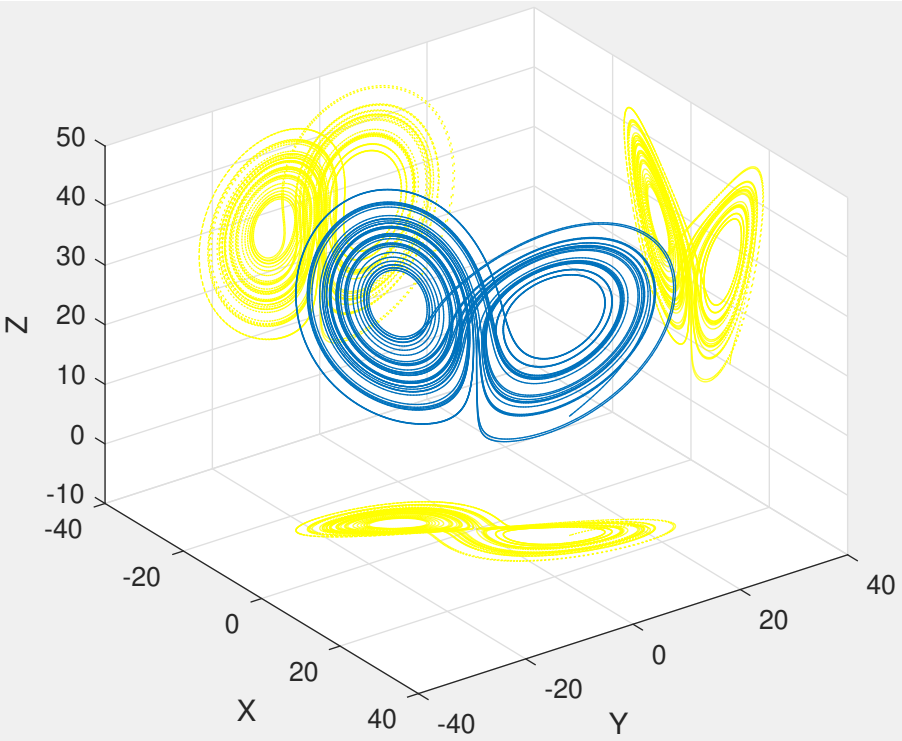

Figure 1.6: Phase-space trajectory of the Lorenz system. The projections into the three two-parameters planes are plotted in yellow.

a deterministic rule [24]. Additionally, chaotic systems show a strange attractor in the phase-space of the state variables of the system. The trajectory of the temporal evolution of the variables, although complex, stay in a bounded region. The attractor of the Lorenz system under common parameters initialization [24, 25] is presented in Fig. 1.6. The trajectory turns here around two points but, contrary to a periodic trajectory, it never passes twice by the same dynamical point. The strange property of such attractor has later been characterized as a mathematical object of non-integer, also called fractal, dimension [25].

Lasers were first considered to be far from such realities. However, in 1975, Haken observed that the general equations used to describe a laser were similar to the Lorenz equations [26]. While Haken's chaos only occurs in specific lasers, further studies observed that chaos was observable in many types of lasers, including the laser diodes [25, 27].

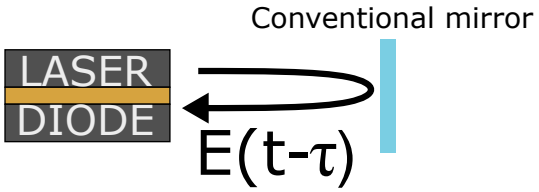

Figure 1.7: Schematic of a COF experiment. $E(t-\tau)$ is the delayed laser output electric field.

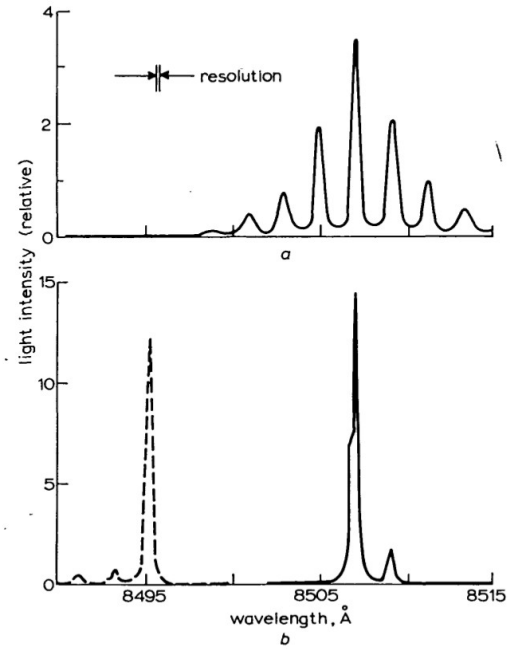

Figure 1.8: Spectra of a laser diode under COF. The spectrum in (a) is under limited feedback, the solide line in (b) is the spectrum with higher feedback strength and the dashed line in (b) the spectrum of the free-running laser. Figure taken from Ref. [28].

Soon after the invention of the laser diode, it was observed that its response to a change in its drive current was nonlinear [29]. In 1969, Broom reported a new phenomena: a laser diode was destabilized when its output light was coupled back into its internal cavity by a mirror [28]. Such feedback will be thereafter named conventional optical feedback or COF (see Fig. 1.7). The optical spectra of Broom's laser is presented Fig. 1.8. Under moderate COF, sidebands appear around the central peak, as shown Fig. 1.8 (a). At higher

feedback strength, as presented in the solide line of Fig. 1.8 (b).

The observed side-bands in Ref. [28] were identified as an udamping of the relaxation oscillations (ROs), a frequency related to the competition between the decay rate of the carriers and the decay rate of the photons in the laser diode cavity [25]. Then, observations show that the undamping of the ROs lead to chaotic dynamics [30].

1.2.2 The Lang-Kobayashi equations

The numerical reproduction of these observations was unclear until Lang and Kobayashi proposed in 1980 a model to describe the behavior of a single-mode laser diode under weak COF. The equations give the evolution of $E(t)e^{i\Omega t}$ the complex electric field of the laser and $N(t)$ the density of excited carriers [31]:

$$\frac{d}{dt}E(t)e^{i\Omega t} = \left\{ i\omega(N) + \frac{1}{2}(G(N) - \Gamma_0) \right\} E(t)e^{i\Omega t} + \kappa E(t-\tau)e^{i\Omega(t-\tau)} \tag{1.3}$$

$$\frac{d}{dt}N(t) = -\gamma N - G(N)|E(t)|^2 + P \tag{1.4}$$

where Ω is the laser oscillation frequency, $\omega(N)$ is the resonant frequency of the laser cavity longitudinal mode, $G(N)$ is the gain, Γ_0 is the losses in the laser cavity, γ the inverse spontaneous lifetime of the excited carriers and P is the injection rate of excited carriers, expressed as a density. τ is the round-trip time between the laser and the external mirror and κ is the coefficient defined as [31]:

$$\kappa = \frac{c}{2\eta l_D}a = \frac{a}{\tau_{in}} \tag{1.5}$$

where a is the coupling strength between the light in the laser and in the external cavity. c is the speed of light, η the index of light in the laser cavity, l_D the length of that cavity and therefore κ is inversely proportional to τ_{in}, the round-trip time in the laser cavity.

These equations were soon modified with a new parameter of the laser diodes: the linewidth enhancement factor, or α. It was discovered to explain

larger linewidth of the laser diode when compared with other lasers [32]. Having a typical value between 3 and 7 for laser diodes, it enhances the linewidth by a factor of $1+\alpha^2$ but it also a key parameter of the modulation properties and of the dynamics of laser diodes [33].

Close to the threshold, the gain $G(N)$ is also expressed as linearly dependent to the carriers density [33]:

$$G(N) = G_N(N - N_0) \tag{1.6}$$

where G_N is the linear gain and N_0 the carriers density at transparency.

If the laser operates far from threshold, saturation has to be considered and the gain is now [33]:

$$G(N) = \frac{G_N}{1+\epsilon|E|^2}(N - N_0) \tag{1.7}$$

where ϵ is the coefficient gain saturation.

Therefore, the Lang-Kobayashi equations write as follows [24], once we set $\mathbf{E}(t) = E(t)e^{i\Omega t}$:

$$\frac{d}{dt}\mathbf{E}(t) = \left[\frac{1+i\alpha}{2}\left\{G_(N) - \frac{1}{\tau_p}\right\} + i\omega(N)\right]\mathbf{E}(t) + \kappa\mathbf{E}(t-\tau) \tag{1.8}$$

$$\frac{d}{dt}N(t) = P - \frac{n}{\tau_e} - G_(N)|\mathbf{E}(t)|^2 \tag{1.9}$$

where $\tau_p = \frac{1}{\Gamma_0}$ is the photon lifetime and $\tau_e = \frac{1}{\gamma}$ is the carrier lifetime.

Since the dynamics of the electric field is much slower than the variations of the optical frequency, we can decompose the electric field into a slow complex electric field $E_s(t)$ and a fast optical carrier $e^{i\omega t}$ (ω is considered to be constant over time) [24]:

$$\mathbf{E(t)} = E_s(t)e^{i\omega t} \tag{1.10}$$

Equation 1.8 transforms into [24]:

$$\begin{aligned}\frac{d}{dt}E_s(t)e^{i\omega t} + i\omega E_s e^{i\omega t} \\ = \left[\frac{1+i\alpha}{2}\left\{G_(N) - \frac{1}{\tau_p}\right\} + i\omega\right]E_s(t)e^{i\omega t} + \kappa E_s(t-\tau)e^{i\omega(t-\tau)}\end{aligned} \tag{1.11}$$

Dividing each term by $e^{i\omega t}$ and adding $-i\omega E_s$ to both sides gives the standard form of the Lang-Kobayashi equations [24, 33, 34]:

$$\frac{d}{dt}E_s = \frac{1+i\alpha}{2}\left\{G_(N) - \frac{1}{\tau_p}\right\}E_s(t) + \kappa E_s(t-\tau)e^{-i\omega\tau} \tag{1.12}$$

$$\frac{d}{dt}N(t) = P - \frac{n}{\tau_e} - G_(N)|E_s(t)|^2 \tag{1.13}$$

The system can be seen as a reservoir of excited carriers coupled to an optical emitter with delay. Carriers are injected by the pump $+P$ term in equation 1.13 but spontaneously decay, hence the $-\frac{n}{\tau_e}$ term. Other are destroyed when they recombine to create photons with a gain G(N): $-G_(N)|E_s|^2$. While some photons decay a the rate $\frac{1}{\tau_p}$, photons are created, hence the $\frac{1}{2}\left\{G(N) - \frac{1}{\tau_p}\right\}E_s(t)$ term in equation 1.12. The $+\kappa E_s(t-\tau)e^{-i\omega\tau}$ term considers the energy added into the laser cavity by the delayed feedback.

The Lang-Koyashi equations were later modify to apply to many systems with conventional laser diodes, such as, for instance, multimode lasers [35], injection of the output light of a laser diode into another laser diode [36] or optical feedback with rotation of the polarization [37].

1.2.3 The dynamical scenario of a laser with conventional optical feedback

The dynamics of the laser diode with conventional optical feedback was extensively studied, both by experiments and simulations. The dynamics were understood as a competition between the relaxation oscillation frequency f_{RO} of the laser and the frequency f_{EC} of the external cavity [25].

The relaxation oscillation frequency is given by [24]:

$$f_{RO} = \frac{1}{2\pi}\sqrt{\frac{P/P_{th}-1}{\tau_p\tau_e}} \tag{1.14}$$

where P is the carriers pump, P_{th} the pump at threshold, τ_p the photon lifetime and τ_e the carriers lifetime. f_{RO} is of the order of a few GHz for standard laser diodes.

The frequency of the external cavity is the inverse of the external time delay τ:

$$f_{EC} = \frac{1}{\tau} = \frac{c}{2L_{ext}} \tag{1.15}$$

where L_{ext} is the distance between the laser and the mirror.

The dynamics of the system is different depending if $f_{EC} \ll f_{RO}$ ("short cavity") or $f_{EC} \gg f_{RO}$ ("long cavity") [25].

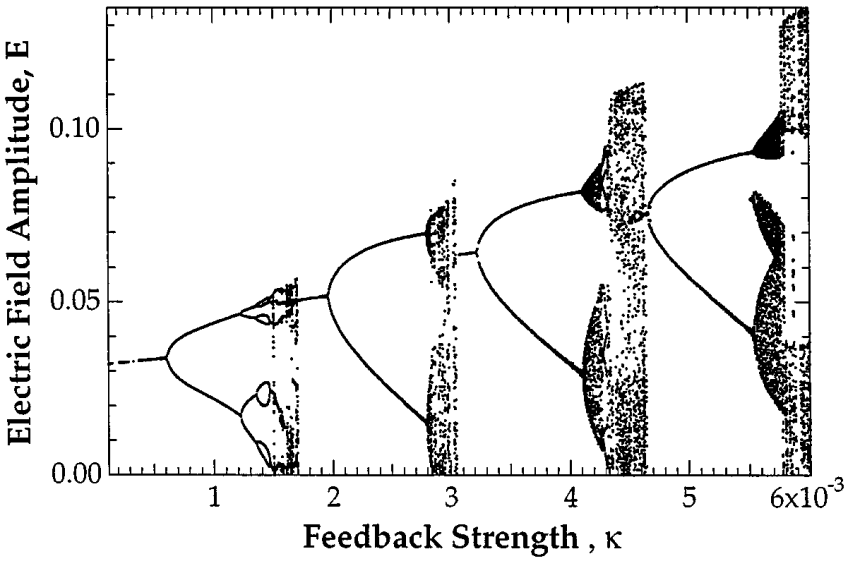

Figure 1.9: Numerically computed bifurcation diagram versus the feedback strength for a laser under weak optical feedback. Figure taken from Ref. [34].

In Fig. 1.9, we present the bifurcation diagram of the output electric field of a laser under conventional optical feedback in the long cavity configuration, versus the feedback strength κ. The laser destabilizes from $\kappa > 6 \times 10^{-4}$ through the undamping of the relaxation oscillations. Then, it becomes chaotic via period-doubling as the feedback strength is increased. From $\kappa = 1.7 \times 10^{-3}$, the dynamics stabilizes again. A study of its optical spectrum shows that the laser optical frequency settles at multiples of the inverse of the round-trip time of the external cavity [34]. As the feedback strength increases, the laser undergoes a new Hopf bifurcation at $\kappa = 2 \times 10^{-3}$, which leads to chaos via a quasi-periodicity. The laser follows several bifurcation cascades on successive external cavity modes.

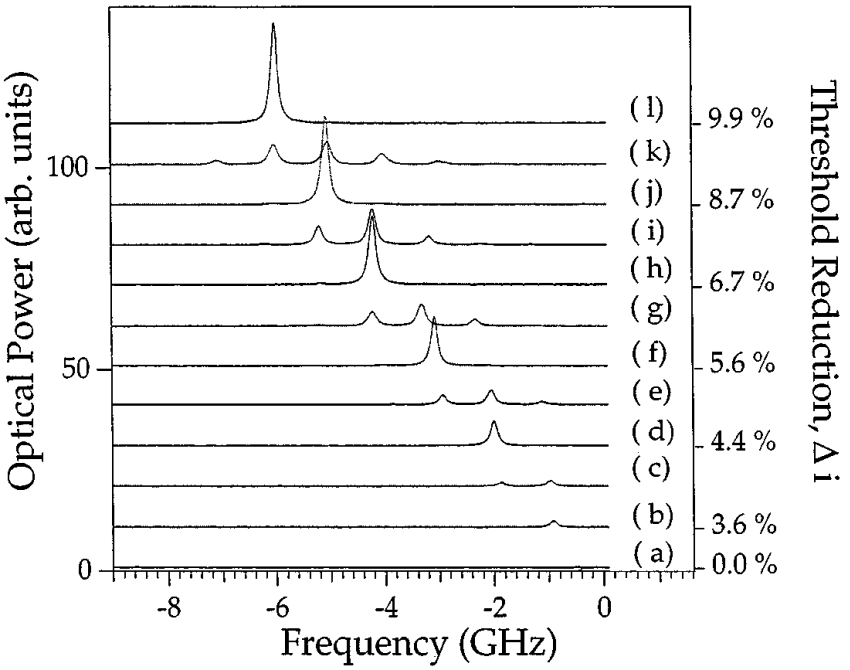

Figure 1.10: Experimental optical spectra of a laser subjected to COF. The feedback strength, measured by using the threshold reduction, increases from (a) to (l). Figure taken from Ref. [34].

This cascade of external cavity modes can be observed experimentally, as shown in Fig. 1.10, which was also taken from Ref. [34]. Figure 1.10 presents the experimental optical spectra of a laser subjected to COF, for increasing feedback strengths from (a) to (l). At low feedback strength (Fig. 1.10 (b)), the laser output spectrum is narrow: the laser output power is steady. Then, Fig. 1.10 (c) shows sidebands at f_{RO} around the central peak: the laser output power has undamped relaxation oscillations. The spectra b, d, f, h, j and l in Fig. 1.10 show the external cavity modes, separated by unstable dynamics shown in the spectra c, e, g, j and l in Fig. 1.10 [34].

1.3 Dynamics of laser diodes with phase-conjugate feedback

Conventional optical feedback requires a good alignment of the mirror to couple the feedback beam into the laser cavity. Therefore, a new solution was proposed, using phase-conjugate feedback. A phase-conjugate feedback is a counterpropagating beam that follows the inverse propagation of the original beam. The feedback is therefore self-aligned.

Phase-conjugation, and how it can be generated in a phase-conjugate mirror (PCM), will be extensively described in chapter 2. However, we will now describe how phase-conjugate feedback creates many different dynamical behaviors on laser diodes.

1.3.1 Equations

The first numerical study of the dynamics of a laser with phase-conjugate feedback was a modification of the standard Lang-Kobayashi equations [38]:

$$\dot{E}(t) = i(\omega_0 - \Omega)E(t) + \frac{1}{2}\left(G - \frac{1}{\tau_p}\right)(1 - i\alpha)E(t) + \kappa E^*(t-\tau)exp(i\phi_{PCM}) \tag{1.16}$$

$$\dot{N}(t) = \frac{I}{q} - \frac{N(t)}{\tau_e} - G|E(t)|^2 \tag{1.17}$$

where $E(t)$ is the optical field (normalized such that $|E(t)|^2$ represents the number of photons in the cavity), $E*(t)$ is the phase-conjugation of $E(t)$, N(t) the electron population, ω_0 the optical frequency of the laser with feedback, Ω the optical frequency of the free-running laser, $G = G_N(N(t) - N_0)$ the linear optical gain, N_0 the population inversion at transparency, τ_p the photon lifetime, α the linewidth enhancement factor, I the injection current, q the charge of an electron, τ_e the electron lifetime. κ is the feedback rate, τ is the round-trip time in the external cavity and ϕ_{PCM} is a possible phase-shift in the PCM.

Since the feedback field is the phase-conjugate of the output field, there is no $\omega_0\tau$ phase-shift in the feedback term as in equation 1.12 [38].

Previous studies [38–43] have considered a detuning in the feedback field. It simulates the case of an external pump applied to the phase-conjugate mirror, whose optical frequency is possibly different from the solitary laser frequency.

Subsequent studies also added non-linear gain saturation [41, 44–46]:

$$\dot{E}(t) = i(\omega_0 - \Omega)E(t) + \frac{1}{2}\left[\left(G' - \frac{1}{\tau_p}\right) - i\alpha\left(G_N[N(t) - N_0] - \frac{1}{\tau_p}\right)\right]E(t) + \kappa E^*(t-\tau)exp(i\phi_{PCM}) \tag{1.18}$$

$$\dot{N}(t) = \frac{I}{q} - \frac{N(t)}{\tau_e} - G'|E(t)|^2 \tag{1.19}$$

with

$$G' = \frac{G_N}{1 - \epsilon|E(t)|^2}(N(t) - N_0) \tag{1.20}$$

where ϵ is the non-linear gain coefficient.

Using a self-pumped PCM (see section 2.1.3), the four-wave mixing is frequency-degenerated (no detuning), hence there is no shift in the wavelength [47]. The equations therefore become, considering also that the phase-shift ϕ_{PCM} can be set to 0, and if the gain is linear [48]:

$$\dot{E} = \frac{1 + i\alpha}{2}\left[G_N(N - N_0) - \frac{1}{\tau_p}\right]E + \kappa E^*(t-\tau) \tag{1.21}$$

$$\dot{N} = \frac{I}{q} - \frac{N}{\tau_e} - G_N(N - N_0)|E|^2 \tag{1.22}$$

To obtain dimensionless equations, we can introduce the following variables [48],

$$t' = \frac{t}{\tau_p} \tag{1.23}$$

$$Y = \sqrt{\frac{\tau_e G_N}{2}}E \tag{1.24}$$

$$Z = \frac{G_N \tau_p}{2}(N - N - sol) \tag{1.25}$$

with $N_{sol} = N_0 + \frac{1}{G_N \tau_p}$ the population inversion of the solitary laser. All the parameters expressed as a time are also normalized by τ_p

$$\gamma = \kappa \tau_p \tag{1.26}$$

$$\theta = \frac{\tau}{\tau_p} \tag{1.27}$$

$$T = \frac{\tau_e}{\tau_p} \tag{1.28}$$

Last, the pump is reinterpreted as a new parameter P:

$$P = \frac{G_N \tau_p \tau_e}{2} \left(\frac{I - I_{th}}{q} \right) \tag{1.29}$$

with $I_{th} = \frac{N_{sol} q}{\tau_e}$ the threshold current.

Equations 1.21 and 1.22 can now be written in a dimensionless form [48]:

$$\frac{d}{dt'} Y = (1 + i\alpha) ZY + \gamma Y^*(t' - \theta) \tag{1.30}$$

$$T \frac{d}{dt'} Z = P - Z - (1 + 2Z)|Y|^2 \tag{1.31}$$

If f_{RO} is normalized, equation 1.14 can be written as [49]:

$$f_{RO} = \frac{1}{2\pi} \sqrt{\frac{2P}{T}} \tag{1.32}$$

In the case of finite depth-penetration length in the PCM, i.e. if the PCM does not have an instantaneous response [50], the feedback field U is filtered by a parameter τ_r, related to the times it takes for the light to penetrate the PCM. If we assume that τ_r is normalized by τ_p, the equations now reads as [51]:

$$\frac{d}{dt'} Y = (1 + i\alpha) ZY + \gamma \tag{1.33}$$

$$T \frac{d}{dt'} Z = P - Z - (1 + 2Z)|Y|^2 \tag{1.34}$$

$$\tau_r \frac{d}{dt'} U = Y^*(t' - \theta) - U \tag{1.35}$$

1.3.2 Bifurcation scenario

Equations 1.33 to 1.35 are simulated with parameters $P = 0.6016$, $\alpha = 2$, $\tau_r = 50$, $\theta = 1143$ and $T = 1200$ [52]. Four time series at different values of γ are shown in Fig. 1.11 and the corresponding bifurcation diagram is show in Fig. 1.12.

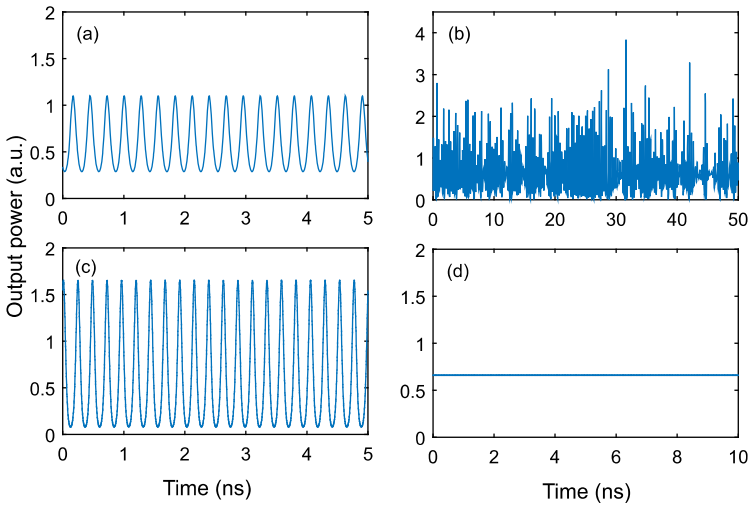

Figure 1.11: Simulated time traces of a PCF laser with filtered feedback, obtained from equations 1.33 to 1.35. (a) is γ=0.0012, (b) at $\gamma = 0.008$, (c) at $\gamma =$ 0.0168 and (d) at γ =0.0506. Other parameters are $P = 0.6016$, $\alpha = 2$, $\tau_r = 50$, $\theta = 1143$ and $T = 1200$. Figure taken from Ref. [52].

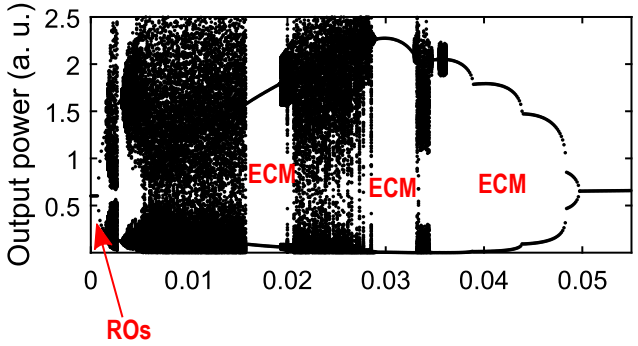

Figure 1.12: Simulated bifurcation diagram of a PCF laser with filtered feedback, obtained from equations 1.33 to 1.35. Parameters are the ones of Fig. 1.11. Figure taken from Ref. [52].

At low feedback strength, the laser destabilizes into the relaxation oscillations [52–54], as in conventional feedback [25]. An example of simulated undamped oscillations are presented in Fig. 1.11 (a).

When the feedback strength is increased, chaos appears from the undamping of the relaxation oscillations [52–55], as illustrated in Fig. 1.11 (b). However, the PCF seems more prone to chaos [55] and phase-conjugate feedback chaotic

dynamics encompass larger bandwidths than the chaos obtained with conventional feedback [56].

For still larger feedback strength, the system shows qualitatively different dynamics, shown in Fig. 1.11 (c). The output power oscillates at a frequency equal to a multiple of the inverse of the output roundtrip time and this frequency is often higher than the relaxation oscillation frequency [52, 54, 57]. Analogous to the external cavity modes of the conventional feedback, these latter states are named external cavity modes (ECMs) [58].

At higher values of feedback strength, early studies predicted a restabilization of the laser [43]. That result was observed in 2002 with a self-pumped phase-conjugate mirror [59]. It is worth noting that the authors observed restabilization but no ECMs.

Restabilization after ECM crisis was reported by our group in 2017 [52]. That latter study led us to use a model that took into account the penetration time into the crystal [50], presented in equations 1.33-1.35. The restabilization was analytically determined to be from an inverse Hopf bifurcation on an ECM solution [51].

1.4 Other PCF systems

We have described the behavior of the laser diode using a simple setup, with a degenerate phase-conjugate feedback. However, more complex configurations have been associated to PCF.

First, an external pump of a phase-conjugate mirror was also considered in theory. In that configuration, the laser locks to the frequency of the pump before the undamping of the relaxation oscillations [39].

Such results were experimentally observed with a PCM made of rubidium vapor cell, as presented Fig. 1.13. There is a 300 MHz detuning between the frequency of the pump of the PCM and the frequency of the free-running laser. At a given value of feedback strength, the laser locks to the frequency of the pump and its optical spectrum is thinner. Then, sidebands at the frequency of the relaxation oscillations (f_{RO}) appear and are followed by new harmonics of

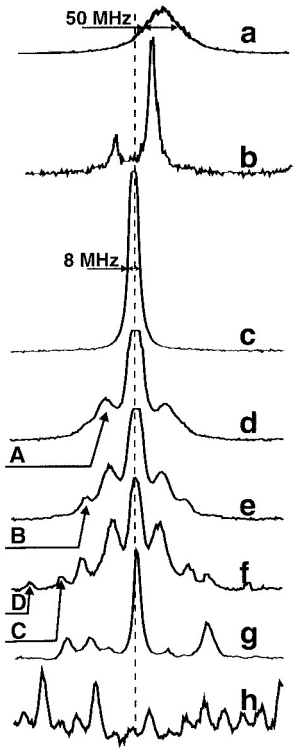

Figure 1.13: Optical spectra of a laser diode with PCF from a rubidium vapor cell at increasing feedback strength: (a) free running laser, (b) four-wave mixing in the laser, (c) the laser locks to the pump frequency, (d) two sidebands appear, (e) and (f) four sidebands, (g) spectrum becomes broad and (h) coherence collapse. Figure taken from Ref. [60].

f_{RO}. The spectrum becomes broader until coherence collapse occurs [60].

A strong detuning δ of the PCM with respect to the feedback rate, i.e. if $|\delta| > \frac{\sqrt{1+\alpha^2}}{\tau_p}$, will only create chaotic solutions [42].

Moreover, the phase-conjugation can be used as a way to easily inject light from a master laser into a slave laser, by using a $BaTiO_3$ crystal as a "shared-waveguide" between the two lasers [61, 62].

The dynamical effect of phase-conjugate feedback was also theoretically explored for quantum cascade lasers (QCLs). QCLs are stable in a larger range of feedbacks strength with PCF than with COF [63].

1.5 Objectives

The chaos generated by PCF has been qualitatively studied in several works in the past thirty years [41, 52–54, 59]. However, no extensive quantitative study has been conducted, except for the two studies made by our group in 2016 [56, 64]. These studies were however limited not only by the range of laser and feedback parameters considered but also by the limited time resolution of the measured dynamics.

Therefore, we decided to extend their results with a broader qualitative study. After a presentation of the experimental setup in chapter 2, we will discuss the following results:

- Reference [56] analyzed the chaos bandwidth (defined in section 3.1). The chaos bandwidth is analyzed by using a three-times larger measurement bandwidth, as we report in chapter 3.

- Reference [64] analyzed theoretically the chaos bandwidth, the permutation entropy and the spectral flatness (defined section 3.1) but it used the standard unfiltered PCF equations. Still in chapter 3, we extend its conclusions by considering the finite depth penetration time in the PCM and also comparing theory with experiment.

- Similarly, the permutation entropy of PCF had never been measured. We analyze it here, in chapter 4.

- Still, our group was the first to evidence external cavity modes in Refs. [52, 54, 57, 65–67]. Still, how the feedback parameters influence the stability and properties of the ECMs was not considered year experimentally. In particular, Refs. [65, 66] predicted that the frequency of the external cavity modes was independent of the length of the external cavity but no experimental proof had been made. This will be done in chapter 5.

- Finally, we found interesting to analyze more complex PCF configurations such as one in which a Faraday rotator is inserted in the feedback loop. That configuration leads to interesting new dynamics when compared to

conventional PCF, and these dynamics are here unveiled theoretically in chapter 6.

Chapter 2

Experimental setup

Various configurations have been used to study the dynamics of the laser diode subjected to phase-conjugate feedback (PCF). We will here present the key components of our experiment, i.e. the phase-conjugate mirrors and its principle, and the different elements of the experimental setup (laser diodes and measurement devices).

2.1 Phase-conjugate mirrors

The main components of the PCF experiment are the laser diode and a phase-conjugate mirror (PCM).

2.1.1 Principle of phase-conjugate mirrors

We present first some general statements about PCMs. A beam is the phase conjugate of another beam when they are counterpropagating but also have the same amplitudes and phases. If we consider the complex expression of the electric field, the amplitude of the phase-conjugate beam is the complex conjugate of the original beam amplitude.

We take the example of a planar wave. The amplitude of the input electric field is written as follow:

$$E(x,y,z,t) = A(x,y,z)e^{i(kz+\phi(x,k,z))}e^{-i\omega t} \tag{2.1}$$

where $A(x,y,z)$ is defined as the amplitude of $E(x,y,z,t)$, $\phi(x,y,z)$ is the spatial dependency of the phase, k projection of the propagation vector on the direction z and ω the frequency of the wave (in radians).

The electric field of the phase-conjugate beam is the following:

$$E^*(x,y,z,t) = A(x,y,z)e^{i(-kz-\phi(x,k,z))}e^{-i\omega t} \tag{2.2}$$

The signs of both the phase and the propagation vectors have been inverted. It has two consequences :

- The spatial modifications of the phase will be "corrected", the phase-conjugate beam being subjected to the inverse phase modification of the input beam,
- The phase-conjugate beam will have the same propagation direction as the input beam, but reversed. For instance, if the input beam was diverging from a source, the phase-conjugate beam will be converging into the source of the input beam.

In practice, phase-conjugation is often non-degenerate and light may not be monochromatic but the principle remains.

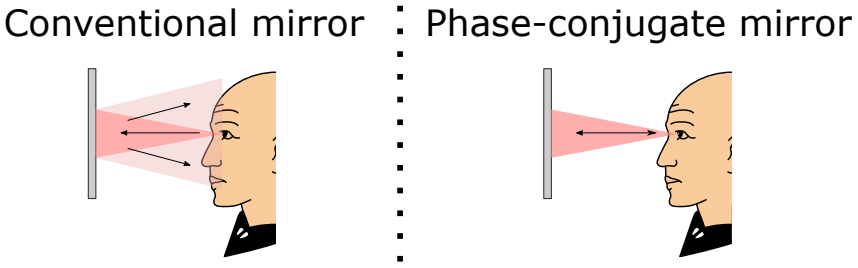

Figure 2.1: Illustration of the effect of a PCM compared to a conventional mirror. PCM inverts the propagation of the light and the person is only able to see his eye.

To illustrate phase-conjugation, we consider a human looking himself in a mirror, as shown in Fig. 2.1. The eye is open and he is able to see a larger part of the mirror, in the solid angle corresponding to his eye. If the mirror is a conventional mirror, the person can see most of his face. However, if the mirror

is a phase-conjugate mirror, the reflected light is directly inverted and he is only able to see its eye. Of course, phase-conjugation can not be achieved when the energy of the light is too low and spread on a too large surface.

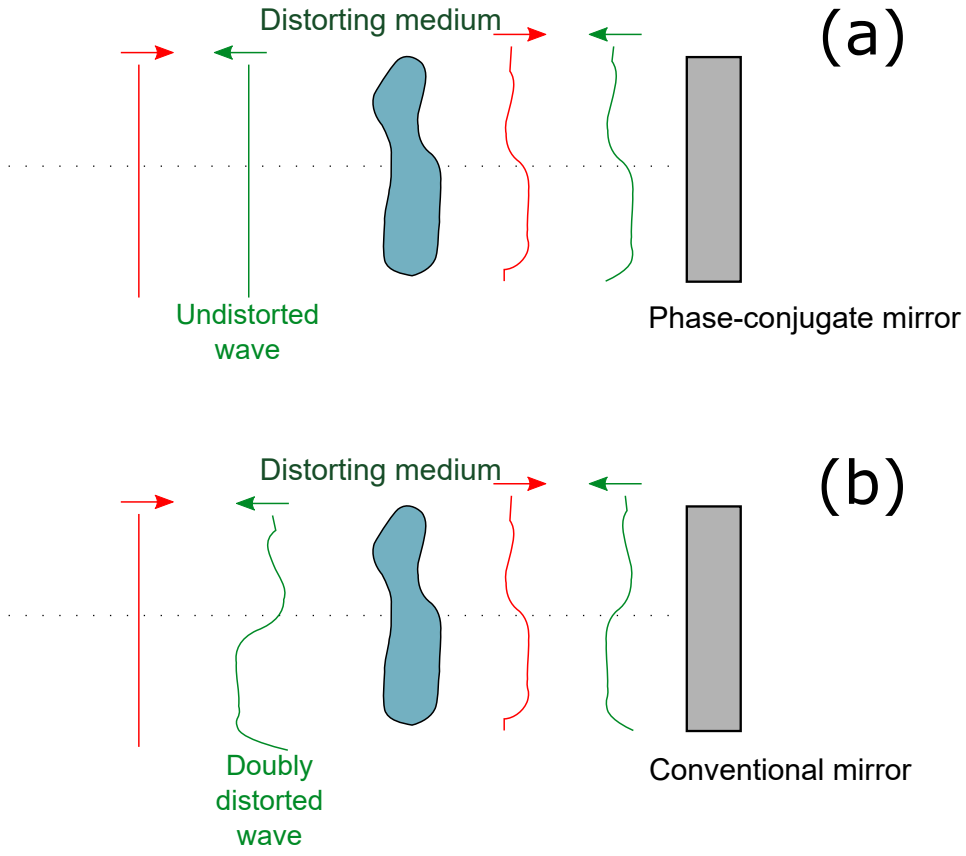

Figure 2.2: The traditional illustration of the wavefront corrective effect of phase-conjugation [68–71]. A wave with a planar wavefront is reflected by (a) a phase-conjugate mirror and (b) a conventional mirror. The wavefront of the forward wave is represented in red and the one of the reflected wave is in green.

Another example of the properties of phase-conjugation is presented in Fig. 2.2. A wave with a plane wavefront propagates to the right, is distorted by a distorting medium and then reflected by a mirror (blue wave). If the mirror is a phase-conjugate mirror, as shown in Fig. 2.2 (a), the wavefront is not inverted and the distortion is canceled, while if the mirror is a conventional mirror, as shown in Fig. 2.2 (b), the wavefront is distorted twice, first during

its forward propagation and second during its backward propagation. Such wavefront distortion leads to a deformation of the observed image.

2.1.2 Physical processes to create phase-conjugate mirrors

In order to generate a phase-conjugate mirror, various setups, using different physical processes, can be used. Complete reviews can be found in Refs. [69, 71, 72].

2.1.2.1 Scattering mediums

The first phase-conjugation was historically achieved in 1972 using stimulated Brillouin scattering (SBS) in a gas cell. The back-scattered light generated by SBS was already known to be in the opposite direction of the incoming beam but Zel'dovitch *et al.*, observed that the reflected wavefront was similar to the indicident one [73]. Phase-conjugation was later achieved with other types of stimulated scattering, such as stimulated Raman scattering [74], stimulated Rayleigh-wing scattering [75] or photorefractive back-scattering [76].

2.1.2.2 Four-wave mixing

However, the most used phase-conjugation method is four-wave mixing (FWM), in third order ($\chi^{(3)}$) mediums [71]. Its principle is shown in Fig. 2.3. As its name implies, FWM is based on the interaction of four waves, a signal wave, two pump waves and a fourth wave, in a third-order non-linear medium. It can be described as real-time holography: the signal and one of the pump waves create a grating in the material, grating that is then read by the second pump wave to generate the phase-conjugate signal. The phase-conjugate wave is generated by the $\chi^{(3)}$ response of the medium [71].

Four-wave mixing enables the generation of the beam at a new frequency. If the two pump beams have frequencies f_1 and f_2 and the signal beam a frequency f_3, the fourth beam will have frequencies at $\pm f_1 \pm f_2 \pm f_3$ and third-harmonic generation $3f_i$. Degenerate four-wave mixing implies $f_1 = f_2 = f_3 = f$,

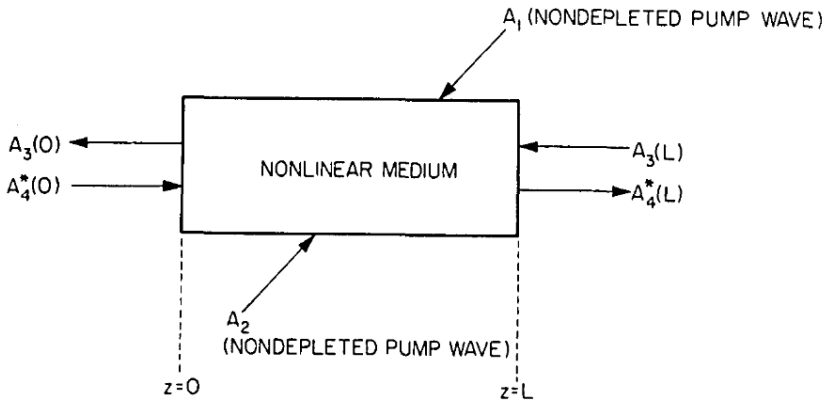

Figure 2.3: Geometry of four-wave mixing, from Ref. [77]. In a $\chi^{(3)}$ non-linear medium, four waves interact: two pump beams (A_1) and (A_2), one signal beam (A_3) and the phase-conjugate (A_4^*).

so the phase-conjugate beam has a frequency of f, in addition to third-harmonic $3f$ generation. One of the main advantage of degenerate four-wave mixing is that if the two pump beams are opposite, the phase-matching condition is always fulfilled [77]. Degenerate four wave mixing also enables the use of only one laser to generate both the pump and the signal. Such configuration is used in self-pump mirrors, i.e. mirrors whose pump is taken from the laser output.

A widely used medium to obtain the aforementioned gratings is the photorefractive mediums, where the gratings to generate phase-conjugation are obtained using Pockels effect. The physical principle of the photorefractive effect is presented in Fig. 2.4. The interference fringes homogeneously illuminate the material. This nonhomogeneity of light intensity leads to a migration of the photoexcited charges into the darker areas. The difference in the charge density creates a space charge field, that changes the refractive index through Pockels effect. The refractive index is now a periodic grating, of same wavelength than the original fringes but with a $\pi/2$ detuning. The response time of the material, related to the mobility of the carriers, is directly linked to the time it takes to write the gratings structure into the photorefractive material.

We can note that four-wave mixing was also achieved in broad-area semiconductor lasers. In that case, the gratings is inscribed into the semiconductor

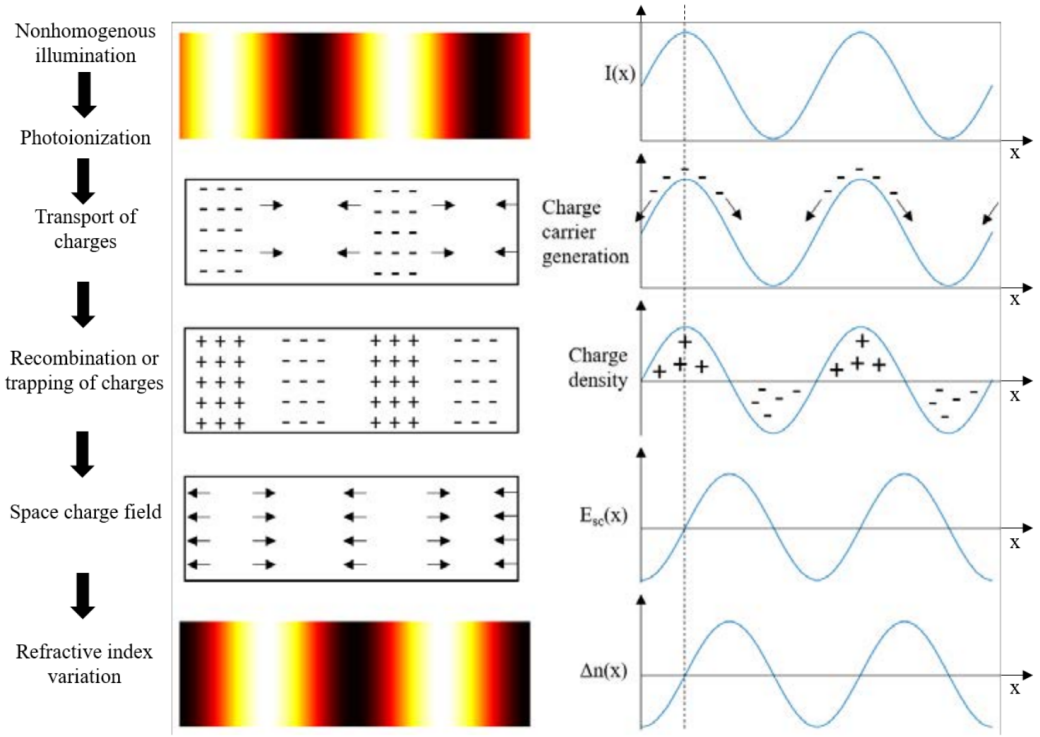

Figure 2.4: Principle of photorefractive effect in a material non-homogeneously illuminated. Figure taken from Ref. [78].

inner structure of the laser by the pump beam and its reflection in the laser rear facet [79, 80]. There are two main advantages: the response of the system is faster because of the low relaxation time of the carriers (fs-ps) [81, 82] and the phase-conjugate beam can be electrically amplified in the laser [83].

2.1.3 Photorefractive self-pump phase-conjugate mirror and cat-mirror

The phase-conjugate mirrors obtained in photorefractive crystals are often self-pumped, i.e. the pump beams and the signal beam are created by the same laser. A peculiar kind of self-pumped PCM is named the "cat" mirror. It was first demonstrated in 1982 by J. Feinberg [84]. He used the image of a cat to illustrate the image correction properties of the proposed phase-conjugate

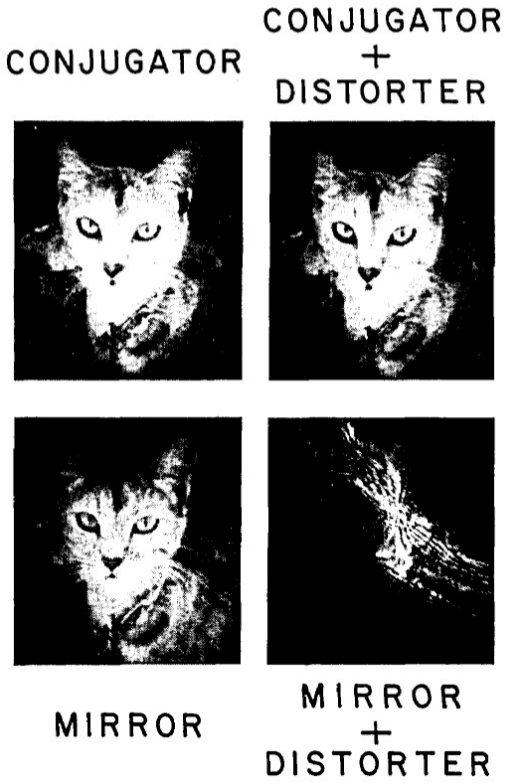

Figure 2.5: The "image of a common household member" used in Ref. [84] to show the efficiency of the 'cat' mirror.

mirror (see Fig. 2.5) and consequently that mirror is always named cat.

Technically speaking, its principle is presented in Fig. 2.6. The phase-conjugation occurs in a photorefractive crystal and uses an effect named "fanning". J. Feinberg reported the observation of an asymmetric defocusing of light in photorefractive crystals. The deviation of light, or fanning, occurs in the direction of the c-axis of the crystal (Fig. 2.6) [85]. It is used to generate the pump for the four-wave mixing process in the crystal, without any additional beam splitting device.

After the beam enters the crystal, part of the input light A_1 is deviated in the direction of the c-axis thanks to the fanning physical process. That deviated light is named $A_{1,d}$ in Fig. 2.6. It experiences total internal reflection in I_1 and I_2 and then arrives at point G_2. At that point, four-wave mixing occurs between

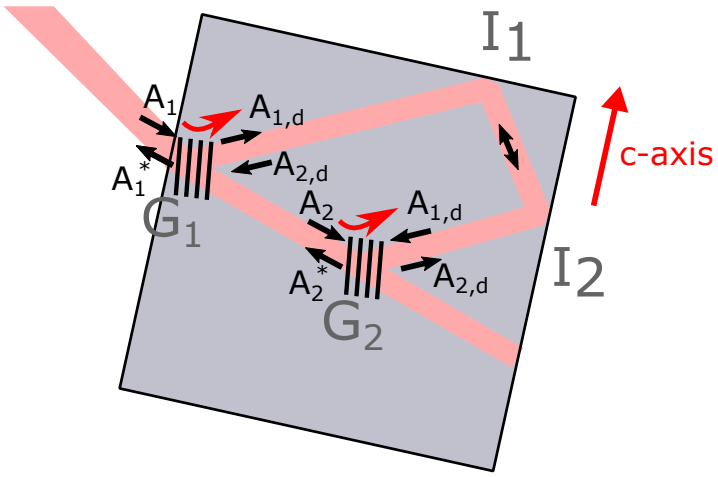

Figure 2.6: Principle of the 'cat' self-pumped phase-conjugate mirror. The fanning is indicated with curved red arrows.

the beam A_2 that went straight from G_1, the beam $A_{1,d}$ and the beam that is deviated by fanning in G_2, named $A_{2,d}$. The fourth wave is the phase-conjugate of A_2. Similarly, in G_1, four-wave mixing occurs between A_1, $A_{1,d}$ and $A_{2,d}$, the fourth wave A_1* being the phase-conjugate of the input wave A_1.

To obtain total-internal reflection, the crystal has to be carefully polished. Therefore, porous crystals such as $Sn_2P_2S_6$ (SPS) have not been used in 'cat' phase-conjugate mirrors. In Ref. [84] the crystal is $BaTiO_3$ (barium titanate) and that crystal was used in most of the further studies [86–90]. Copper-doped $(K_{1-x}Na_x)_{0.4}(Sr_{1-y}Ba_y)_{0.8}Nb_2O_6$ (Cu:KNSBN) [91] and iron-dopped $KNbNO_3$ ($Fe:KNbNO_3$) [92, 93] were also used. All these experiments were performed at wavelengths around 480-530 nm. Cobalt-dopped barium titanate $Co:BaTiO_3$ crystals enable efficient phase-conjugation at 800 nm [94] and Rhodium-dopped barium titanate $Rh:BaTiO_3$ at 1.06 μm [95]. In 2001, one of the few dynamical studies of a near-infrared laser under a phase-conjugate feedback was performed in a 'cat' mirror with $Rh:BaTiO_3$ cubic crystal configuration [59]. In our study, we use two different crystals of the same material. These two crystals, manufactured together by the German company FEE in 2015, are 5 by 5 by 5 mm cubes, cut parallel to the c-axis. They are dopped with rhodium (Rh) at 1000 ppm to make them more efficient at infrared wave-

lengths. Indeed $BaTiO_3$ has an absorption maximized for visible light at low wavelength but adding Rh drives the peak of absorption to 600 nm and enables the crystal to be sensitive to a beam with a near-infrared wavelength of 850 nm [96].

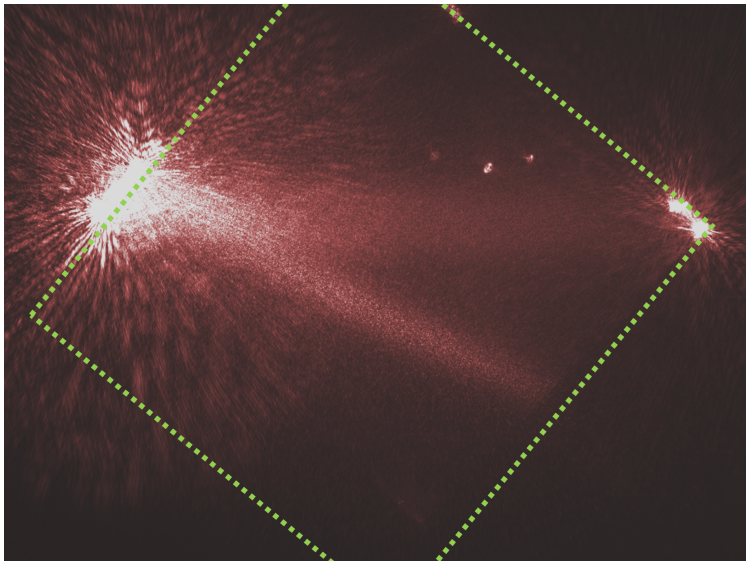

Figure 2.7: Light path in the 'cat' phase-conjugate mirror. The light enters the crystal from the left. The edges of the cube are roughly indicated with a green dotted line.

Using an infrared camera, we took the picture displayed in Fig. 2.7, that shows the light path as phase-conjugation occurs in the crystal. The light is seen entering from the left, and then part of the light is deviated by fanning into the top-right corner. The two bright points on that corner correspond to the total-internal reflections of the fanned beam.

$BaTiO_3$ crystals have a response time of a few ms [97]. However, it is not a default in phase-conjugate feedback experiments because the phase-conjugation still takes place but the crystal is insensitive to the fast variations (ns-scale) of the laser output. A photorefractive material with a faster response time may generate a phase-conjugate feedback that is inconsistent with the laser output signal. For instance, if the PCM is sensitive to the fast variations of a chaotic laser signal, it could create a chaotic and always changing reflectivity. Such PCF study would be unworkable.

2.1.4 Analysis of phase-conjugate beam in the cat configuration instabilities

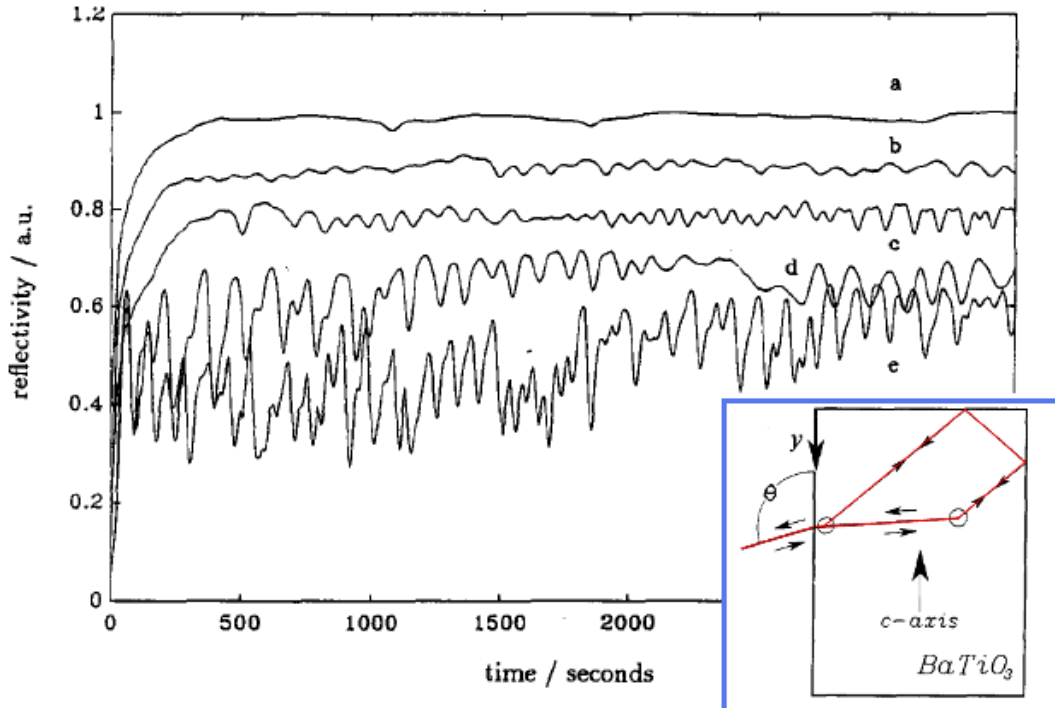

Figure 2.8: Temporal evolution of the reflectivity of a PCM-cat mirror, for a lateral position y equal to 5.64 mm, (a), 5.99 mm (b), 6.2 mm (c), 6.33 mm (d), 6.4 mm (e). In particular, time trace (a) is stable and time trace (e) has been proven to be chaotic. The inset shows the geometry of the mirror. Figure taken from Ref. [87].

As we try to implement phase-conjugation in cat mirrors, a question will appear: is the reflectivity stable and constant with time? The temporal instability of the reflectivity of cat mirrors has been reported from 1985. In Ref. [98], the authors reported various experimental results about these instabilities. In particular, they described the possibility of oscillating, stable and chaotic dynamics of the reflectivity. Periodic oscillations and steady-state were observed in a cat-mirror whose faces had been covered by a diffusely reflecting layer of Tipp-Ex. Damped oscillations leading to steady-state and chaos were observed with a highly reflecting cover, silver paint in that case. They reported

a linear increase of the period of the regular oscillations with respect to the intensity of the pump beam and supposed the oscillations were created by spatial oscillation of the photorefractive gratings. In the case of highly reflecting sides, they explained the chaotic states by the simultaneous presence of two channels, i.e. two possible optical paths. When the signal power is above a threshold, the reflectivity stabilizes. In 1987, Gauthier *et al.* [86] proposed a numerical explanation for that result: the interactions between the two points of four-waves mixing in the cat mirror make the evolution of the reflectivity chaotic. Thee authors experimentally confirmed their model with a $BaTiO_3$ PCM-cat: the "Rényi entropy" of its reflectivity, which is an indicator of the diversity of the dynamics, converges to a positive value.

Several ways have been then proposed to stabilize the reflectivity of the PCM-cat. In 1992, Rauch *et al.* studied the influence of the position of the input point of the light on the instabilities of a $BaTiO_3$ PCM-cat. They moved the PCM parallel to its c-axis and measured the time series, reproduced on Fig. 2.8. They concluded that a carefully chosen point enables constant and high values of reflectivity [87]. Jeffrey *et al.* confirmed that result by calculating the Lyapunov exponent of the experimental reflectivity of a $BaTiO_3$ PCM-cat moved parallel to its c-axis [88]. Medrano *et al.* obtained a stable reflectivity with a specially-cut $Fe:KNbNO_3$, its edges being non parallel to its c-axis [93]. Zheng *et al.* shows that the polarization of the output light into a $Cu:KNSBN$ PCM-cat can also stabilize its reflectivity [91]. In 1995, Goetz *et al.* studied the influence of the temperature of a $BaTiO_3$ crystal on the dynamics [89].

We have tried to reproduce that later result, by mounting the crystal on a radiator. The temperature is then stabilized but still, we did not observe stabilization of the reflectivity. Geometric studies were also not efficient in stabilizing the laser over long time. We explain that lack of stabilization by the unstable nature of the laser output light. The authors trying to optimize the reflectivity of a PCM used Faraday isolator to prevent the laser dynamics from being destabilized while our goal is to have an unstable laser to study its dynamics.

However, these unwanted variations enabled us to explore the influence of the feedback strength on laser without the need of human intervention

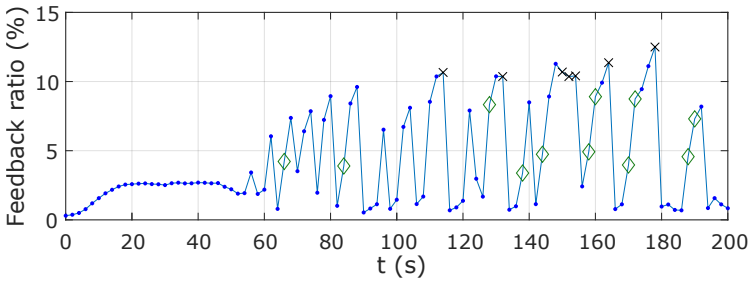

Figure 2.9: Variation of the feedback ratio F (0.64 times the reflectivity of our PCM) versus time. The dots, diamonds and crosses indicate that the laser dynamics are respectively chaotic, self-pulsing or steady state. Figure taken from [99] and modified.

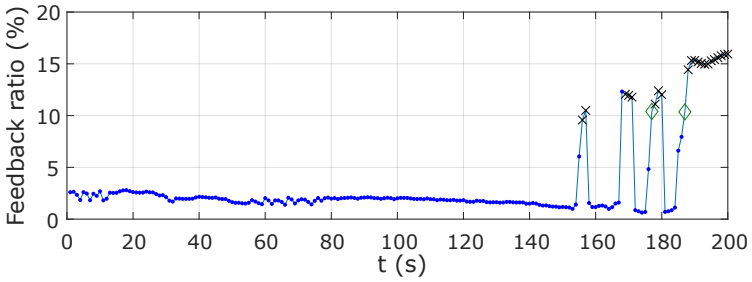

Figure 2.10: Variation of the feedback ratio F (0.64 times the reflectivity of our PCM) versus time. The dots, diamonds and crosses indicate that the laser dynamics are respectively chaotic, self-pulsing or steady state. Figure taken from [99] and modified.

on the variable attenuator. Figure 2.9 shows an example of such variations and how the system explores various dynamical states depending on the PCM reflectivity. These dynamical states will be presented in more details in chapter 3. By a careful choice of the geometry, we were also able to stabilize the PCM for a relatively long time, up to several minutes but the reflectivity suddenly became irregular after a variable time. Figure 2.10 is an example of such stabilization of the reflectivity, followed at $t = 155$ s by the onset of irregular variations of the reflectivity.

As now, we know how to generate a phase-conjugate mirror, let us present the experimental setup to analyse nonlinear dynamics of a laser subjected to phase-conjugate feedback.

2.2 Experimental setup

We have presented the principles of the two main components, the laser diode and its dynamics (section 1.3) and the cat mirror (section 2.1.3). We will now detail the experimental setup that is used in this thesis.

2.2.1 Setup description

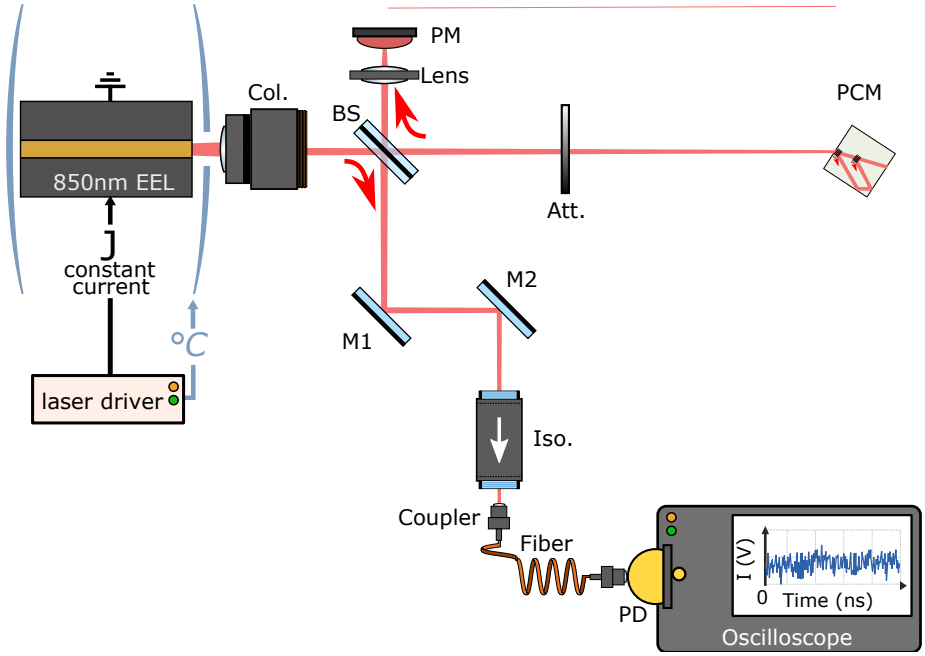

Figure 2.11: Setup of a PCF experiment, with a cat-mirror. The edge-emitting laser is place left and the PCM right. Col. means collimator, BS means beam splitter, Att. means attenuator, PM means powermeter, M1 and M2 are two mirrors, Iso. designates a Faraday isolator and PD means phototiode.

The setup, derived from the setup presented in Ref. [52], is presented in Fig. 2.11. The two main components of our experiment are the laser and the phase-conjugate mirror. The principle of the mirror was described in the above sections. The laser is an edge-emitting laser (EEL) emitting in the near-infrared ($\lambda \approx 850$ nm) and its specifications will be given in section 2.2.2. It is mounted in on a Newport 710 Temperature Controlled Laser Diode Mount, controlled by

a Newport Model 6100 Laser Diode and Temperature Controller. The mount of the laser is maintained at a temperature of 20°C.

Semiconductor lasers have diverging outputs and we placed a Newport 5722-B-H aspheric lens (Col.) a few centimeters after the laser to collimate the beam. The distance between the laser and the collimating lens can be adapted to change the beam divergence, for instance to better focus the beam on the mirror.

The light is then splitted by a 80-20 beam splitting plate (BS). Precise measures show 78% of the light is not deviated and 19% of the light is deviated. The straight-going beam is then attenuated by a variable neutral density, slightly tilted to avoid unwanted conventional feedback into the laser. We often remove the attenuator, because the reflectivity of the PCM can be decreased by a small tilt in its geometry. After the attenuator, the light enters the cat phase-conjugate mirror. As explained in section 2.1.3, the mirror generates the backward-propagating phase-conjugate of the laser output.

The phase-conjugate beam is then splitted by the beam splitter and 19% of it is measured by a powermeter (PM). If necessary, a lens is placed in front of the powermeter to focus the large beam into the measurement cell. The part of the feedback that is not diverted by the beam splitter returns into the laser.

The part of the output of the laser that is splitted after the collimator is coupled into an optical fiber. We use a free-space isolator Thorlabs IO-3-850-HP to prevent reflections from the coupler. Two mirrors are placed before the isolator to help the coupling of the light into the isolator and the fiber. The measurement arm itself will be described in section 2.2.3.

Apart from the adjustments of the light path, the important parameters that will change are:

- the feedback strength, which is controlled by the attenuator and by the spontaneous time-dependent variations of the reflectivity of the PCM,
- the laser pump current, which can be tuned at the driver of the laser,
- the distance between the laser and the PCM. The $BaTiO_3$ crystal is placed on an rail. The distance can vary from 14.7 cm to the length of the

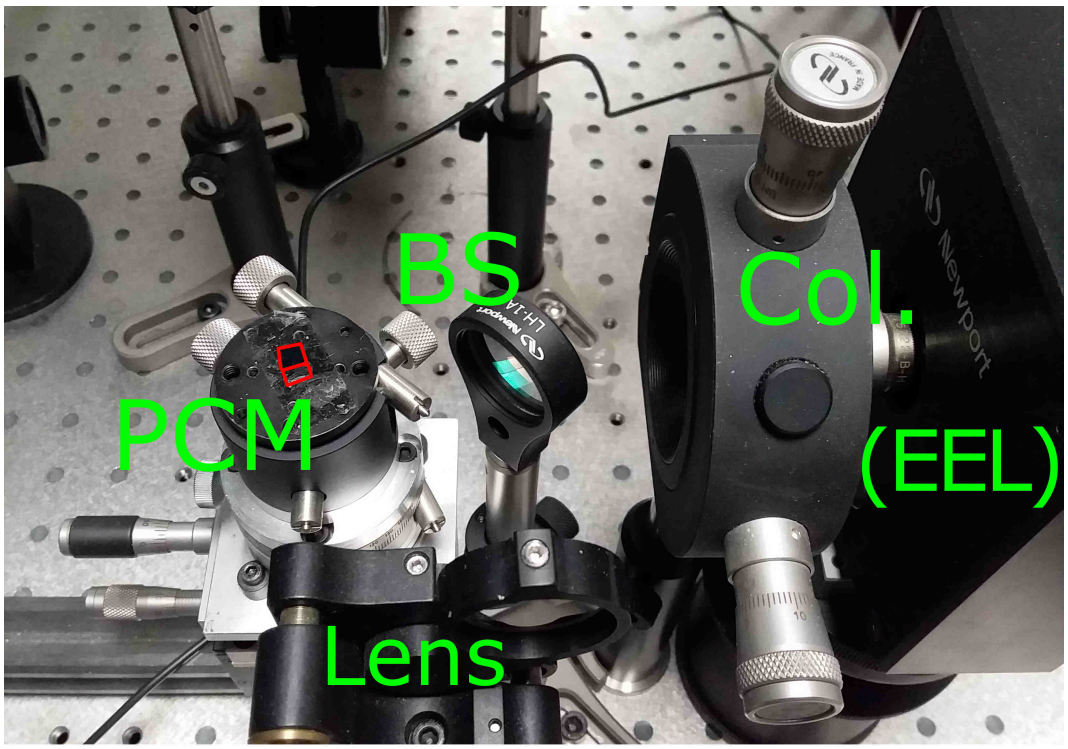

Figure 2.12: Photograph of the experimental setup with the shortest possible external cavity. The mechanical mount of the phase-conjugate mirror (PCM, the crystal is highlited in red) touches the beam splitter (BS), whose mount is as close as possible to the collimator (Coll.) and the laser mount (EEL). In the foreground, the lens is the one that focalizes the feedback beam into the powermeter.

optical table. The minimum distance is reached when the PCM is sticked to the beam splitter. Such configuration is detailed in Fig. 2.12.

2.2.2 Laser diodes

We have used two different laser diodes. Both are $GaAlAs$ Fabry-Perot index-guided laser diodes produced by JDS-Uniphase, from the SDL-5400 series. The first model, a SDL-5420 was used in the first year of study. In particular, it is used for the results of Refs. [99–102]. Then that laser stopped lasing and was replaced by another laser, model SDL-5410. It was used in Ref. [103]. Their characteristics are given below.

We choose that series of Fabry-Pérot laser to make easier the comparison with previous experiments from our group: in Refs. [54, 56, 104, 105] the laser was a SDL-5400 and in Ref. [52], the laser was the aforementioned SDL-5420 ; but also with many experiments in the past 30-years about nonlinear dynamics of laser diodes that also use SDL-series laser diodes.

2.2.2.1 JDS-Uniphase SDL-5410

While, chronologically speaking, it is the second laser we used, we have more data available to characterize the SDL-5410 than the SDL-5420 laser.

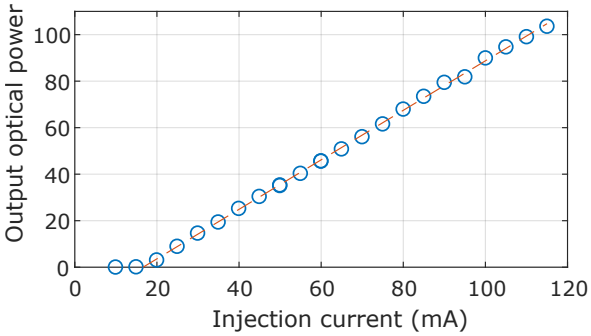

Figure 2.13: Light-current curve of the JDS-Uniphase SDL-5410 laser diode. The equation of the linear section of the curve was obtained by linear regression for the values of injection current higher than 19 mA.

First, we present in Fig. 2.13 the light-current curve of that laser. The linear regression was performed on the points with an injection current higher than 19 mA. We obtain a threshold current of $I_{th} = 16.6\ mA$ and an electrical-optical efficiency of 1.06 W/A.

We then present in Fig. 2.14 the evolution of the optical spectrum of the laser for various values of pump current I. At 15 mA, the emitted light is from spontaneous emission. The spectrum shows resonance at regularly spaced wavelengths that correspond to the modes of the Fabry-Pérot cavity. We can determine the free-spectral range: $FSR = 124\ ps$. Then, at $I = 20\ mA$, the spectrum shows a maximum at 856.2 nm. However, other modes are lasing simultaneously, in particular at 855.8 nm. The multimode behavior of the

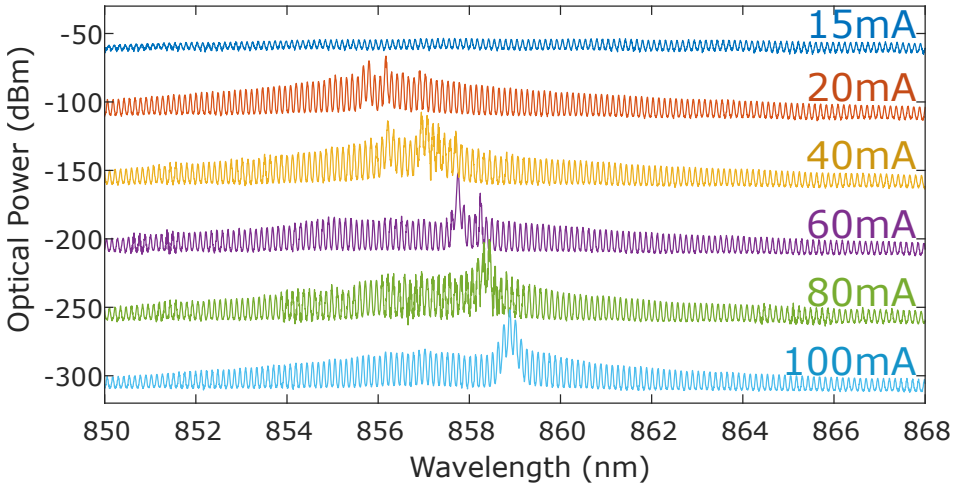

Figure 2.14: Experimental evolution of the optical spectrum of the SDL-5410 laser diode, for increasing values of pump current. Each successive spectrum has an offset of 50 dBm with the respect to the previous one.

laser is even more visible for $I = 40\ mA$. As the pump current increases, the frequency of the laser red-shifts, up to a wavelength 858.9 nm under a pump current of 100 mA.

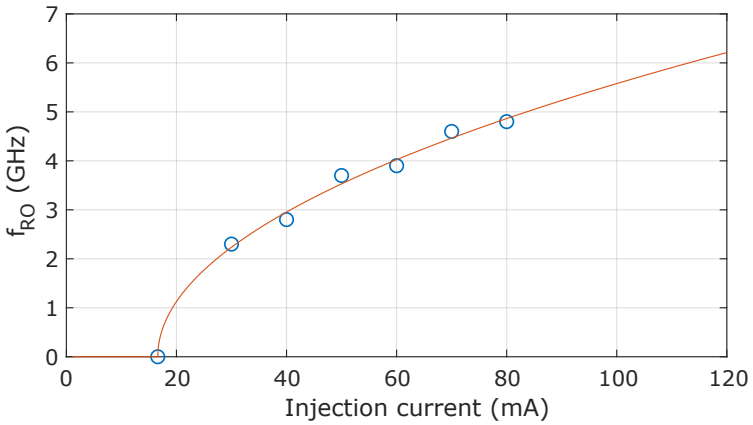

Figure 2.15: Evolution of the frequency of the ROs of the SDL-5410 laser diode. The dots correspond to the measured points.

Last, we present in Fig. 2.15 the frequency of the relaxation oscillations f_{RO} versus the pump current I. The relaxation oscillations appear when the

laser diode is modulated, which is also true when being self-modulated such as in optical feedback experiments. The values of f_{RO} are therefore obtained by visual observation of the spectrum of the laser under very low feedback. We observe a peak at f_{RO} in the Fourier spectrum of the laser output power. Then, we performed a linear regression to obtain an approximation of the general evolution of f_{RO} with I.

$$f_{RO} = K\sqrt{\frac{I - I_{th}}{I_{th}}} \tag{2.3}$$

with K a real coefficient, we performed a linear regression of $\sqrt{\frac{I-I_{th}}{I_{th}}}$ and we obtain $K = 2.49$ GHz. The corresponding curve is indicated in red in Fig. 2.15.

2.2.2.2 JDS-Uniphase SDL-5420

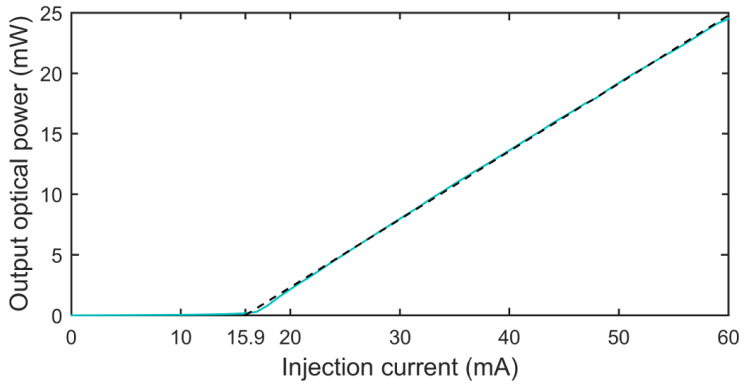

Figure 2.16: Light-current characteristic of the SDL-5420 laser diode used in our experiment. Figure taken from Ref. [106].

The other laser diode is of the model SDL-5420. According to its datasheet, it can be pumped up to ≈ 200 mA and has a maximum output power equal to 200 mW.

It was used in previous experiments in our group and Émeric Mercier gives in his PhD thesis [106] the light-current curve of that laser and the evolution of its relaxation oscillation frequency versus its pump current. They

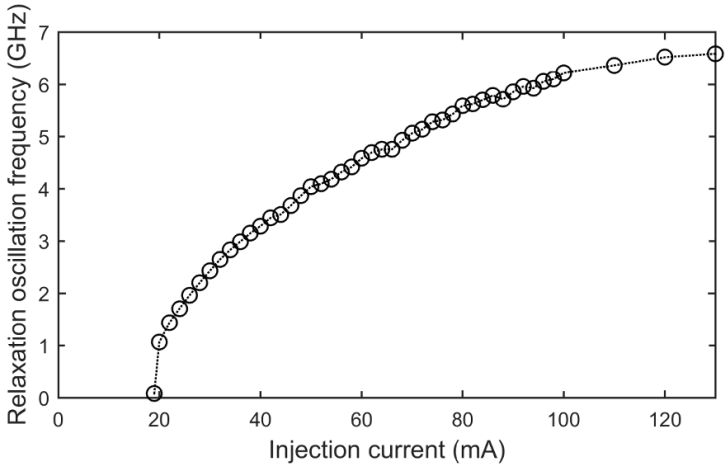

Figure 2.17: Evolution of the frequency of relaxation oscillations as a function of the injection current of the laser diode. Figure taken from Ref. [106].

are reproduced respectively in Fig. 2.16 and in Fig. 2.17. From Fig. 2.16, the threshold of the laser is 15.9 mA. The value of the RO frequency was obtained by relative intensity noise measurements. In the operating range of pump current 40-50 mA, $f_{RO} \approx 3.5$ to 4.5 GHz.

2.2.3 Measurement arm

Our laser diode generates high-frequency dynamics. To record them, part of the laser output light is coupled into an optical fiber. A photodiode is then fiber-coupled and converts the optical dynamics into the dynamics of a photocurrent.

We used two different photodiodes :

- The first one was a Newport 1414-50, with a 3-dB bandwidth running from DC to 25 GHz. At 850 nm, it has a responsivity of roughly 0.3 A/W. The evolution of that responsivity versus the frequency is presented in Fig. 2.18. The input of that photodiode is a multimode fiber with 50 μm core. Using multimode fiber facilities the coupling of light into the fiber.

- The second one was a Newport 1474-A, with a 3-dB banwidth running from 15 kHz to 38.5 GHz. Its output is a singlemode fiber with a 9 μm core.

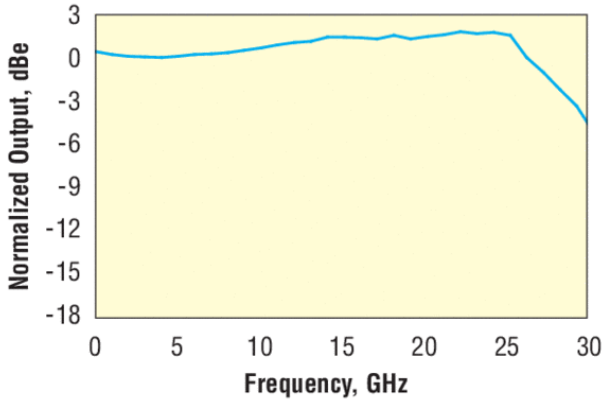

Figure 2.18: Frequency responsivity of the Newport 1414-50 photodiode, from the manufacturer. Source : `https://www.newport.com/p/1414-50`

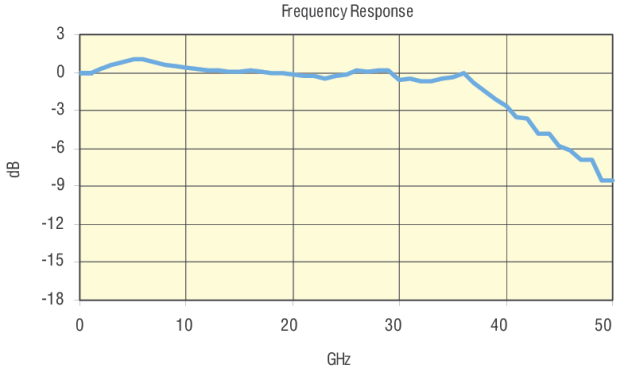

Figure 2.19: Frequency responsivity of the Newport 1474-A photodiode, from the manufacturer. Source : `https://www.newport.com/f/22-ghz-and-38-ghz-photoreceivers`

It requires more careful coupling of light but the photodiode has a slightly better responsivity, $\approx 0.35\ A/W$. We give in Fig. 2.19 the responsivity of the 1474-A phototiode. It is worth noting there is a 2-dB high peak in the responsivity around 5 GHz. That value being close to the relaxation oscillations frequency of our laser, it could led to a small overestimation of the contribution of that frequency.

To avoid filtering the photodiode electronical output, we directly plug the photodiodes to the oscilloscope.

We use two models of oscilloscope. The first one is a Tektronix DPO72304SX oscilloscope. It has a bandwidth of acquisition of 23 GHz and a sampling rate of 50 GSample/s. We couple the 1414-50 photodiode with that oscilloscope. The second oscilloscope is a Teledyne LeCroy 10-Zi-36, with a 36 GHz bandwidth and a sampling rate of 80 GSample/s. It allows the capture of the full dynamics from the 1474-A photodiode.

2.2.4 Powermeter and real-time measurement of the reflectivity

To monitor the feedback strength, as described in section 2.2.1, we use a powermeter. Depending on the available one, we used Newport 818-IR (Germanium), 818-IG (InGaAs) and 818-SL (Silicon) photodetectors. A crucial issue of our work was to synchronize the measurements of the feedback strength and of the laser output time series, since a time series is measured each half-second.

To do so, a first method is to record the feedback strength with a PC connected by a Newport 843-R-USB powermeter. The software of the powermeter is not compatible with interface-based instrument communication protocols. Therefore, we obtain a reference point by blocking the laser light, as both laser output power (measured at the oscilloscope) and reflectivity immediately fall to 0.

The second method is simpler to implement: we directly plug the Newport photodetector to the oscilloscope. We suppose the measured voltage linearly varies with the optical power and we calibrate our measurement with a 2 mW power. Since the duration of time series and the rise time of the photodectors are of the same order of magnitude ($\approx 2\ \mu m$), we do not consider possible low-scale variations in the feedback strength and we take its average value on the duration of the laser output time series.

2.3 Conclusion

We have presented our experimental setup. The first component, the self-pumped phase-conjugate feedback. It uses degenerate four-wave mixing in a

photorefractive $BaTiO_3$. The spontaneous instabilities in the mirror yield a time-dependent reflectivity, which enables us to study the dynamics at various feedback strengths without user's intervention. Then, we have shown the properties of the two laser diodes used in this thesis, in particular the evolution of their output power, wavelength and relaxation oscillations frequency with respect to the pump current. Last, we presented the measurement apparatus, namely the photodiodes and the measurement of the feedback strength.

Chapter 3

Study of the chaos bandwidth of laser diodes with phase-conjugate feedback

In chapter 1, section 1.3, we described the ability of laser diodes under phase-conjugate feedback to generate chaos. To enable the fast encryption of chaos-based communication, the laser diodes must present high frequencies and a broad range of modulation. Cryptography using broadband chaos will also be harder to break than chaos deployed over a small range of frequencies. The following work intends to be a proof of concept of the capacity of the PCF to fulfill these requirements. We study here in detail the qualitative evolution of the chaos generated by phase-conjugate feedback.

That work was presented in various conferences [100, 101, 107] and published in several articles [99, 103, 107].

3.1 Definitions of the different indicators of the chaos quality

To qualitatively analyze our results, we define here two indicators, the chaos bandwidth and the spectral flatness, and we will give the state of art.

3.1.1 A first indicator: the chaos bandwidth

3.1.1.1 Different definitions of chaos bandwidth

In random bit generation using chaotic signal, the need of fast chaos is a direct consequence of the objective of generating numbers at high rates [108, 109]. Broadband chaos will also be harder to break in secured communications [110]. Last, the resolution of a chaotic lidar is increased thanks to the large bandwidth of the chaos used [111].

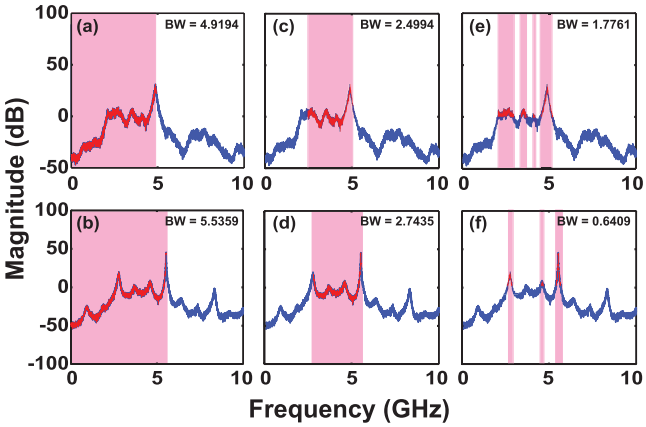

Figure 3.1: Three definitions of chaos bandwidth used on two different spectrum: standard chaos bandwidth (a-b), chaos bandwidth centered on the main peak (c-d) and effective chaos bandwidth (e-f). Figure taken from Ref. [112].

To quantify the bandwidth of chaos, information can be obtained from the radio-frequency (RF) spectrum, i.e. the spectrum of the power of the output of the chaotic laser. The conventional definition of bandwidth, that considers the frequency at which the signal energy is attenuated by 3dB, can not be applied to chaotic signals, since they do not have a flatband frequency content. Other definitions have been proposed:

- First, a simple way is to study the range of frequencies on which the chaotic spectrum extends. A definition was proposed in 2003 by F.Y. Lin and J.M. Liu [113]: the chaos bandwidth is equal to the range of frequencies that contains 80% of the total energy of the spectrum, starting from DC. Figure 3.1 (a) and (b) present an example of such measurement.

- That definition was later improved. A first possible issue with the previous definition is that if the chaos originates with a pulsed state at a high frequency, most of its energy will be far from DC, meaning fast chaos, but the system actually oscillates on a few range of frequencies. Therefore was introduced the definition of the chaos bandwidth studying the range of frequencies that contains 80% of the total energy but starting from the main frequency of the system [112]. That measurement is presented in Fig. 3.1 (c) and (d).

- However that later definition will still conclude on a broadband chaos altough the spectrum may just have two frequency peaks far from each other. Therefore, a new definition was introduced, considering the sum-up of the discrete components of the spectrum that contains 80% of the signal energy [112]. That new kind of chaos bandwidth is named effective bandwidth. It is presented in Fig. 3.1 (e) and (f). The easiest method to calculate the effective bandwidth from a spectrum is to sort the spectrum in descending order and then calculate its chaos bandwidth.

3.1.1.2 State of the art

Since the chaos bandwidth was defined, many results have tried to improve it in chaotic optical sources. In general the chaos obtained by a single laser diode with optical feedback has a bandwidth limited by the laser relaxation oscillation frequency [110]. In the study by F.Y. Lin and J.M. Liu that first introduced chaos bandwidth [113], the system was a laser subjected to both optoelectronic feedback and optical injection (Fig. 3.2 (c)) and they obtained a bandwidth of 20.5 GHz. When using COF and optical injection, a chaos bandwidth of 17 GHz was typically measured [117]. Zhang et al. proposed an experiment using dual wavelength-injection in laser diode also subjected to feedback amplified by an EDFA, and generated a chaos bandwidth of 32 GHz [118]. To obtain wideband chaos, another solution is triple injection: one laser with COF injects its output into a second laser, which itself inject a third laser. Sakuraba et al. reported a chaos bandwidth of 35 GHz [114]. Using mutual injection between two lasers, Qiao et al. obtained a chaotic signal with a bandwidth superior to

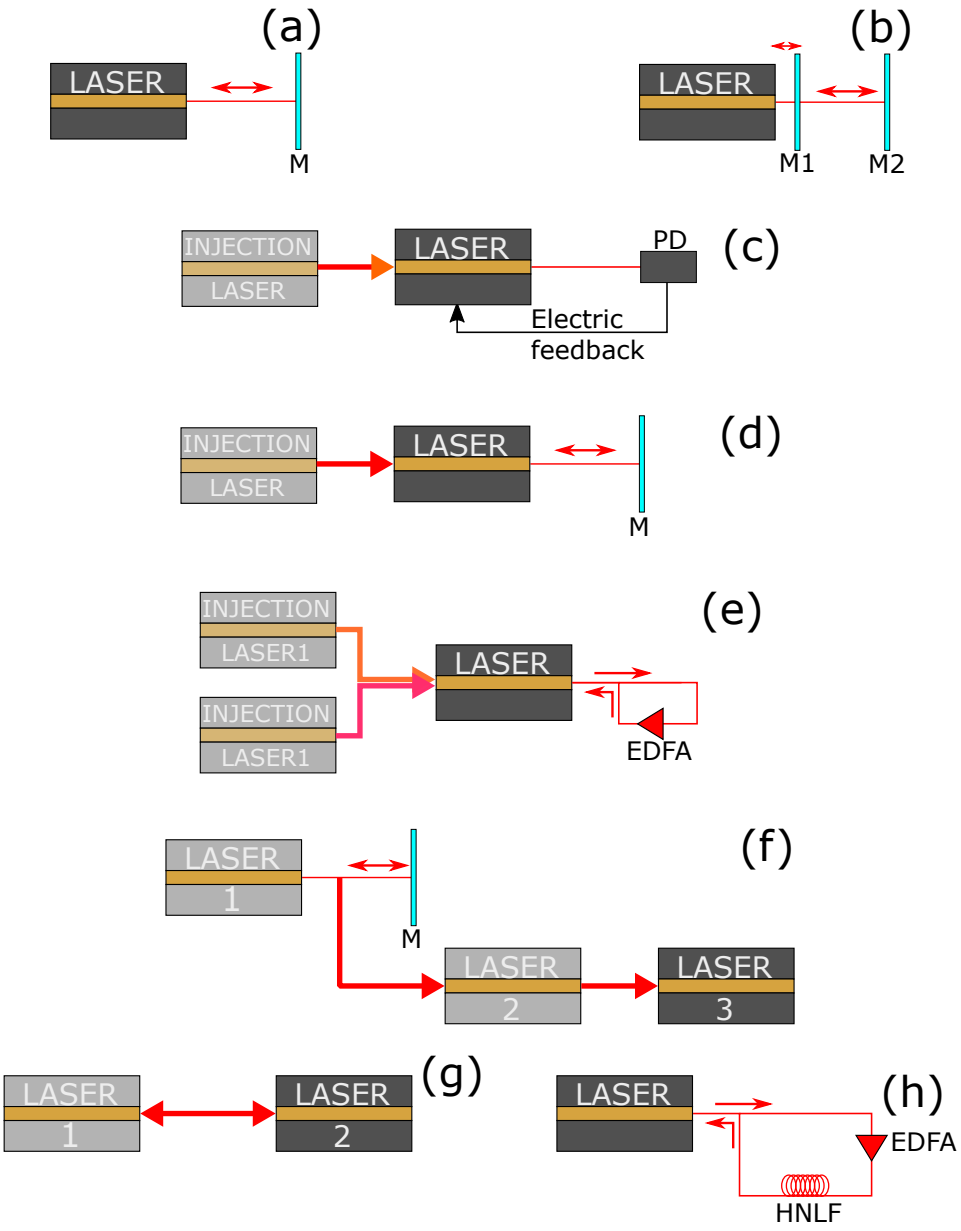

Figure 3.2: Various configurations mentioned in section 3.1.1.2. The symbol M (or M1/M2) indicates a mirror, PD a photodiode, EDFA an erbium doped fiber amplifier and HNLF a high nonlinear optical fiber. (a) COF (Refs. [114, 115]), (b) dual COF [116], (c) injection and opto-electric feedback [113], (d) injection and COF [117], (e) dual wavelength injection in laser with active feedback [118], (f) cascaded injection [114], (g) mutual coupling [119] and (h) a laser subjected to non-linear active feedback [120].

38 GHz [119]. The same group proposed an experiment using an active feedback loop with an EDFA and a high nonlinear fiber: they reported a bandwidth close to 39 GHz [121]. However, all these experiments, whose configuration is shown in Fig. 3.2 (c-h), require active components to improve the destabilization of the laser.

Of more fundamental interest is therefore the question of the chaos bandwidth in a single laser with feedback. A typical laser under COF (Fig. 3.2 (a)) exhibits chaos with a bandwidth inferior to 12 GHz [114, 115]. In 2017, Schires et al. used a laser diode with both ultra-short and long external cavities (Fig. 3.2 (b)) that enables to generate chaos with a bandwidth of 16 GHz. However, they used a specifically designed laser with a relaxation oscillation frequency being pushed towards 14 GHz [116].

In 2016, members of our group studied the bandwidth of the chaos generated by a PCF system, and compared it to COF. They observed that the chaos bandwidth of PCF chaos is superior to the one of COF chaos on the range of feedback strength they studied [56]. However, the maximum value of feedback strength was limited by the PCF configuration used (ring-PCM, see Ref. [95]) and the chaos bandwidth measurements were limited by the bandwidth of the photodiode (12 GHz) [56]. Further numerical analysis with a simplified PCF model without accounting for the mirror finite penetration depth (see section 1.3.1) confirms that the chaos bandwidth of chaotic PCF was superior to COF. It also predicted a quasi-continuous increase of the chaos bandwidth as the feedback increases [64]. These studies from our group therefore motivate the idea that replacing conventional mirrors by PCM would significantly extend chaos bandwidth for a fixed f_{RO}, which is a significant paradigm shifting approach!

3.1.2 Spectral flatness: another indicator of complexity

Apart from the chaos bandwidth, it is important to known how the frequencies are distributed in the range of frequency inside the chaos bandwidth. Therefore, we use what is called the spectral flatness. A common definition in laser dynamics is to consider the distance between the maximum and the minimum values of the power spectrum, in decibels [122]. It works well with chaotic

spectrum measured by a RF spectrum analyser. However, that definition proved to be less effective when studying the spectrum generated from measured time series, which is our case. The electronic noise of the oscilloscope leads to possibly strong fluctuations of the power spectrum energy versus the frequency.

On the contrary the spectral flatness is defined in signal processing as the ratio of the geometric mean of the power spectrum by the arithmetic mean [123]:

$$SF = \frac{\prod_{n=1}^{N} f(n)^{\frac{1}{N}}}{\frac{1}{N}\sum_{n=1}^{N} f(n)} \tag{3.1}$$

where $f(n)$ is the n-th discrete component of the Fourier spectrum and N is the length of the discrete Fourier spectrum.

A spiky spectrum will have a spectral flatness close to 0 and a white-noise will have a spectral flatness close to 1. Notice that the white-noise has a perfectly flat spectrum only in expectation: the values are always distributed around that expectation and the spectral flatness is typically inferior to 1. The spectrum of a perfect chaos should looks like the one of a white noise, meaning all the frequencies are present in the time traces.

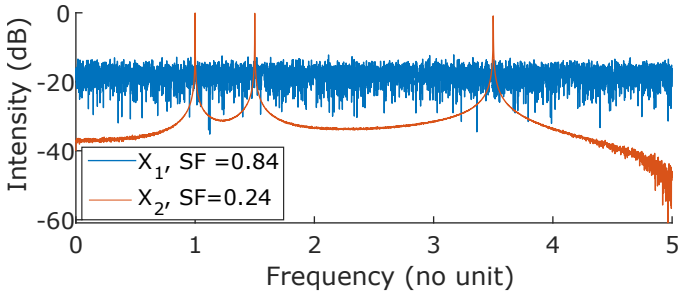

Figure 3.3: Example of the spectral flatness obtained from two RF spectra.

Figure 3.3 presents an example of a spectrum obtained from two time series X_1 and X_2, generated by:

$$X_1(t) = \xi_1(t) + R\xi_2(t); \tag{3.2}$$

$$X_2(t) = cos(2\pi t) - cos(3\pi t) - cos(5\pi t) + R\xi_3(t) \tag{3.3}$$

where ξ_1, ξ_2 and ξ_3 are decorrelated white gaussian noises. The spectral flatness of X_1 is 0.84 and the spectral flatness of X_2 is 0.19.

In the field of chaotic laser diodes, the spectral flatness is generally calculated on the 80% most significant part of the spectrum (i.e. the part inside the chaos bandwidth), to avoid calculating spectral flatness on high-frequency sections of the spectrum that would not be used in real applications [64, 122]. We follow that approach. Since we use the general definition of spectral flatness and not the one used by the studies on chaotic laser diodes, we do not have results to compare with the existing literature. Only Ref. [64] predicted a maximum spectral flatness of 0.82 in PCF and 0.72 in COF, using our definition.

The spectral flatness is generally used as a secondary indicator with respect to chaos bandwidth and we will not always mention the flatness when studying chaos bandwidth, for instance in section 3.3.1.

3.2 Preliminary results

We use the experimental setup presented in chapter 2, section 2.2. During my PhD thesis, we have used two different devices to record the time series.

- The first one used a photodiode model Newport 1414-50 and a Tektronix DPO72304SX oscilloscope. The photodiode has a 3 dB bandwidth of 24.5 GHz while the oscilloscope has a bandwidth of acquisition of 23 GHz and a sampling rate of 50 GSample/s. That later value means the Fourier spectrum will extend up to 25 GHz.

- To further increase the bandwidth of analysis, the 23 GHz bandwidth oscilloscope was replaced by a 36 GHz oscilloscope (Teledyne LeCroy 10-Zi-36) and the photodiode by a Newport 1474-A, AC coupled and whose 3 dB bandwidth is 38 GHz. The sampling rate of the oscilloscope is 80 GSample/s and the Fourier spectrum will extend up to 40 GHz.

The results of Ref. [56] were obtained with a 12.5 GHz photodiode, so both of our new setups enable us to measure higher chaos bandwidths.

Two lasers have also been used. First, a JDS-Uniphase SDL-5420, whose characteristics have been given section 2.2.2.2. Later, that laser stopped lasing and was replaced by a JDS-Uniphase SDL-5410, presented section 2.2.2.1.

3.2.1 First example with a 23 GHz oscilloscope

As an example of measurement, we study two time series obtained at different feedback strengths (named F here). We used the SDL-5420 laser under a pump current of 50 mA, i.e. 3.6 times the threshold (13.9 mA). At this operating point, the frequency of the relaxation oscillations f_{RO} is 3.9 GHz. The cat-mirror was placed at a distance of 53.5 cm from the laser cavity, so the cavity round-trip frequency f_{EC} is 280 MHz. The time trace measurement setup is made of the 23 GHz oscilloscope and the 25 GHz photodiode.

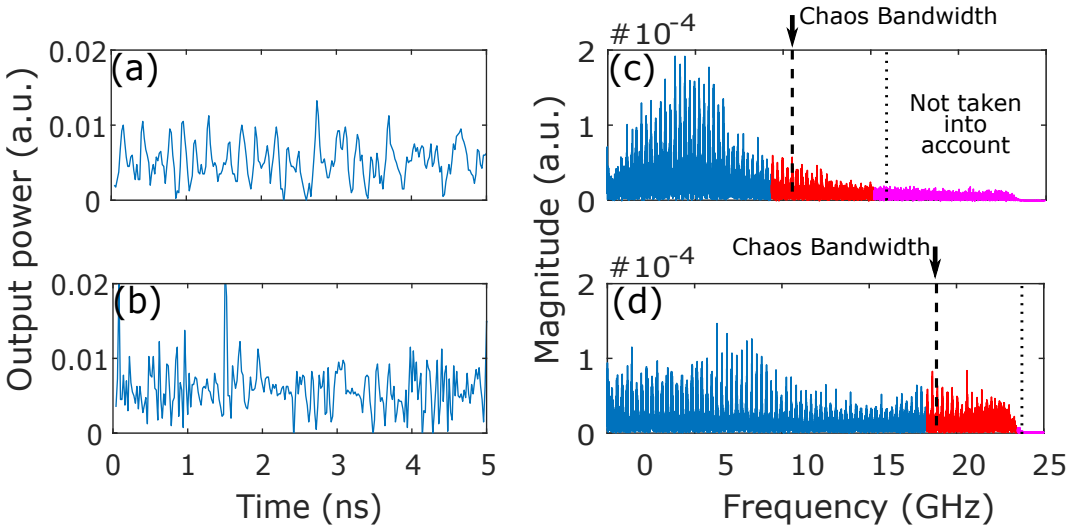

Figure 3.4: Time-traces of laser output power (left) and corresponding RF spectra (right) for different phase-conjugate feedback strengths. (a) and (c) have been recorded at $F = 0.46\%$, (b) and (d) at $F = 4.6\%$. The purple part (left of the thin dotted line) of the spectrum was ignored. The blue part of the spectrum (left of the dashed line) contained 80% of the total energy, the red part 20%. Figure taken from Ref. [99].

We display in Fig. 3.4 (a) and (b) a small part of the time traces. The corresponding spectra are given in (c) and (d). The RF spectrum of these

time traces show resonances at frequency components at multiples of the cavity round-trip frequency (280 MHz). This is a well-known feature of the chaos generated by lasers with feedback, that can also be observed in the autocorrelation function of the time traces. It can be reduced using various methods, such as additional feedback [124] or a choice of f_{EC} close to f_{RO} [125]. In our case, it is a good way to verify the value of F_{EC}.

To compute the chaos bandwidth, we proceed in two steps. First we remove the noisy high-frequency part of the spectrum. In laser dynamics experimental measurements, the noise is mostly electrical noise, created by the photodiode and the oscilloscope. In typical determination of the chaos bandwidth, the spectrum is determined by a RF spectrum analyser and the authors substract the spectrum of the noise from the spectrum of the chaotic signal. We cannot use such method with our spectrum obtained from the time traces. Indeed, we did not use a RF spectrum analyser because its measurement time would be too slow when compared with the spontaneous variations of the reflectivity of the PCM (see section 2.1.4). Therefore, we choose not to study the high-frequency part of the spectrum whose average energy on a range of 500 MHz is inferior to the average energy of the noise. That removed part is colored in magenta in Fig. 3.4.

Second we calculate the chaos bandwidth. The blue part contains 80% of the energy of the useful spectrum and the red part the remaining 20%. The chaos bandwidth is shown with an arrow.

At low feedback (i.e. $F = 0.46$ %, see Fig. 3.4 (a)) the laser exhibits a chaotic behavior. Most of the energy is concentrated around f_{RO} (3.9 GHz), indicating the chaos is created by the destabilization of the relaxation oscillations. The chaos bandwidth achieved in Fig. 3.4 (c) is equal to 9.4 GHz. Fig. 3.4 (d) presents the RF spectrum at a higher F (around 4.6 %). The laser is still chaotic, but it features a better distribution of the energy. Consecutively, it has a significantly larger chaos bandwidth, equal to 18.3 GHz. That later value is close to the measurement limit: as the oscilloscope has a bandwidth of 23 GHz, the limit chaos bandwidth will be around 18.4 GHz (80% of 23 GHz). The presence of high frequency components can also be hintered from the evolution of the output power, whose variations are faster in Fig. 3.4 (b) than in Fig. 3.4 (a).

3.2.2 Another example with a 36 GHz oscilloscope

We present here another example of chaos bandwidth measurements, obtained with another laser (SDL-5410), a shorter cavity (14.7 cm, $f_{EC} = 1.02$ GHz) and the measurement apparatus with a higher bandwidth (36 GHz oscilloscope and 38 GHz photodiode). The laser threshold current is 14.9 mA and it was operated at 40 mA ($f_{RO} = 4.8$ GHz).

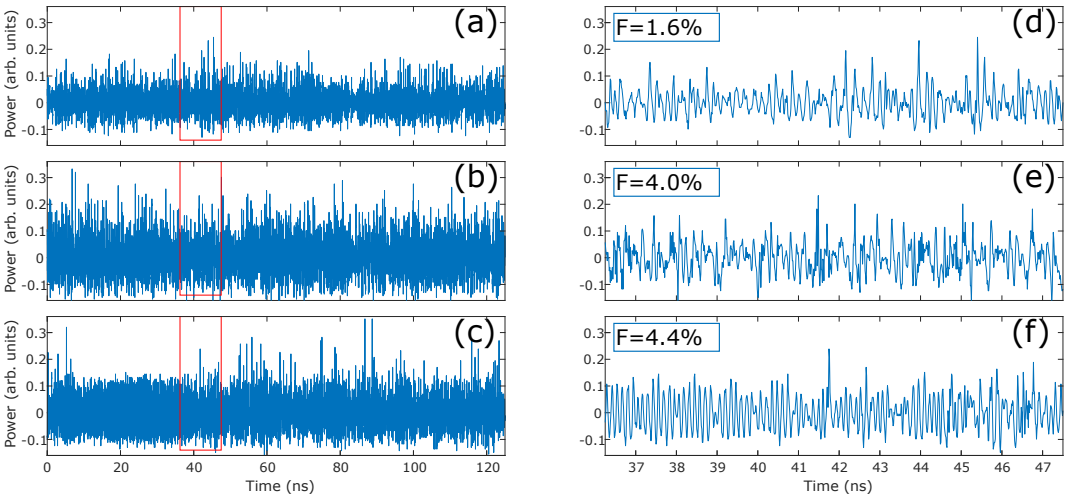

Figure 3.5: Time traces of the laser output power at three values of feedback strength. The pumping current is set at 80 mA and the delay length at 0.98 ns. (d-f) are zooms on the region marked with a red square on (a-c). Figure taken from Ref. [103].

The better sampling time of the oscilloscope (80 Gsample/s instead of 50) enables a better view on the time traces. The time traces of three measured time series are shown in Fig. 3.5. Figures 3.5 (a)-(c) show a 120 ns subset of the acquired time traces (on a total length of 1 μs). Figures 3.5 (d)-(f) shows a zoom on the red-squared zones from Figs. 3.5 (a)-(c). The corresponding spectra are given in Figs. 3.6 (a)-(c).

Figures 3.5 (a) and (d) were measured under weak feedback , here $F = 1.6\%$ (notice that the laser changed from section 3.2.1 and feedback strengths are therefore not exactly similar). The time trace displays irregular pulsations with intensity peaks generally separated by around 160 to 200 ps, see for instance the oscillations between 42 and 43 ns. That observations is confirmed by the

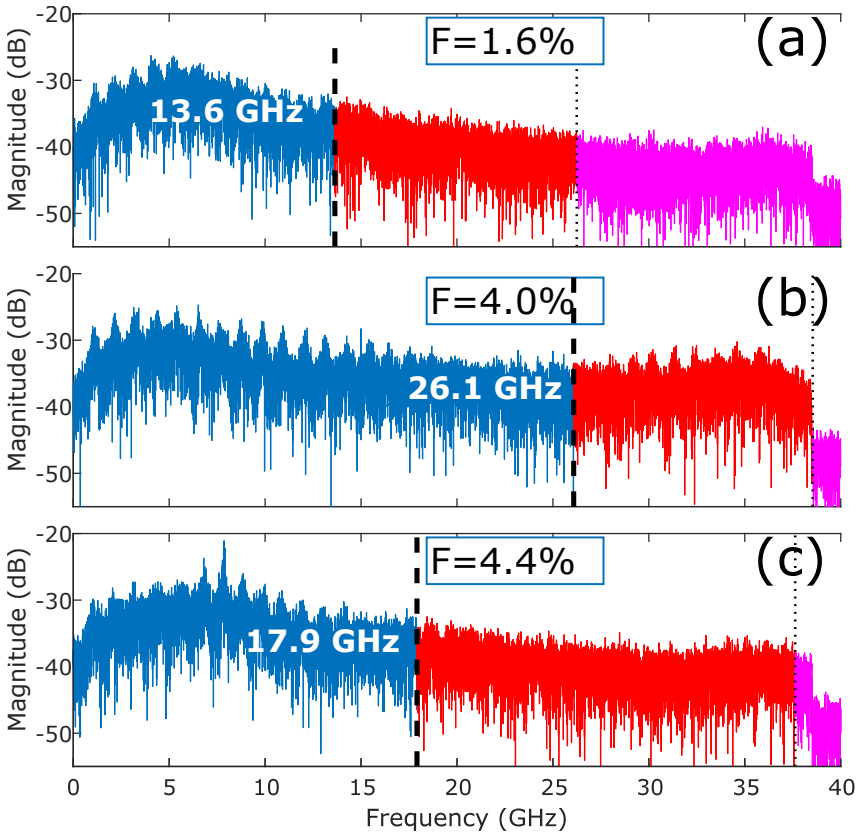

Figure 3.6: Spectra of the laser output powers, corresponding to the time traces of Fig. 3.5 (a)-(c), at several values of feedback strength, delay and pump current. The chaos bandwidth is indicated in white and corresponds to the span of frequencies of the blue part of spectrum (until the vertical dashed line), that contains 80% of the energy of spectrum. Figure taken from Ref. [103].

RF spectrum, shown in Fig. 3.6 (a): most of its energy is centered around 5 GHz, close to $f_{RO} = 4.8$ GHz. The spectrum also displays some energy at lower levels in the higher frequencies and consequently faster dynamics can be observed on the time traces. They are particularly visible between 43 and 44 ns on Fig. 3.5 (c). The RF spectrum of the chaos is similar to what would be obtained with COF [119] and its chaos bandwidth is 13.6 GHz. We also calculate the spectral flatness. We obtain a value of 0.74, which shows that the energy is well distributed in the limited range of the chaos bandwidth.

Figures 3.5 (b) and (e) are for higher feedback strengths. One can notice

the time traces displays both "slow" (≈200 ps) and faster variations, hence the chaos encompasses a wider range of time scales. As a consequence, the spectrum, shown in Fig.3.6 (b), displays higher frequencies with a good distribution. The chaos bandwidth rises to 26.1 GHz while the spectral flatness is equal to 0.71. In simulations of Ref. [64], the spectral flatness decreases for high values of chaos bandwidth but our experience shows the spectral flatness remains high.

As the feedback is further increased in Figs. 3.5 (c) and (f), the laser is at the edge of a dynamical change and follows an intermittent destabilized limit cycle, mixing chaos and regular oscillations. Between 18 and 41 ns, the output power is close to periodic, with a period of approximately 150 ps (frequency of 6.8 GHz) while at longer times the signal is highly chaotic. The system goes back and forth between chaos and quasi-periodicity and an analysis of the full time series can confirm it. Figure 3.5 (f) is taken close to the bifurcation point and shows that, each nanosecond, the quasi-periodic signal is interrupted for a few picoseconds. This duration of 1 ns is a clear signature of the time delay. The spectrum shown in Fig.3.6 (c) is remarkable because it features clear peaks at 6.80 and 7.86 GHz alongside standard chaotic spectrum. The frequency of 7.86 GHz is probably related to other regions of quasi-periodicity that are not visible the small part of the time series displayed in Fig. 3.5 (c). The flatness of the spectrum is equal to 0.71, which is the same value as in Fig. 3.6 (b) but the chaos bandwidth is here lower.

3.3 Evolution of the chaos bandwidth versus the feedback strength

3.3.1 Experimental result

In that section, we use the configuration of section 3.2.1: the oscilloscope has a bandwidth of 23 GHz, the laser is the SDL-5420, pumped at 50 mA and f_{EC} = 282 MHz. We did not calculate the spectral flatness of our time traces.

As we explained in section 2.1, the reflectivity of our PCM varies over time,

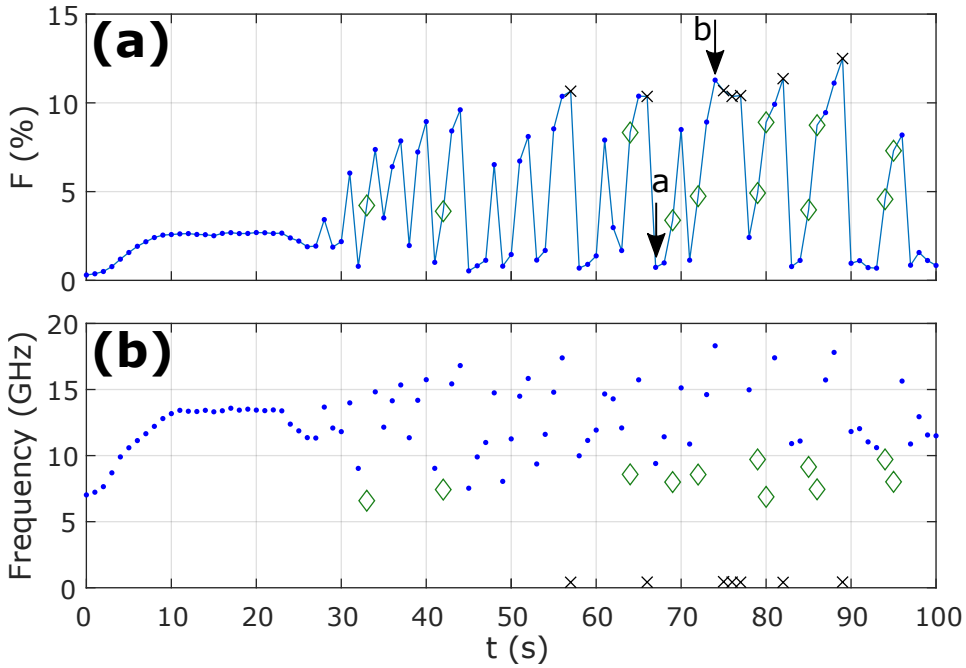

Figure 3.7: Evolution of (a) the feedback strength F and (b) the chaos bandwidth versus time. Dots are for chaotic dynamical states, diamonds for ECMs and crosses for stationary states. For self-pulsing states, the frequency is not the chaos bandwidth but the frequency of the main ECM. Arrows a and b indicates the time series presented in Fig. 3.4 (a) and (b). Figure taken from [99].

at a tenth of a second time scale. Therefore, the feedback strength is naturally tuned during an experiment if one time series is measured each second. Since the time series are 2 μs long, we consider that the feedback strength is constant on this short range.

We obtained three types of dynamics, as explained in section 1.3. The main measured dynamics are the chaotic states, which are the core of the study of this chapter. Two other dynamics are also obtained when the feedback strength varies freely: restabilized steady-states at high values of feedback strength, and ECMs, the self-pulsing states that will be described in chapter 5. We display these ECMs in Fig. 3.7, with a green diamond. Similarly, a black cross means steady-state time series. The ECMs being self-pulsing states, the frequencies displayed in Fig. 3.7 (b) for the self-pulsing states are the fundamental frequency of the self-pulsations.

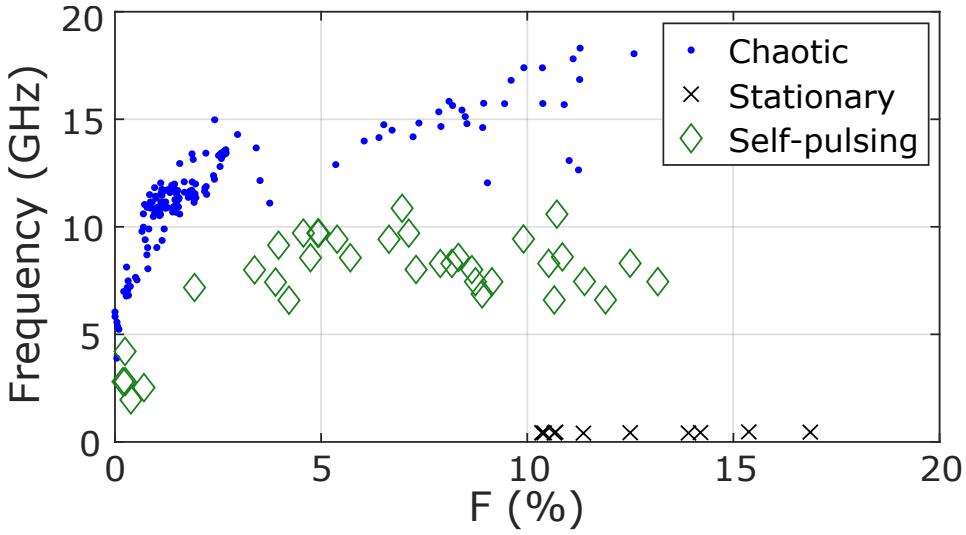

Figure 3.8: Experimental evolution of the chaos bandwidth versus F. For regular self-pulsing states (diamonds), the reported frequency is not the chaos bandwidth but the frequency of the ECM. Figure taken from Ref. [99].

From the data such as those presented in Fig. 3.7, we can plot the evolution of the chaos bandwidth versus the feedback strength F. It is presented in Fig. 3.8. As the reflectivity of the PCM is varying continuously, there is some uncertainty in the measurement of F (around 0.5%). First, we observe that for very low feedback strength $F < 0.5\%$, the chaos has a low chaos bandwidth and coexists with undamped relaxation oscillations, i.e. diamonds with a frequency around 4 GHz. The chaos bandwidth is really low, around 5 or 6 GHz. Then, the chaos bandwidth linearly increases with the increase of F while $F < 3\%$. At $F \approx 3\%$, the chaos bandwidth reaches a value of about 15 GHz. That value, equal to 3.8 times f_{RO}, is higher than the one obtained with COF [114, 115]. But higher values can be obtained: for increasingly moderately large F, the chaos bandwidth shows an increase with F, though much slower than at low F values. The chaos bandwidth reaches a maximum value of about 18 GHz - i.e. close to the measurement limit - when F is close to 10%. In that range of values, the dynamics shows several regions of stable ECMs at very high harmonic frequencies of the external cavity frequency. For still larger F, the laser diode re-stabilizes to a stationary steady-state.

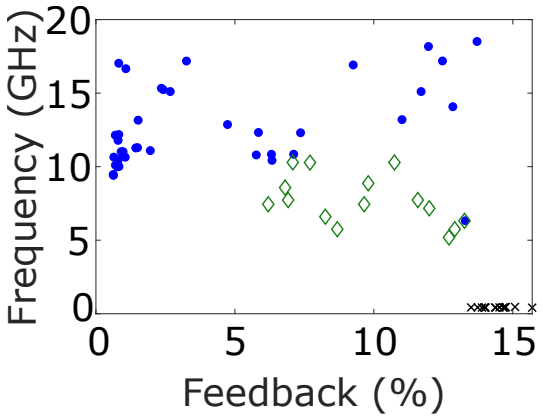

Figure 3.9: Experimental evolution of the chaos bandwidth versus F. For regular self-pulsing states (diamonds), the reported frequency is not the chaos bandwidth but the frequency of the ECM. Figure taken from Ref. [100].

That behavior is highly reproductible. We present in Fig. 3.9 another measurements done with the same setup on another day: the curve completely follows the behavior describe above.

3.3.2 Numerical confirmation: the role of the PCM finite depth penetration

We showed in section 3.3.1 that the evolution of the chaos bandwidth with respect to the feedback strength is not linear and saturates for high values of feedback strength. These findings contradict the numerical simulations performed in Ref. [64]. In that reference, our group observed that the chaos bandwidth of a PCF laser would linearly increase with the feedback strength.

Therefore, we perform another numerical investigation of the evolution of the chaos bandwidth with respect to the feedback strength. In Ref. [64], the numerical model was the unfiltered model, i.e. the simulation of a laser without accounting for the finite penetration depth. As explained in details in section 1.3.1, the finite penetration depth τ_r is the time it takes the light to penetrate the nonlinear crystal of the PCM and it is directly proportional to the length of the crystal. We use the equations of section 1.3.1 with the following parameters: $\tau_p = 1.4\ ps$, $\alpha = 2$, $P = 0.6016$, $T = 1200$ and $\tau_r = 50$. All

these values were already used in previous simulations of the behavior of our laser [67]. Considering our experimental cavity round-trip length ($L = 1.07$ m), we take $\tau = 2548 = \frac{L}{c\tau_p}$ (c is the speed of light). We choose $\gamma \in [0\ 0.06]$ and set two values of τ_r: 1 and 50. $\tau_r = 50$ corresponds to a PCM with a length of 5 mm [52]. $\tau_r = 1$ actually corresponds to unfiltered PCF in our simulations, the cut-off frequency of the feedback being equal to the time step of our algorithm.

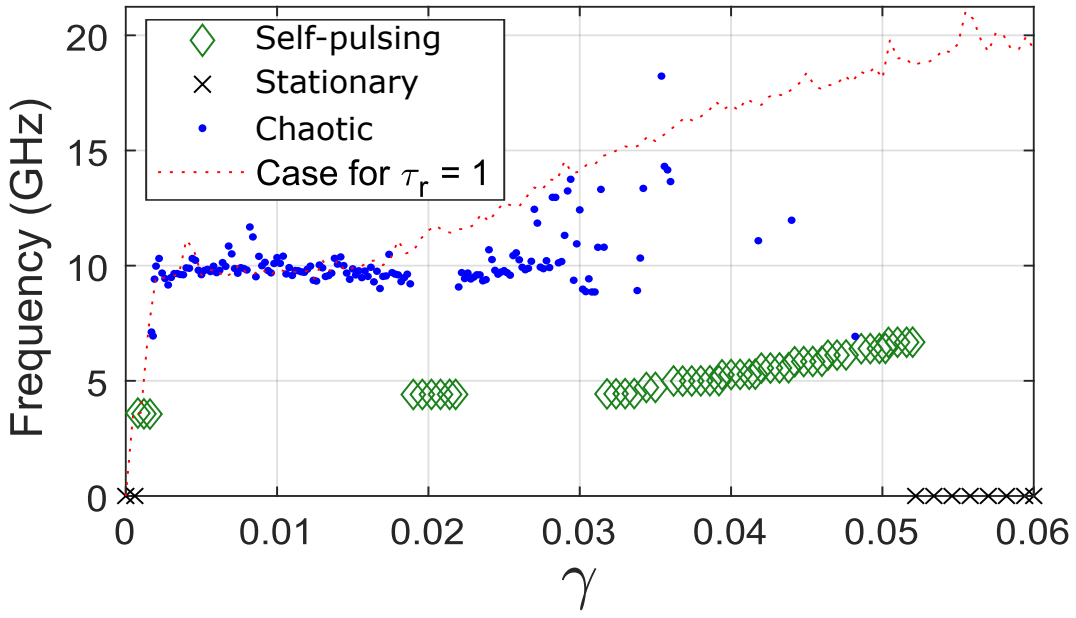

Figure 3.10: Theoretical variation of chaos-bandwidth (for chaotic state) and oscillation frequency (for self-pulsing states) of a laser with filtered PCF, versus the feedback rate κ. The red dotted line is the chaos bandwidth of an instantaneous PCF. Figure taken from Ref. [99].

We plot in Fig. 3.10 the chaos bandwidth versus γ. As in Fig. 3.8, we differenciate the dynamics obtained for $\tau_r = 50$: stable steady-state are indicated with black crosses, regular self-pulsing dynamics are indicated with green diamonds and chaotic states with blue dots. The indicated frequency is the chaos bandwidth for the chaotic states and the frequency of the main period of the system for regular self-pulsing states. For $\tau_r = 1$ (unfiltered), the system only displays chaos (except when $\gamma < 0.001$). It does not mean ECMs do not exist but they are unstable [65]. Therefore we plotted in red dotted line the evolution of its chaos bandwidth.

At low feedback ($\gamma < 0.015$), the chaos bandwidth is similar for filtered and unfiltered PCFs. From $\gamma = 0.02$, external cavity modes appear. The bandwidth of the unfiltered case follows a monotic linear increase with feedback strength, as previously reported by Ref. [64], while the bandwidth of the filtered PCF saturates with the feedback strength, as experimentally reported. However, chaotic states still appear between succesive ECMs and can present very high bandwidths, such as 18.23 GHz at $\gamma = 0.0354$.

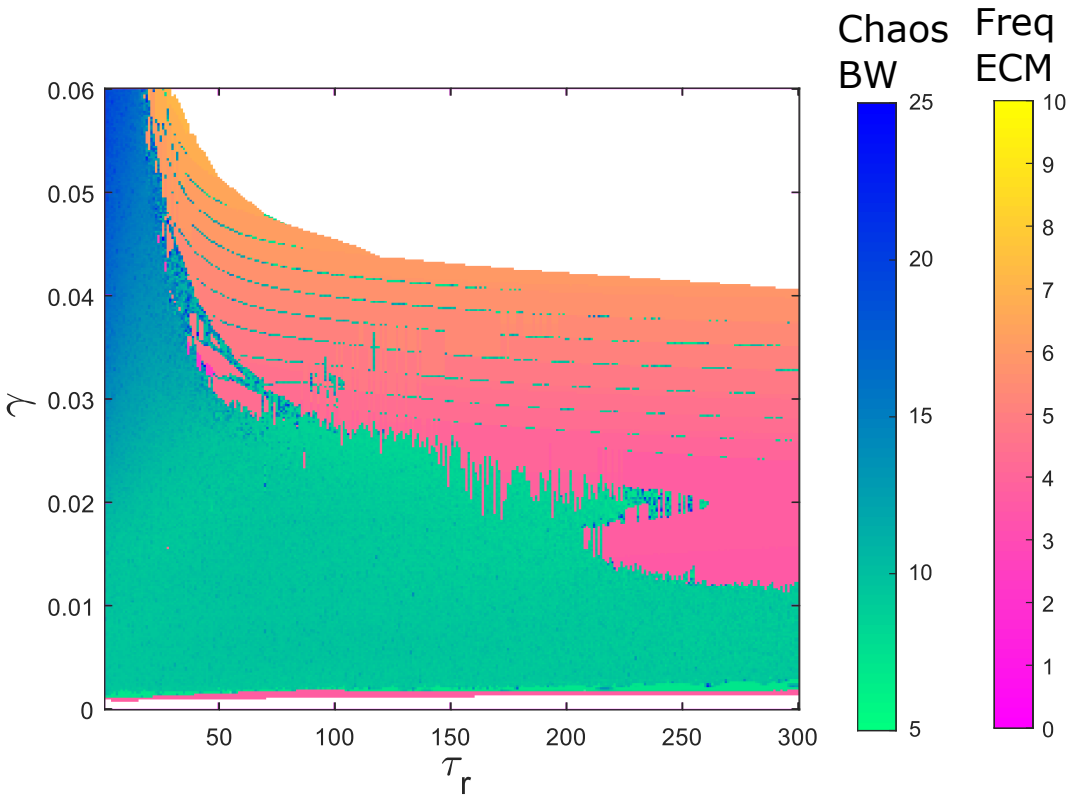

Figure 3.11: Influence of the finite penetration depth τ_r (horizontal axis) and of the feedback strength γ (vertical axis) on the frequency of the external cavity modes for the self-pulsing states (pink to yellow color-scales, in GHz) and on the chaos bandwidth (green to blue color-scales, in GHz). The steady-states are displayed in white. Figure taken from Ref. [107].

We then performed an even deeper analysis. We decided to study the evolution of the chaos bandwidth versus γ for a large set of τ_r. Therefore, we present in Fig. 3.11 the value of the chaos bandwidth (for chaotic states) or the

frequency of the ECM (for regular self-pulsing states) versus γ and τ_r. All the parameters are the same than above. The white zone of the map indicates the steady-states. The chaos bandwidth is measured in green to blue color scale and the frequency in magenta to yellow. A similar map was already published in Ref. [67], displaying only the frequency of the ECMs. Our map enables comparison between the properties of ECMs and of chaos in the plane of the system parameters.

The conclusion that can be drawn from Fig. 3.11 confirms those of Fig. 3.10. First, filtering the feedback through the finite penetration depth reduces the chaos bandwidth. Indeed, for $\tau_r < 10$, broadband chaos (up to 25 GHz) can be obtained for $\gamma \approx 0.05$ and larger values of γ. However, reducing τ_r requires a shorter phase-conjugate mirror, and this may complicate the achievement of high feedback values because the PCM efficiency is directly related to the interaction length between the beam in the nonlinear medium. Second, the restabilization occurs for lower values of γ when τ_r increases. That limits both the frequency of the higher ECM and the maximum of chaos bandwidth. Third, high values of chaos bandwidth can be reached in the bubbles of chaos between successive ECMs. That later observation shows the link between the existence of the PCF ECMs and the fact the chaos bandwidth in PCF is higher than in COF.

3.3.3 Conclusion

We have reported in this section two new results about the chaos bandwidth of phase-conjugate feedback. First, we reported that PCF enables high chaos bandwidths, up to 18.3 GHz. It is higher than those of COF, the only limit being the measurement bandwidth. We also report an experimental saturation of the chaos bandwidth. Numerical simulations unveiled the influence of the finite penetration depth in the laser in explaining such saturation. It opens new perspectives in the generation of broadband chaos with PCF, for instance with mirror featuring a smaller finite penetration depth, i.e. nonlinear media with smaller interaction lengths.

3.4 Study of the effective chaos bandwidth

3.4.1 Experimental observations

We now investigate the effective chaos bandwidth of a PCF system. We use in that section the SDL-5420 laser, pumped at 80 mA (f_{RO} = 5.2 GHz). The cavity is 1.545 m long (f_{EC} = 97.07 MHz) and the oscilloscope has a 36 GHz bandwidth and a sampling rate of 80 GSample/s. We have measured around 5000 different time traces and for the sake of clarity we have kept ≈60 time series, choosing the most representative time spans of the dynamics. As in the previous section, we do not consider in the energy calculation the noisy high frequency part of the spectrum. We sort the spectrum in descending order and then determine the part that contains 80% of the total energy, starting from the highest values of the spectrum.

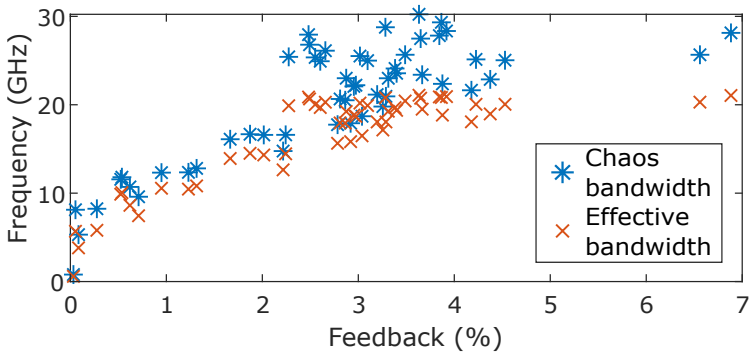

Figure 3.12: Evolution of the chaos bandwidth (blue stars) and the effective chaos bandwidth (red crosses) versus the feedback strength. Figure taken from Ref. [101].

The evolution of the chaos bandwidth and the effective chaos bandwidth is displayed in Fig. 3.12. The chaos bandwidth (blue stars) follows the same trend than in the previous section: it increases until the feedback $F = 2.2\%$ and then shows saturation. The observed maximum chaos bandwidth value is 30.2 GHz, which is the largest chaos bandwidth measured to our knowledge in laser with passive feedback. The effective chaos bandwidth follows the evolution of the chaos bandwidth when $F \leq 2.2\%$. However, it has a different behavior in the range $2.2\% \leq F \leq 5\%$: both the chaos bandwidth and the effective chaos

bandwidth increase but the enhancement of the effective chaos bandwidth is not as strong as the one of the chaos bandwidth. Still, the values of effective chaos bandwidth are often equal to ≈ 20 GHz in the range $2.2\% \leq F \leq 5\%$ while a typical laser with COF has an effective chaos bandwidth of 9.6 GHz [114]. The effective chaos bandwidth we obtain with PCF is even larger than the one reported in the case of chaos from a laser with both feedback and injection (13.8 GHz) [114].

3.4.2 Numerical simulations and the role of the destabilized ECMs

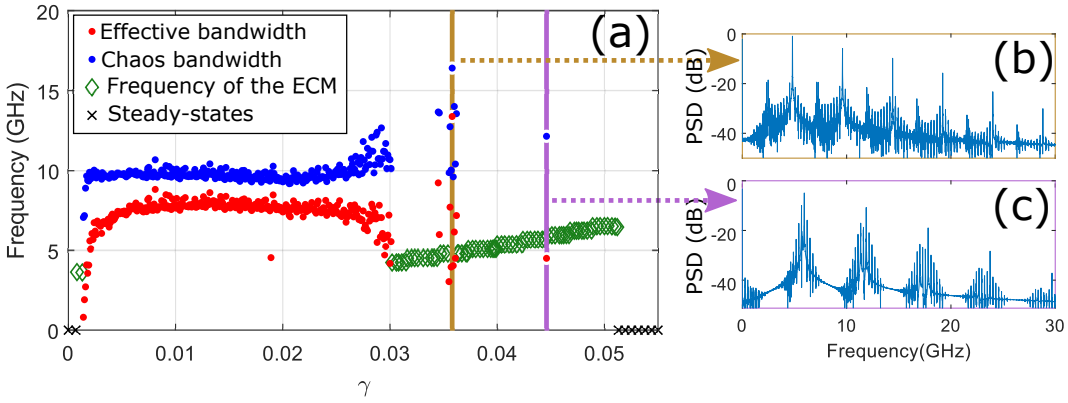

Figure 3.13: (a) Evolution of chaos bandwidth and effective (chaos) bandwidth (for chaotic states) and oscillation frequency (for ECMs) for a typical laser with PCF. (b) and (c) present the power spectral density (PSD) for $\gamma = 0.0358$ (brown line on (a)) and $\gamma = 0.0446$ (violet line on (a)). Figure from Ref. [107].

To confirm the experimental results, we now numerically study the evolution of the effective chaos bandwidth and compare it with the chaos bandwidth. The parameters are the one of section 3.3.2. Figure 3.13 (a) shows the evolution of the chaos bandwidth (blue dots), the effective chaos bandwidth (red dots) and the frequency of the ECMs (green diamonds) versus the normalized feedback strength γ. If a state is chaotic, both the effective chaos bandwidth and the chaos bandwidth are indicated.

Like in experiment, the chaos bandwidth and the effective chaos bandwidth follow the same trend until $\gamma = 0.025$. From $\gamma = 0.025$, the chaos bandwidth increases as the ECMs become stable at $\gamma = 0.03$. High value of chaos bandwidth (16.4 GHz) and effective chaos bandwidth (13.4 GHz) are obtained at $\gamma = 0.0358$, indicated with a brown vertical bar. The corresponding RF spectrum is displayed in Fig. 3.13 (b). The peak of the spectrum is at a frequency of 4.8 GHz and harmonics while lower peaks are visible at 2.4 GHz and harmonics. Since 4.8 GHz is the frequency of the ECM that appears at $\gamma = 0.0357$, we conclude that the wideband chaos we report at $\gamma = 0.0358$ is created by a destabilized ECMs, with the signature of period doubling (peak at 2.4 GHz). However, in that region, the effective chaos bandwidth can become very low while the chaos bandwidth remains high. A good example can be found at $\gamma = 0.0446$ (violet vertical bar): the chaos bandwidth equals 12.15 GHz while the effective chaos bandwidth is as low as 4.5 GHz. Therefore, we display in Fig. 3.13 (c) the spectrum of that time series. The energy is centered around 5.91 GHz, which is as previously the frequency of the next stable ECM,. However, the spectrum does not show new frequencies created by period doubling and most of its energy is centered around 5.91 GHz and 11.82 GHz. That explains the lower value of effective chaos bandwidth, while the chaos bandwidth remains high since there is no energy in the low frequency part of the spectrum (from DC to 5 GHz).

It is also highly interesting to observe that simulations predict that, in the region of the ECMs, the spectrum of the chaotic states is centered on the frequency of the neighbour ECMs. However, experimental spectra, such as those of Figs. 3.4 and 3.6, do not display any large peak around those frequencies.

3.5 Influence of the delay on the chaos bandwidth and the spectral flatness

3.5.1 Experimental observations

In that section, we reuse the setup used in section 3.2.2. The bandwidth of the oscilloscope is 36 GHz, the laser is the SDL-5410 and it is pumped at 80 mA.

To our knowledge, there has been no study of the influence of the feedback delay on the chaos bandwidth. On the other hand, it has been demonstrated that a wise choice of delay can highly reduce the time delay signature (TDS) [125]. However, the question remains of the behavior of the chaos bandwidth: does it decrease with delay? Can broadband chaos be obtained at all values of delay?

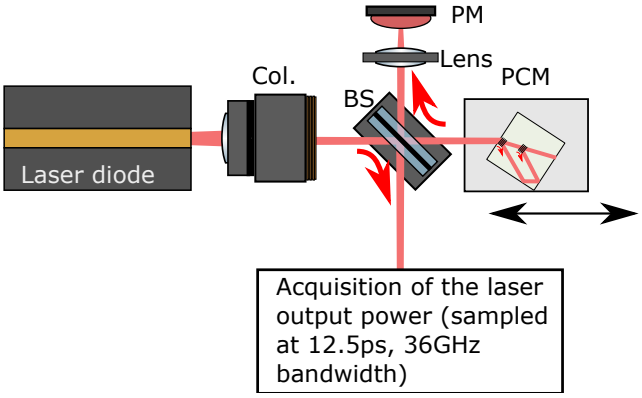

Figure 3.14: The experimental setup used in that subsection, and its components. The support of the phase-conjugate mirror (PCM), represented in light green, is as close as possible to the mount of the beam splitter (BS). In the illustration, the single-trip distance between the output of the EEL (edge-emetting laser) and the PCM is 14.7 cm.

Therefore, we investigated the evolution of the chaos bandwidth and spectral flatness versus the delay. Two values of delay have been chosen: 3.55 ns and 0.98 ns, corresponding to $f_{EC} = 282$ MHz and $f_{EC} = 1.02$ GHz. That later value is the shortest that can be obtained with our setup since a beam splitter has to be placed between the mirror and the laser to measure the feedback

strength (Fig. 3.14). The 14.7 cm distance between the laser and the crystal is occupied by a collimating lens and a beam splitting plate.

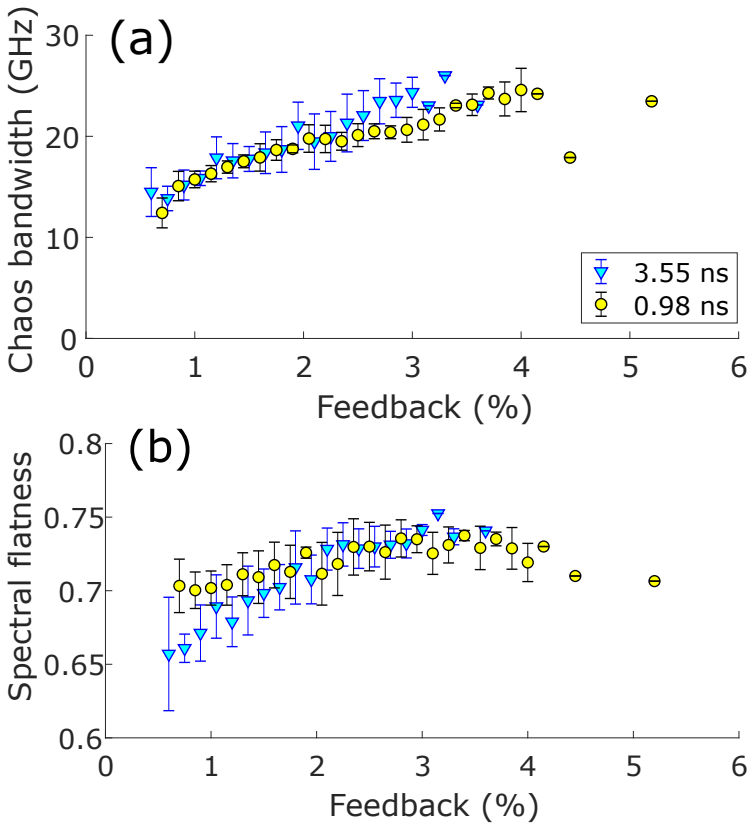

Figure 3.15: Evolution of (a) the average chaos bandwidth, (b) the average spectral flatness. The pump current is set at 80 mA. Experiments have been performed with two values of delay: 3.55 ns (blue triangles) and 0.98 ns (yellow circles). Figure taken from Ref. [103].

We still use the method of section 3.3.1: we concatenate the data from various time series, a time series being measured each half-second and the feedback strength varies following the spontaneous slow variations of the PCM reflectivity. Since we have more time traces than in the previous section, we divide the experimental range of feedback strength in intervals long of 0.15%. In each interval of feedback strength values, several time series have been measured and the displayed chaos bandwidth is the average value of the different values of chaos bandwidth obtained. The same method is used for the

spectral flatness. We also indicated with a bar associated the standard deviation when computing the chaos bandwidth or spectral flatness for different time series. No bar means that only one time series was recorded for that specific feedback strength. To improve the readability, the ECMs have not been shown in the graph, nor the steady states.

As it can be seen from the error bars, there is some deviation from the average value of bandwidth or flatness at a given feedback value. It is caused by the multi-stability between the different dynamics of the PCF (see Refs. [44, 65] and chapter 5). The variations of the chaos bandwidth are rather limited but those of the spectral flatness are stronger. It is particularly the case for the 3.55 ns delay (blue triangles) at low feedback strengths but the amplitude of these variations decrease if the feedback strength increases. Anyway, these variations do not prevent the observation of the trends of the evolution of chaos bandwidth.

The overall trend is that the chaos bandwidth does not vary much when the time delay changes. The chaos bandwidth increases with the feedback strength and slowly saturates when the feedback strength F becomes superior to 3%. It is completely similar to what we described in the previous section (3.3.1) and in Ref. [56] with other lasers and it remains true even when changing the delay. The spectral flatness also increases until the feedback strength equals 3% but then decreases with the feedback strength. That decrease may be caused by the apparition of stable ECMs, from F =2.5%.

3.5.2 Numerical confirmation

We try to reproduce that behavior with the filtered model of PCF. We keep $\tau_R = 50$. To simulate the new laser and in particular to match the observation of the relaxation oscillation frequency, we set $T = 1200$ and $\tau_p = 1.4$ ps, $P = 0.95$. We also choose $\alpha = 3$. We add a gaussian noise with a standard deviation of 10^{-12} to the intensity of the output field before the calculation of the next step of the simulation. The goal is to avoid that the PCF laser dwells on infrequent stable states.

We show in Fig. 3.16 the simulated chaos bandwidth (a) and spectral

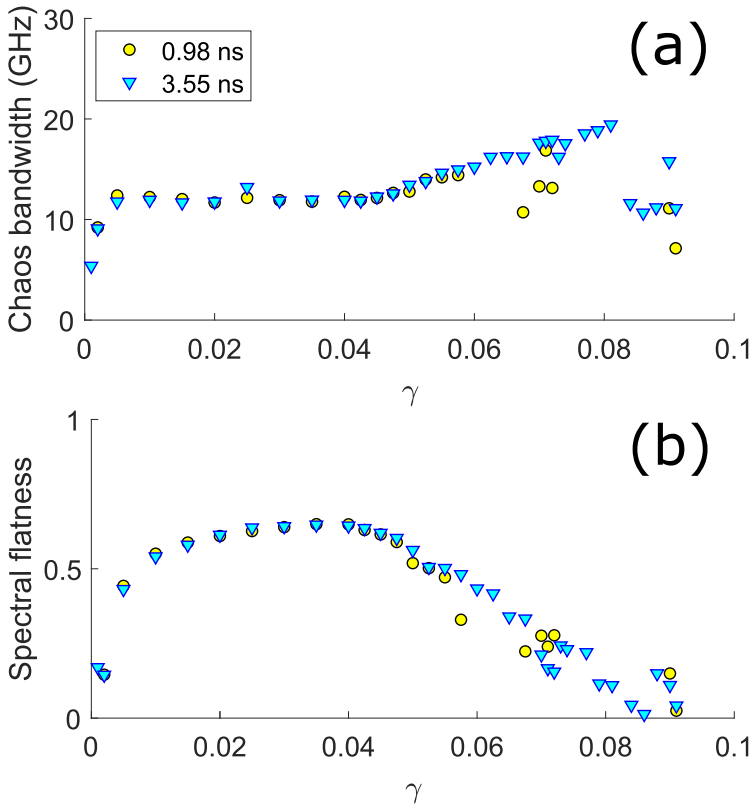

Figure 3.16: Numerical evolution of (a) the chaos bandwidth and (b) the spectral flatness. The pump current I is set at 80 mA. Simulations have been performed with two values of delay: 3.55 ns (yellow circles) and 0.98 ns (blue downward-pointing triangles). Figure taken from [103].

flatness (b) versus the feedback strength γ. For the sake of clarity, the self-pulsing dynamics and steady-states are not displayed.

Figure 3.16 shows a qualitatively similar conclusion than the one we observed experimentally in Fig. 3.15: the evolution of the chaos bandwidth and of the spectral flatness are rather insensitive to delay, except at some values of γ (for instance at $\gamma \approx 0.07$). The greater variability of the indicators can be linked to the presence of the ECMs in that region. For instance at $\gamma = 0.07$, the laser simulated with a 0.98 ns delay (yellow circles) encounters an ECM state. Then, the next simulated time trace, at $\gamma = 0.071$ shows a rather low chaos bandwidth and its spectral flatness is not equal to the one at 3.55 ns delay (blue triangles).

The drop of spectral flatness from $\gamma = 0.04$ confirms the one observed in experiment from $F = 3.5\%$. The drop is however more significant in simulations. In that region where both ECMs and chaos are found, the spectrum of the chaotic states is centered on the frequency of the neighbor ECMs (see Fig. 3.13 (b) and (c)) while the experimental spectra show a broad distribution of the energy among the different frequency components (see Fig. 3.4 or 3.5). Moreover, noisy time series can arbitrarily increase the minimum value of spectral flatness and in experiment much noise was added by the electronic measurement setup. Noise was added in the algorithm to avoid dwelling on unusual states and does not simulate the actual noise added by the measurement setup.

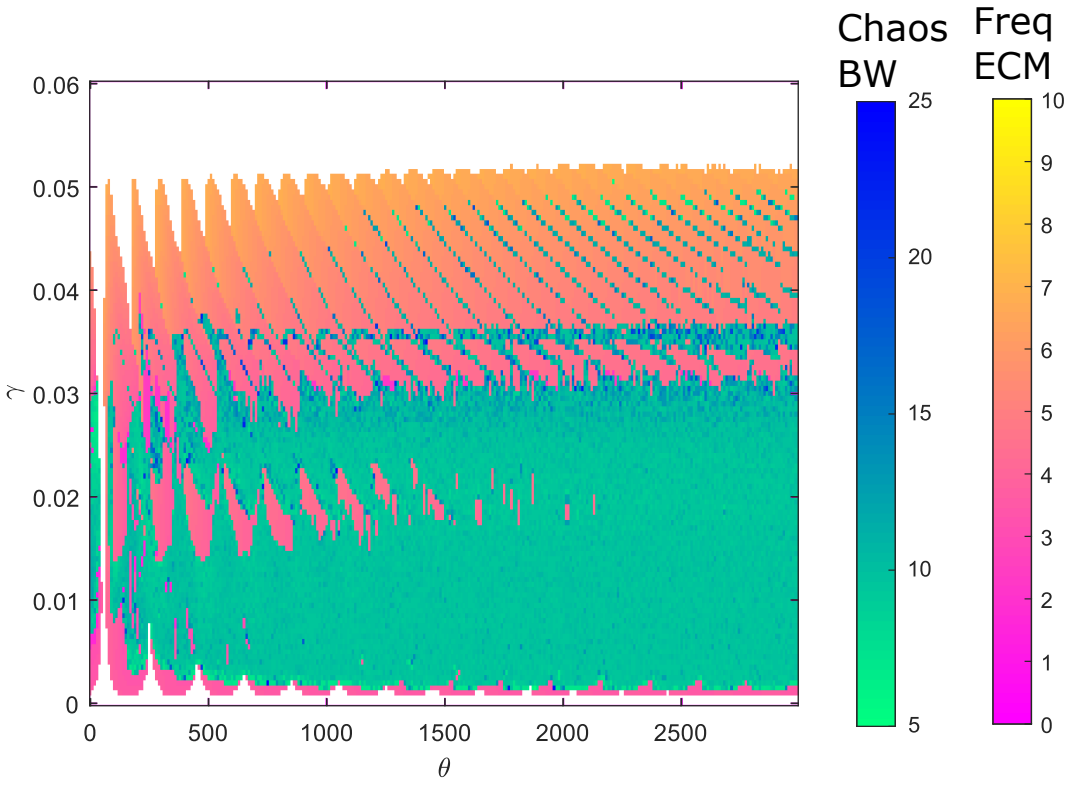

Figure 3.17: Mapping in the plane (γ, θ) of the frequency of the self-pulsing modes (magenta to yellow scale, in GHz) and of the chaos bandwidth of the chaotic states (green to blue scale, in GHz), for a laser diode with PCF.

We then calculated a map of the evolution of the chaos bandwidth versus

both the delay (θ) and the feedback strength γ. We use the following parameters: $\tau_p = 1.4\ ps$, $\alpha = 2$, $P = 0.6016$, $T = 1200$ and $\tau_r = 50$. The corresponding map of the frequency of the self-pulsing modes and of the chaos bandwidth, with respect to θ and γ, is presented in Fig. 3.17. The chaos bandwidth is found to be rather insensitive to delay, as are the ECM frequencies. However, between the ECMs, typically for $0.03 < \gamma < 0.05$, the position of the chaotic states varies and the achieved chaos bandwidth may change with the delay. That result extends the findings from Fig. 3.16 (a).

The map of Fig. 3.17 also enables us to study the case of short feedback, that could not be experimentally studied with our setup. When $f_{EC} \approx f_{RO}$, i.e. when $\theta \approx 200$, the chaos bandwidth and the frequency of ECMs are not different from those measured at other values of delay. For some values of short delays, restabilization may occur at lower values of γ, such as 0.037 at $\theta = 180$, in contrast to the typical restabilization at $\gamma = 0.05$ for longer values of delay. Last, the laser is nearly always stable for all values of γ at $\theta \approx 65$. That value of θ corresponds to a very short external cavity, with a distance of 1.4 cm between the laser and the PCM. Such small θ could be achieved experimentally by placing the PCM in front of the laser diode output but not leaving enough space for inserting a beamsplitter and for therefore measuring simultaneously the PCM reflectivity.

3.6 Influence of the pump current on the chaos bandwidth and the spectral flatness

3.6.1 Experimental observations

We now study the properties of the chaos when varying the pump current. An increase in the pump current increases f_{RO} and we demonstrate in chapter 5 that it also increases the frequencies of the ECMs. The role of this part is to study whether it also enhances chaos bandwidth and spectral flatness. We use the 36 GHz acquisition setup and the delay here equals 3.55 ns.

The evolution of chaos bandwidth and spectral flatness when varying the

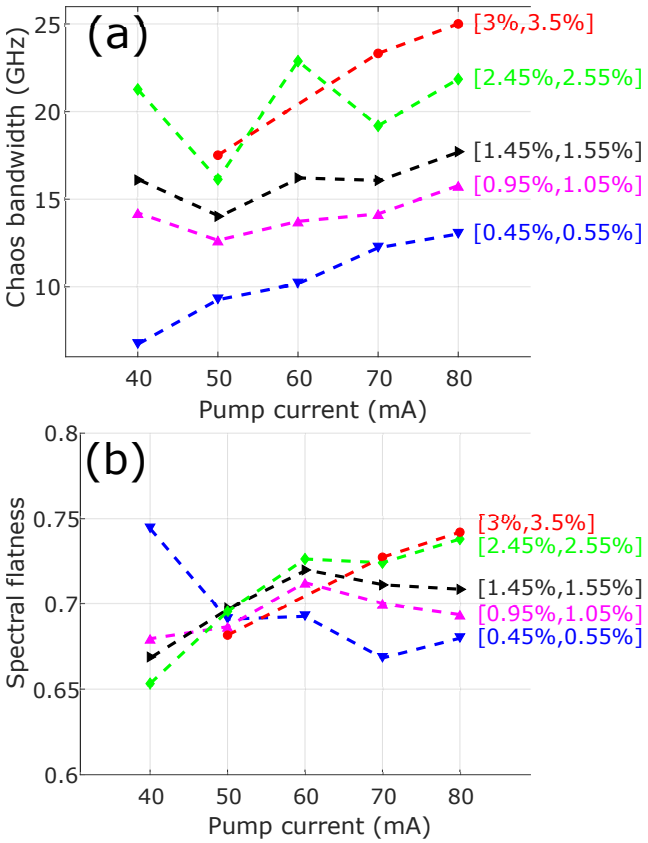

Figure 3.18: Measured evolution of (a) the chaos bandwidth and (b) the spectral flatness versus the pump current, for feedback strength in 5 various intervals, [0.45,0.55%] (blue diamonds), [0.95%,1.05%] (magenta diamonds), [1.45%,1.55%] (black diamonds), [2.45%,2.55%] (green diamonds) and [3%,3.5%] (red diamonds). The delay is equal to 3.55 ns. Figure taken from [103].

pump current from 40 mA to 80 mA is displayed in Fig. 3.18. We trace the averaged value of (a) the chaos bandwidth and (b) the spectral flatness for all the time series whose feedback strengths F are in the following ranges: 0.45 to 0.55% (blue diamonds), 0.95 to 1.05% (magenta diamonds), 1.45 to 1.55% (black diamonds), 2.45 to 2.55% (green diamonds) and 3 to 3.5% (red diamonds), versus the pump current.

We expected that the pump current enhances the chaos bandwidth, as an higher f_{RO} increases the general frequencies. We can confirm that from Fig.

3.18 (a), but there are some exceptions. For instance, with a pump current of 40 mA, the average chaos bandwidth equals 22 GHz for $F \in [2.45\%, 2.55\%]$. At that particular value of feedback strength, the increase of the chaos bandwidth is not linear. An explanation is that mixed dynamics with both ECMs and chaos, as described in section 3.2.2, reduces the chaos bandwidth. Small divergences with the general trend were also observed in COF, where an increase of the current from 25 mA to 30 mA decreases the chaos bandwidth of ≈ 0.5 GHz at very high reflectivity [56].

There is no clear trend in the evolution of the spectral flatness. At a pump current equal to 40 mA, increasing the feedback strength decreases the spectral flatness. On the contrary, at 80 mA, an increase in the feedback strength increases the spectral flatness. The high spectral flatness measured at low feedback strength under a pump current of $40mA$ is surely created by a measurement artefact: the variations of the laser output power are smaller and are concealed in the noise. Hence, the measurement spectral is flatter, but the actual original spectrum of the laser is not.

3.6.2 Numerical study

We simulate the evolution of the chaos bandwidth and of the spectral flatness versus the current I for the following values of feedback strength: $\gamma = 0.1$, $\gamma = 0.06$, $\gamma = 0.04$, $\gamma = 0.06$, $\gamma = 0.08$. We keep the parameters of section 3.5.2: $\tau_p = 1.4\ ps$, $\alpha = 2$, $T = 1200$ and $\tau_r = 50$. However, the value of the normalized pump parameter P varies with the pump current. Since P is proportional to the pump parameter above threshold, we set:

$$P = 0.2\frac{I - I_{th}}{I_{th}} \tag{3.4}$$

The resulting values of chaos bandwidth and spectral flatness are shown in Fig. 3.19. To capture the main features, we averaged chaos bandwidth and spectral flatness from ten simulations with random initialization. The observations from the experiment of Fig. 3.18 are confirmed by the simulation: the chaos bandwidth increases with the pump current. In particular, the increase of the chaos bandwidth with the pump is stronger when γ is higher. This was also

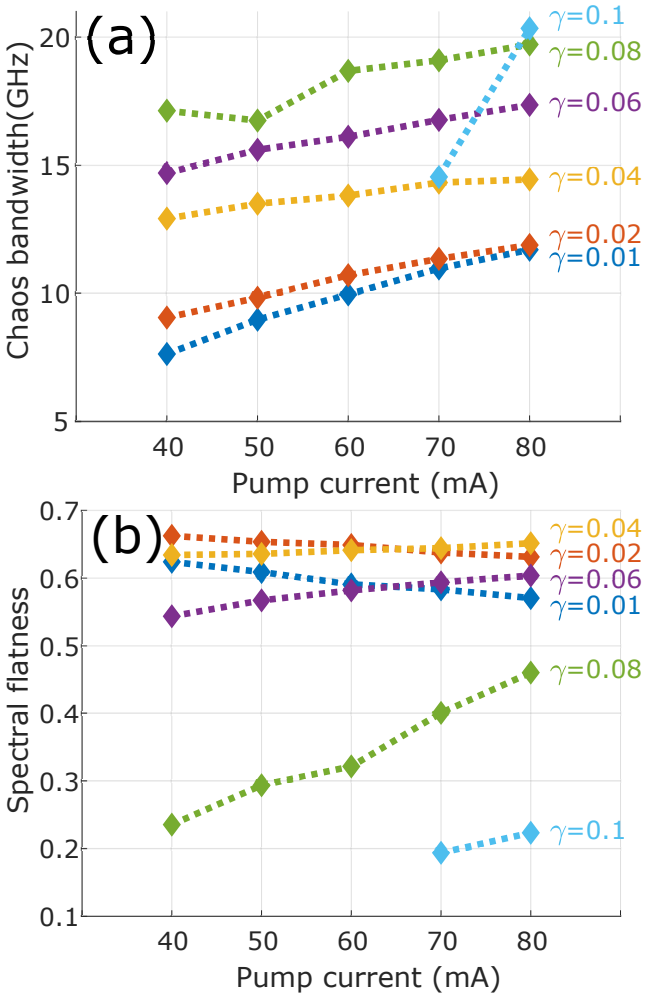

Figure 3.19: Simulated evolution of (a) the chaos bandwidth and (b) the spectral flatness, versus the pump current I, for five values of feedback strength γ. The delay is equal to 3.55 ns. Figure taken from [103].

observed in Fig. 3.18 for feedback strength between 3% and 3.5%. We find that the spectral flatness is rather independent from the change of pump current, and, for low feedback strengths, increasing the pump current even slightly decreases the spectral flatness. This confirms our experimental findings. The value of γ associated with the onset of ECMs decreases with the pump current [67]. Hence the drop of spectral flatness described in section 3.6.1 occurs at a lower value of γ as the pump current decreases. That explains why the

spectral flatness strongly increases with the pump current for $\gamma > 0.06$.

3.7 Conclusion

We have presented one of the results of this thesis, the analysis of the evolution of the chaos bandwidth and spectral flatness of the laser output power. The chaos bandwidth is defined as the span of frequencies where 80% of the total energy is located while spectral flatness indicates whether the energy is concentrated in a few frequencies or over a large range of frequencies.

First, we studied the evolution of the chaos bandwidth with the feedback strength. We experimentally find a fast increase of the chaos bandwidth at low feedback strength values, followed by a slighter increase of the chaos bandwidth at higher values of feedback strength. Using numerical simulations, we highlighted that the finite depth penetration in the phase-conjugate mirror can be responsible of this saturation of the chaos bandwidth. Then, we also observed that both the experiment and the numerical simulations show a link between the high values of chaos bandwidth obtained with PCF and the external cavity modes obtained at high values of feedback strength. The spectral flatness has a behavior similar to the chaos bandwidth: after a fast increase at low values of feedback strength, it saturates and even slightly decreases for larger feedback strengths.

Second, we observed that changing the length of the cavity does not significantly modify the chaos bandwidth and the spectral flatness. Last, we studied the influence of the pump current. An increase in the pump current leads to higher values of chaos bandwidth but the spectral flatness remains in the same range of values.

Chapter 4

Permutation entropy in phase-conjugate feedback

In the previous chapter, we studied the chaos generated by phase-conjugate feedback (PCF), using the chaos bandwidth and the spectral flatness. We observed that PCF was able to generate broadband chaos, with a quite flat spectrum, in a large range of parameters.

Another performance of the chaos is here analyzed: the permutation entropy (PE). PE studies the repetition of patterns in time series and enables to quantify its predictability. It can easily be applied to quantify the complexity of deterministic chaos. Therefore, we use that method to further explore the richness of the chaos from PCF in laser diodes.

The calculation of the permutation entropy from the experimental and numerical data were performed. Our results were published in Refs. [102, 103, 126].

4.1 Permutation entropy

4.1.1 General definition

Permutation entropy was proposed in 2002 by Bandt and Pompe [127]. Its calculation is based on the repetition of short patterns when the time series is

re-sampled at a given value. For a given time series, we take a delay t_D and a subset length D. The time series is also characterized by its sampling time t_S and its length $t_{tot} = N \times t_S$, N being the number of points in the time series.

We consider all the possible vectors of D points separated by a time of t_D. Hence we obtain subsets of D points, $[I(1)...I(D)]$. Since the time series are numerical measures, it is very rare to have two equal values. Therefore, we sort $[I(1)...I(D)]$ in strictly increasing order $I(r_1)...I(r_D)]$, where $r_1,...,r_D$ are indices chosen to sort the vectors. The vector $[r_1...r_D]$ can be represented by a permutation. We then compare the permutation associated with the vector $[r_1...r_D]$ and the $D!$ possible permutation, of order D.

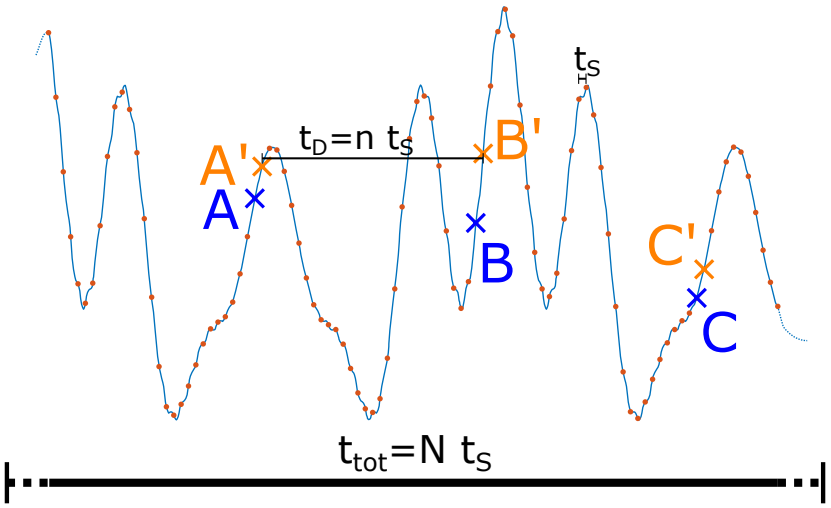

Figure 4.1: Principle of the subsets of permutation entropy. t_S is the sampling time, t_{tot} the total length of time trace and t_D the permutation entropy delay. The vectors of $D = 3$ points, with a distance between two points of $t_D = 30 \times t_S$ are considered, for instance [A B C] and [A' B' C'].

An example of the association of permutations within the time trace is presented in Fig. 4.1, with $D = 3$. The time trace, in blue, is sampled at a period t_S (red points). Then, D points separated by the distance t_D are considered. We take for instance the vectors [A B C] and [A' B' C']. We have A>B>C and the permutation (1,2,3) is associated with the subset [A B C]. We also have B'>A'>C' and associate to it the permutation (2,1,3). All the $N - (D-1) \times n$ vectors of D points separated by t_D are considered for the calculation of PE.

We note π_i, $i = 1...D!$, the possible permutations and the distribution $p(\pi_i)$ of each permutation is defined as:

$$p(\pi_i) = \frac{\#\{k|k \leq N-D, [I(k+1)...I(k+D)] \text{ is associated with } \pi_i\}}{N-D+1} \tag{4.1}$$

If the system is predictable, only a few patterns will repeat and there will be a pattern more present than the others. The permutation entropy at a delay t_D is therefore defined as:

$$\rho(t_D) = -\sum_{i=1}^{N} p(\pi_i) \log p(\pi_i) \tag{4.2}$$

That definition is related to the Shannon entropy [128].

$\rho(t_D)$ is often normalized $\frac{1}{\log D!}$ [129, 130] and we will use that convention here. Therefore, $\rho(t_D)$ is always between 0 and 1. 0 correspond to the complete predictability and 1 to complete predictability. The condition $N \gg D!$ is necessary to have an accurate measurement of PE [129]. To keep relatively short calculation time, one typically choose $3 \leq D \leq 7$ [130].

4.1.2 Applications

Permutation entropy has been used in numerous field of study.

In medicine [131], it was used to analyze electroencephalograms (EEGs). Permutation entropy of EEGs can indicate epilepsy [132] or make the difference between consciousness and unconsciousness during an anesthesia [133]. Permutation entropy can determine the physiological and pathological condition of a patient from its heart rate variability [134].

In economics, permutation entropy is able to underline the period of time in the evolution of the prices of some American commodities [135]. Permutation entropy was also used to study the degree of stock market inefficiency, i.e. the difference between the trade price of goods and their real value [136].

In environment studies, Bandt applied in 2005 permutation entropy to textbook time series: the evolution of the population of the Canadian Lynx between 1821 and 1934, the southern oscillation index from 1950 to 1987, i.e. the monthly evolution of the temperature of the Pacific Ocean and the

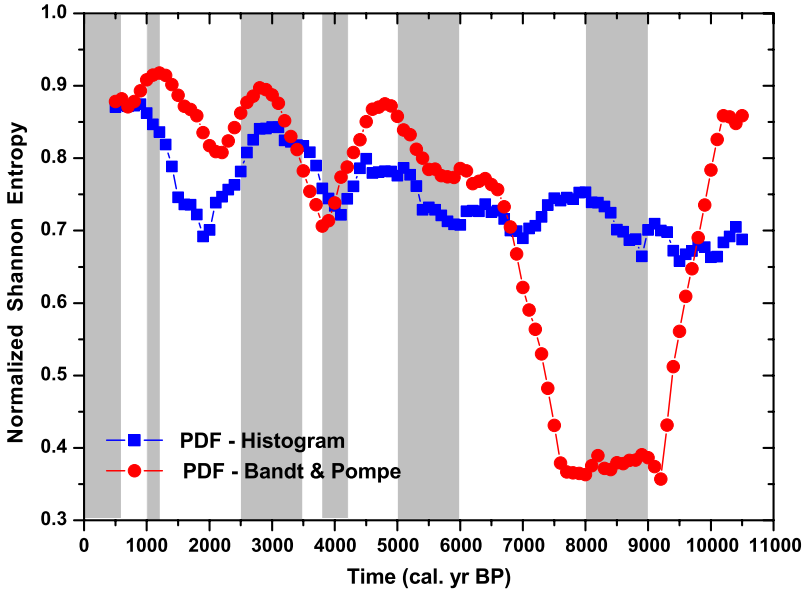

Figure 4.2: Example of permutation entropy used in climate studies. Permutation entropy (red) and the entropy obtained from histograms (blue) of the temperature of the Ocean during the Holocene, versus time. The authors use a sliding time window of 1000 data values and a lag of 100 data values between successive windows. The grey bands correspond to the major periods of Holocene rapid climate change (RCC). Figure taken from Ref. [137].

associated El Niño phenomenon, and the monthly estimated fish recruitment from 1950 to 1987. It was used to underline the hidden predictability in these systems [138]. Permutation entropy can also enable a study of the evolution of the southern oscillation index of the Holocene, in particular during rapid climate changes (RCC). It is presented in Fig. 4.2. The authors use a gliding permutation entropy at delay $t_D = t_S$ to determine the presence of RCCs, indicated in grey. Using the permutation entropy on 1000 consecutive points (in red) is found to enhance the distinction of RCC phenoma when compared to Shannon entropy obtained from histograms (in blue) [137].

In all these applications, the number of points in the experimental time series varies from about hundreds to tens of thousands [130].

Permutation entropy was also applied to numerical simulations, such as the Lorenz equations [139] or logistic maps [138, 139]. And it was logically

extended to the laser diode dynamics, and in particular chaotic dynamics.

4.1.3 Previous results about laser diode chaos

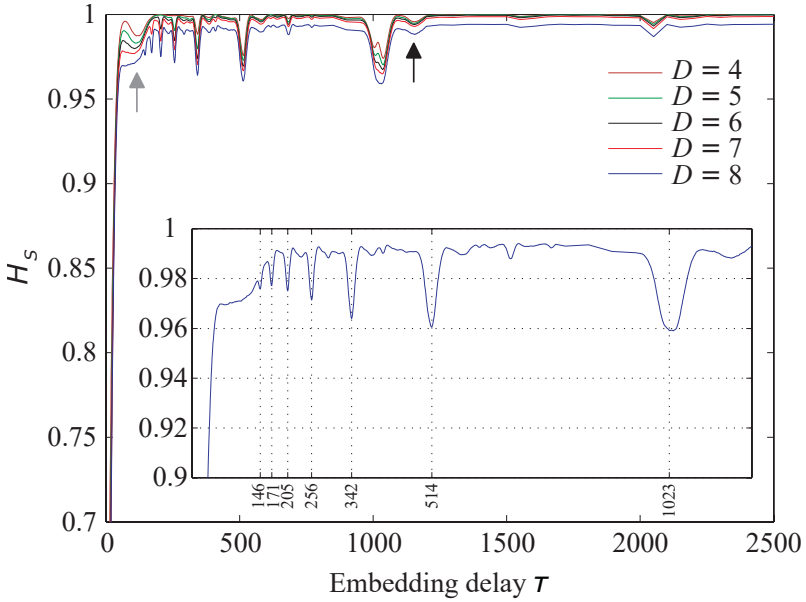

Figure 4.3: Experimental permutation entropy of the output intensity of a laser with COF, as a function of the embedding delay τ ($= t_D$) with embedding dimensions D between 4 and 8. The grey arrow indicates the peak at τ_{RO} and the black one the peak at $\tau_{EC} + \tau_{RO}/2$. The inset displays the detail of the locations of the peak at τ_{EC} and its sub-harmonics for $D = 8$. Figure taken from Ref. [140].

In 2011, Soriano *et al.* analysed the permutation entropy of a laser with conventional optical feedback (COF), with data obtained from the Lang-Kobayshi equations or from experiment. They described that permutation entropy highlights the time scales of the laser, i.e. the relaxation oscillation frequency τ_{RO} and the time delay of the external cavity τ_{EC}, as it can be shown in Fig. 4.3. They varied the delay of the permutation entropy t_D from t_S to $2500t_S$. They observed peaks at τ_{EC} and its $(D-2)$ subharmonics (i.e. $\tau_{EC}/i, i = 1..(D-1)$), a peak at τ_{RO} and also a peak at $\tau_{EC} + \tau_{RO}/2$. Increasing D increases the depth of the peaks [140].

In the applications of chaotic delayed lasers, identifying the time-delay enables the reconstruction of the signal and hence lowers the security of chaos-based cryptography [141]. The consequence of the observation of a drop in permutation entropy around τ_{EC} was that permutation entropy around τ_{EC} should be maximized to avoid a signature of the time delay. It was therefore compared to the so-called "time-delay signature" (TDS), i.e. the peak in the autocorrelation function of the time series [125, 141].

Permutation entropy was also applied to simulated laser with COF with the addition of a low amplitude digital signal [142], to VCSELs with variable polarization feedback [143], to mutual delay-coupled lasers (in that case the time delay is the distance between the two lasers) [144] and to laser diodes under stimulated Brillouin scattering optical feedback [145]. Permutation entropy was also used to differentiate stochasticity and noise in the switching of dynamics between two coupled lasers [146], in a way similar to the low frequency fluctuations of lasers with feedback [147].

4.2 Permutation entropy versus feedback strength

4.2.1 Preliminary results

We now apply the PE calculation to three time series generated by our PCF system. The laser diode is the SDL-5410 laser diode (cf. section 2.2.2.1), pumped at 80 mA. The relaxation oscillation frequency is 4.8 GHz, i.e. a period of 208 ps. The external cavity length τ is 0.98 ns. The time series are sampled at 12.5 ps, so the relaxations oscillations correspond to an embedding delay τ_{RO} =17 and the external cavity to an embedding delay τ =78. The time series are 80000-points long. The feedback strength F is equal to 1.6%, 4.0% and 4.4%. These time series are the three time series presented in Fig. 3.5.

We show in Fig. 4.4 the permutation entropy versus the embedding delay of these three times series. When F =1.6% (dotted red line), a strong peak appears at $\tau_{RO}/3$ and a smaller peak at τ. That confirms results findings of Chapter

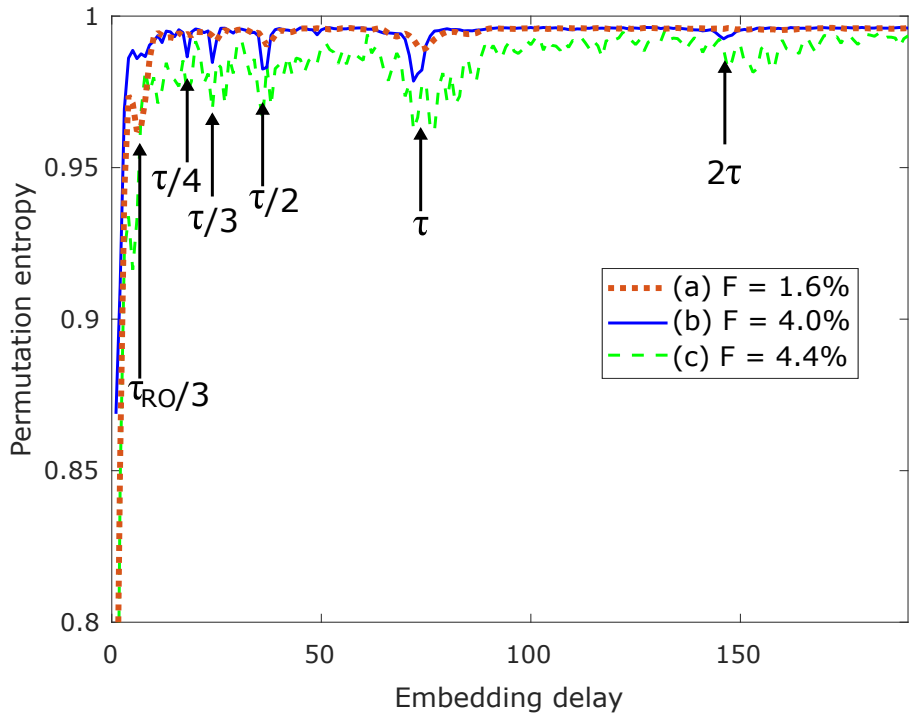

Figure 4.4: Evolution of the permutation entropy as a function of embedding delay for the three time traces obtained at feedback strengths of 1.6% (green dashed line), 4.0% (red dotted line) and 4.4% (green dashed line). The multiples or sub-multiples of the external cavity delay are indicated with arrows. The time delay is 0.98 ns. Embedding delay is expressed in multiples of the sample time (12.5 ps) and is here the external cavity round-trip time. Figure taken from Ref. [103].

3: at low feedback strength, the dynamics is driven by destabilized relaxation oscillations. When F =4.0% (solid blue line), the signature at τ is much stronger and the signature at $\tau_{RO}/3$ is less important. The main time signature of the system is τ. Last, when F =4.4% (dashed green line), the permutation entropy is low at multiples and submultiples of τ. Further studies of that time series [103] show that it exhibits intermittency and switchings between self-pulsed external cavity mode and chaos. The presence of an external cavity mode strongly increases the signature of τ. We also observe that the permutation entropy is lower for that time series at all values of embedding delay. Consequently, this intermittency creates recurrent patterns at various frequencies.

4.2.2 Main results

Next, we study a set of time series from section 3.2.2. The laser is the SDL-5420 laser, pumped at 80 mA (f_{RO} = 5.2 GHz). The time series are still sampled at 12.5 ps. The cavity is 1.545 m long, so the round-trip time corresponds to τ_{RT} =824. Each time series has 36404 points and we choose D=7.

The peak at τ_{RT} is the deepest signature of the permutation entropy. Therefore, we study the evolution of the permutation entropy at τ_{RT}, with respect to the feedback strength.

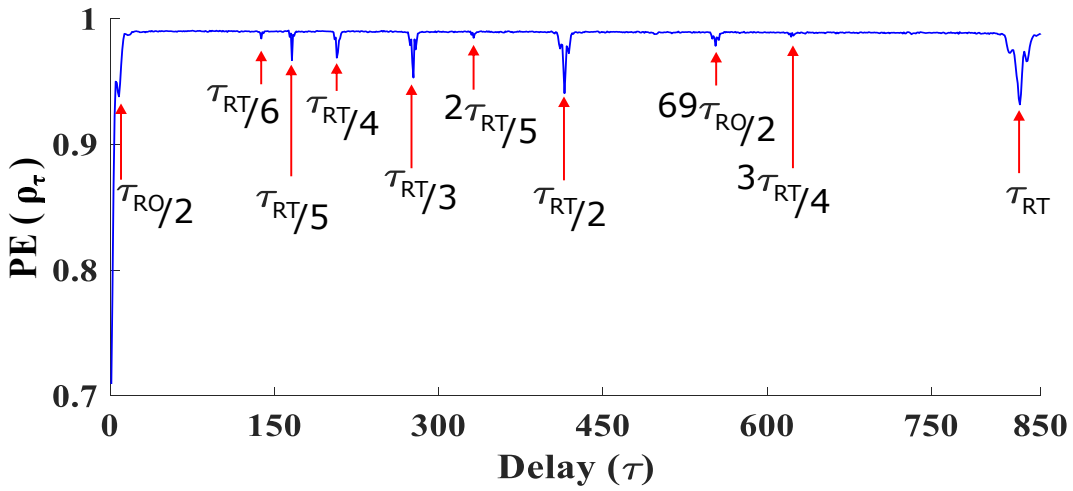

Figure 4.5: Evolution of the permutation entropy versus the embedding delay. The time delay is 10.3 ns and the feedback strength is 1.23%. Figure also presented in Ref. [102].

We present in Fig. 4.5 the evolution of the permutation entropy versus the embedding delay. For that particular time series the feedback strength is 1.23%. If we compare with Fig. 4.4, the longer delay in Fig. 4.5 enables a closer look to the peaks at sub-multiples of τ_{RT}. Peaks are present at τ_{RT}, $3\tau_{RT}/4$, $\tau_{RT}/2$, $2\tau_{RT}/5$, $\tau_{RT}/3$, $\tau_{RT}/4$, $\tau_{RT}/5$, $\tau_{RT}/6$, and also at $\tau_{RO}/2$ and $69\tau_{RO}/2$.

Then, we show in Fig. 4.6 the evolution of the permutation entropy at τ_{RT} (or ρ_{RT}), coupled with the evolution of the chaos bandwidth The permutation entropy is high, superior to 0.85. The only exceptions are with external cavity modes, indicated with black dots in Fig. 4.6 or similar states. It is reasonable that dynamics oscillating at a submultiple of τ_{RT} have a low permutation

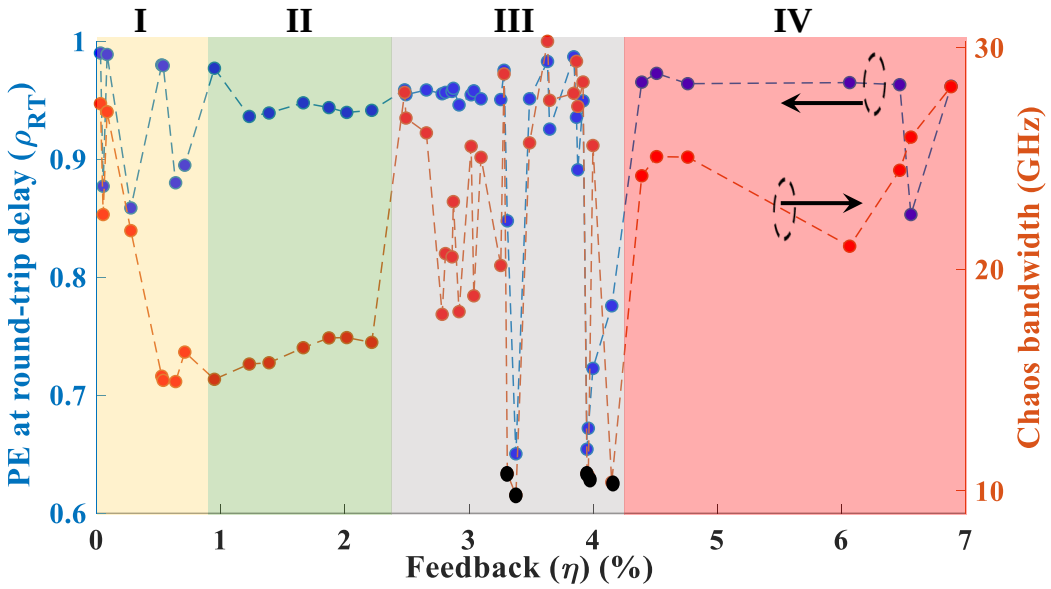

Figure 4.6: Dynamics of a PCF system in the context of PE at roundtrip delay (primary vertical axis) and chaos BW (secondary vertical axis) as a function of feedback. Region I (yellow): relaxation oscillation buildup; II (green): low-feedback; III (grey): transition window towards external cavity modes (ECM) with black dots representing pulsed output; IV (red): high-feedback with ECM. Black dots represent pulsing states. Figure taken from [102].

entropy at τ_{RT}. However, for $\eta \in [1, 3.3]\%$ (regions I and II) and $\eta \in [4.4, 6.5]\%$ (region IV), $\rho_{RT} > 0.93$, the laser output is highly complex with extremely low predictability.

With COF, the experimental permutation entropy was limited to 0.75 (for $D = 7$ and τ_{RT} =4.5 ns) [148]. Therefore PCF demonstrates a much better permutation entropy and complexity.

Reference [64], from our group, predicted high values of permutation entropy, up to 0.986 (for $D = 7$ and τ_{RT} =1 ns), and our experimental results therefore confirm that prediction. We predicted a monotonic increase of the permutation entropy, and then a plateau and a slight decrease with the increase of the feedback strength. The theoretical study also predicted higher permutation entropy for PCF than for COF, which we here confirm.

4.2.3 Inversion of the permutation entropy at harmonics of τ_{RT}

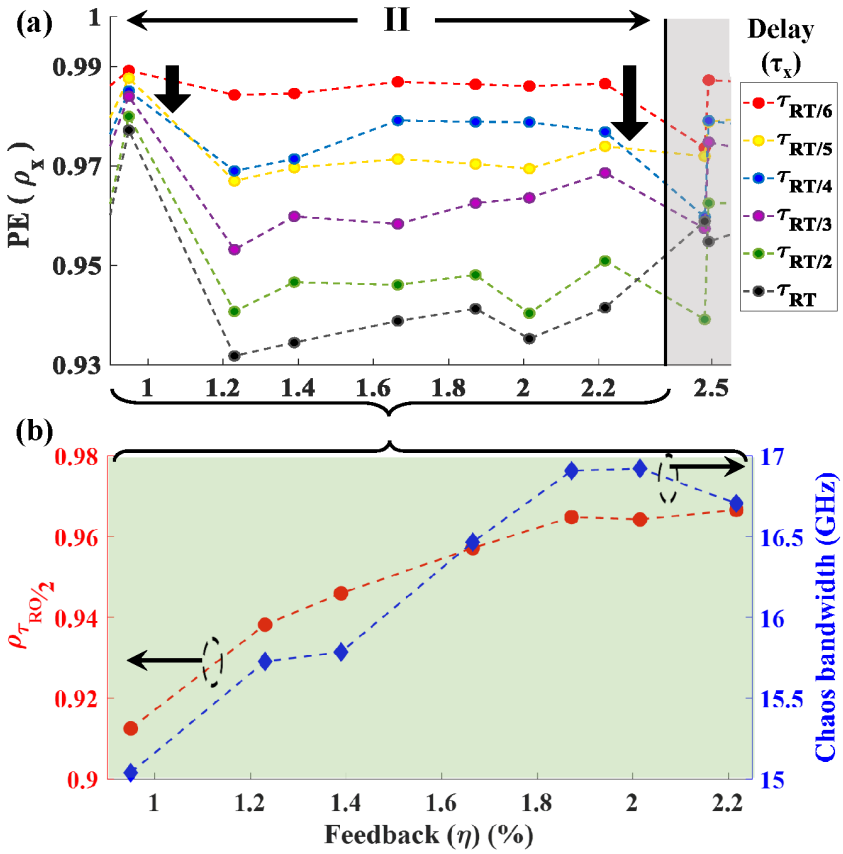

Figure 4.7: Permutation as a function of feedback (a) for embedding delays equal to τ_{RT} and subharmonics of τ_{RT} and (b) for embedding delay equal to $\tau_{RO}/2$. The black arrows in (a) indicate an inversion of $\tau_{RT}/4$ and $\tau_{RT}/5$. The secondary vertical axis and the blue curve in (b) gives the chaos bandwidth.

We have studied the evolution of the permutation entropy at τ_{RT}. However, Fig. 4.5 shows that the peak at $\tau_{RO}/2$ is deeper than the one at τ_{RT} and that submultiples of τ_{RT} may highlight peculiar dynamics. Therefore, we now study the evolution of the permutation entropy at $\tau_{RT}/6$, $\tau_{RT}/5$, $\tau_{RT}/4$, $\tau_{RT}/3$, $\tau_{RT}/2$, τ_{RT}, $2\tau_{RT}/5$ and $\tau_{RO}/2$ versus the feedback strength.

Figure 4.7 (a) shows the evolution of the permutation entropy at these various embedding delays as a function of feedback, for $\eta \in [0.9\ 2.2]\%$. The

PE value, i.e. the predictability of the time series, increases with the delay corresponding to the sub-harmonic multiple of τ_{RT}. However, we observe an exception at $\tau_{RT}/4$: the PE values at $\tau_{RT}/4$ are higher than at $\tau_{RT}/5$ and lower than at $\tau_{RT}/6$. That inversion occurs between the two black arrows in Fig. 4.7 (a). Outside of that region of values of feedback strength, we observe $PE(\tau_{RT}/4) < PE(\tau_{RT}/5) < PE(\tau_{RT}/6)$. That inversion is masked if we only study $PE(\tau_{RT})$.

4.2.4 Evolution of the permutation entropy at $\tau_{RO}/2$

Figure 4.7 (b) shows the PE values at $\tau_{RO}/2$ at increasing feedback strength and compares it with the chaos bandwidth. In the presented region, both have a similar continuous increase. In the region $\eta \in [1.22.2]$, the permutation entropy at τ_{RT} is constant versus the feedback strength. Therefore we conclude that two phenomena occur simultaneously: the onset of high chaos bandwidth and the decrease of the signature of the ROs in the laser dynamics, without variations of the signature of PE at τ_{RT} time-scale.

4.3 Evolution of permutation entropy versus delay

In section 3.5, we studied the evolution of the chaos bandwidth and the spectral flatness for two different values of delay. We have concluded that the delay has no influence on the chaos bandwidth and spectral flatness of the laser output. We extend that study to permutation entropy.

4.3.1 Experimental observations

We use the same time series as in section 3.5.1. The experimental setup is given in Fig. 4.8. The 850 nm edge-emitting laser is the SDL-5420 model. Its output light is reshaped by the collimator and focused into the phase-conjugate mirror (PCM). The beam splitter (BS) enables the acquisition of the feedback strength trough a powermeter (PM) and of the laser output power is recorded

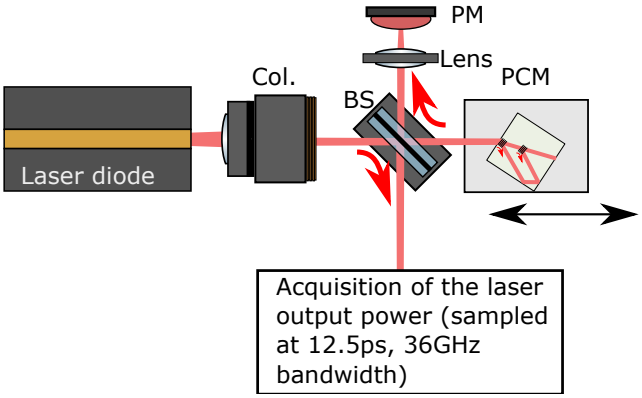

Figure 4.8: The experimental setup used in that section, and its components. The support of the phase-conjugate mirror (PCM), represented in light green, is as close as possible to the mount of the beam splitter (BS). In the illustration, the single-trip distance between the output of the EEL (edge-emitting laser) and the PCM is 14.7 cm.

at a sampling rate of 12.5 ps. All the details about this equipment have been given in section 2.2. Two values of delay have been chosen: 3.55 ns and 0.98 ns, corresponding to f_{EC}=282 MHz and f_{EC}=1.02 GHz and the distance between the laser output facet and the mirror equals 53.2 cm and 14.7 cm. This latter configuration is the shortest cavity length we can apply.

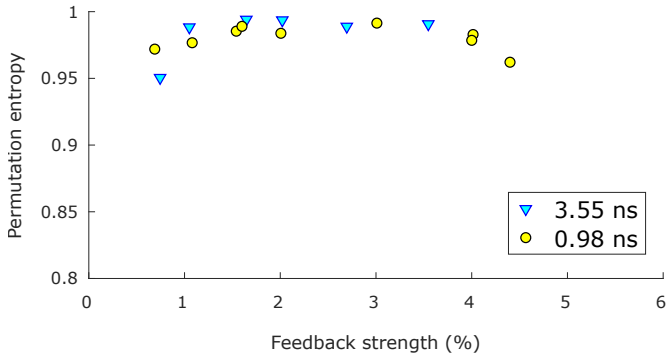

Figure 4.9: Evolution of the permutation entropy at time delay. The pump current is set at 80 mA. Experiments have been performed with two values of delay: 3.55 ns (blue triangles) and 0.98 ns (yellow circles). Figure taken from Ref. [103].

To obtain the time series, we use as in section 3.3.1 the slow natural

variations of the feedback strength while we record 1 μs long time series. Hence we obtain a set of time series at various values of feedback strength. Then, for both values of delay, we randomly select 6 to 9 time series at different times to obtain a rough study of the permutation entropy at delay. The results are presented in Fig. 4.9. In the range of feedback strength from 0.9% to 2%, the permutation entropy at time delay increases similarly for both values of time delays. From 2% to 3.5%, it reaches a plateau at high values of feedback strength (>0.98). The maximum value is 0.994. Then, for values of feedback strength superior to 3.5%, the permutation entropy at delay is reduced. That range of feedback strength values correspond to the region of the onset of the ECMs dynamics. In the configuration described in that section, we do not observe chaotic dynamics at higher values of feedback strength. In section 4.2.2 (see Fig. 4.6), we observed a decrease of the permutation entropy at delay around the ECMs in region III, followed in region IV by a rise to the high values obtained at medium values of feedback strength. That difference is probably caused by the longer cavity that was used, with a time delay of 10.3 ns.

4.3.2 Numerical findings

To check the previous conclusions about the permutation entropy at delay, we use the model of the filtered PCF model, introduced in section 1.3.1. Reference [64] proposed a study of the evolution of the permutation entropy at delay in the case of an unfiltered PCF. However, that model considers an instantaneous penetration of the light inside the PCM and the filtered model describes more accurately the dynamics of the PCF with a finite-length nonlinear material (see section 1.3.1).

To compare with the results about chaos bandwidth and spectral flatness, we reuse the 20000-points long time series obtained in chapter 3, section 3.5.2. The parameters are presented in table 4.1

Figure 4.10 shows the simulated evolution of the permutation entropy at two time delays with the chaos bandwidth. Only the chaotic states have been represented in the graph and missing points indicate regular self-pulsing states. For $\gamma \in [00.005]$, the permutation entropy strongly rises. Then, it remains at

Symbol	Description	Value
τ_p	photon lifetime (integration step)	12.5 ps
τ	normalized round-trip time in the external cavity	0.98 or 3.55 ns
T	normalized electron lifetime	1200
γ	dimensionless feedback strength	$\in$ [0 0.1]
α	linewidth enhancement factor	3
P	pump parameter	0.951
R	standard deviation of the Gaussian noise in the intensity of the output field	$1e^{-12}$

Table 4.1: Parameters used in the simulation of sections 4.3.2 and 4.4.2.

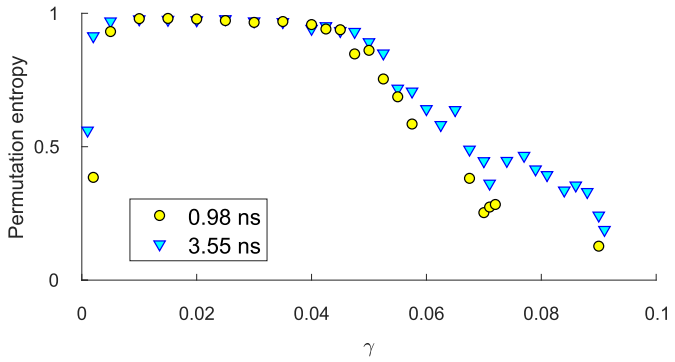

Figure 4.10: Evolution of the permutation entropy with the feedback strength (γ). The simulation has been ruled with two values of delay. Figure taken from Ref. [103].

high values. The maximum value equals 0.987. From $\gamma > 0.05$, the permutation entropy decreases. That behavior is consistent with the experimental results presented in Fig. 4.9. The first stable ECMs appear at $\gamma > 0.05$ and we observe that the apparition of the ECMs decreases the permutation entropy.

4.4 Evolution of permutation entropy versus pump current

Pump current is one of the parameters that is easy to tune in an experimental system. We have concluded that the delay has no influence on the chaos

bandwidth and spectral flatness of the laser output. We extend that study to permutation entropy at delay. In section 3.6, we studied the influence of the pump current on the chaos bandwidth and the spectral flatness. We concluded that an increase in the pump current increased the chaos bandwidth whereas the spectral flatness was less dependent on the pump current. We now extend the analysis of the influence of the pump current to permutation entropy at round-trip delay (designated "permutation entropy" or PE thereafter).

4.4.1 Experimental observations

We reused the experimental setup of 4.3.1. The distance between the laser and the mirror is set at 53.2 cm, so the time delay equals 3.55 ns.

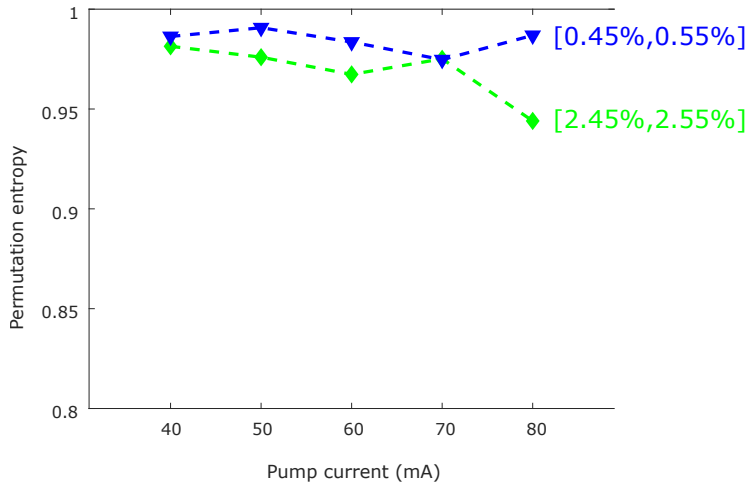

Figure 4.11: Measured evolution of the PE versus the pump current, for feedback strength in two intervals, [0.45%, 0.55%] (blue diamonds) and [2.45%, 2.55%]. The delay is equal to 3.55 ns. Figure taken from Ref. [103].

Figure 4.11 shows the evolution of permutation entropy when varying the pump current from 40 mA to 80 mA, for feedback strength in the ranges 0.45% to 0.55% and 2.45% to 2.55%. The PE reaches high values for all pump currents. The PE is slightly higher at smaller feedback strengths but it does not decrease when varying the pump current. We can conclude that the complexity is rather independent of the pump current. However, changing the pump current induces

an increase of the chaos bandwidth (see section 3.6) and that increase will therefore not induce a reduction of chaos complexity.

4.4.2 Numerical findings

We want to confirm these experimental results. Therefore, we perform a new simulation, reusing the equations and the parameters of section 4.3.2 (see table 4.1), that were also used in the numerical study of the influence of the pump on the chaos bandwidth (section 3.6.2 of chapter 3). In particular, we set:

$$P = 0.2\frac{I - I_{th}}{I_{th}} \tag{4.3}$$

where I_{th} =13.9 mA is the threshold current of the laser.

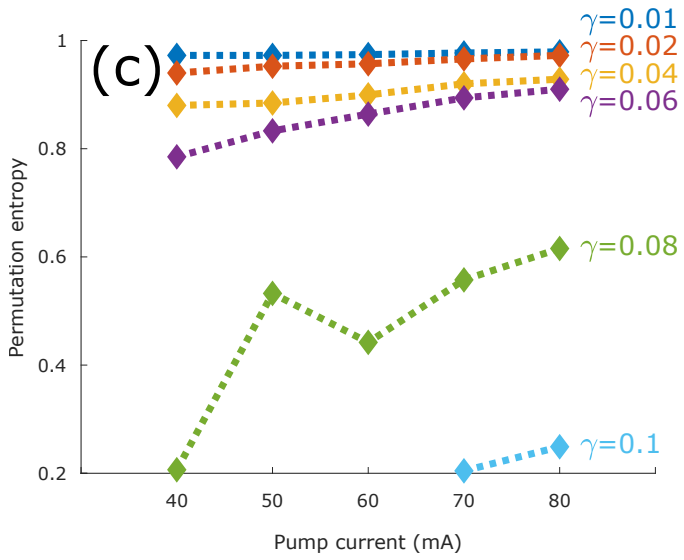

Figure 4.12: Simulated evolution of the permutation entropy versus the pump current, for five values of feedback strength (γ). The delay is equal to 3.55 ns. Figure taken from Ref. [103].

Figure 4.12 shows the permutation entropy for pump current I$\in$ {40 mA, 50 mA, 60 mA, 70 mA, 80 mA} and for feedback strength $\gamma \in$ {0.01, 0.02, 0.04, 0.06, 0.08, 0.1}. At low values of γ, the pump current has a low influence on the permutation entropy. However, for high values of γ, the permutation entropy

is lower and more sensitive to I. It confirms the results of section 4.3.2: the onset of the ECMs induces a decrease of the permutation entropy. In particular, numerical simulations indicate that the onset of the ECMs occur at lower values of γ for low values of pump current [67] while the permutation entropy at 40 mA is the lowest one, and the decrease is also visible at $\gamma = 0.06$. If the pump current is low, the ECMs will be found at lower values of γ and the decrease of the permutation entropy will also occur at lower values of γ.

4.5 Conclusion

We have studied the permutation entropy of a laser subjected to PCF. The permutation entropy displays the signatures of both the external-cavity delay and the period of the relaxation oscillations (section 4.2.1). The experimental and numerical permutation entropy at external cavity delay of PCF is larger than the one found for chaos from COF, and the permutation entropy keeps a large values in a large range of feedback strength (section 4.2.2). The experimental permutation at the period of the relaxation oscillations increases with the feedback strength (section 4.2.4). The permutation entropy at the external cavity time delay remains high whatever the length of the external cavity or the pump current (sections 4.3.1 and 4.4.1). A filtered PCF model reproduces the experimental findings qualitatively well (sections 4.3.2 and 4.4.2). Both simulation and experiment indicate that the onset of the ECMs is responsible for a decrease in the permutation entropy.

To conclude, PCF is a good way to obtain high complexity with a simple system. The parameters can be tuned to modify the chaos bandwidth while keeping the complexity high, except if the system approached a region of ECMs dynamics.

Chapter 5

External cavity modes

A laser diode with phase-conjugate optical feedback (PCF) is able to generate dynamics completely different from those obtained with a conventional optical feedback (COF). External cavity modes (ECMs), defined as regular self-pulsing modes, are unique to PCF. In this chapter, we study the ECM solutions systematically and demonstrate their dependency on the external cavity (EC) frequency. ECMs show harmonic frequencies of the EC frequency. Still, remarkably, we show that the ECM frequency is independent of the EC length. When varying the EC length, the harmonic order adjusts itself such that the resulting ECM frequency remains constant. We conclude by analyzing the influence of the laser pump current on the frequency of the ECMs.

5.1 Self-pulsing dynamics in lasers with optical feedback

Optical feedback generate self-pulsing dynamics at two different frequencies in a laser diode: 1) the first frequency, called the relaxations oscillations frequency f_{RO}, is related to the sustained regular pulsations, undamped by the feedback [25] and 2) a laser with external optical feedback also bears another frequency, the frequency of the external cavity f_{EC}, defined as the inverse of the feedback time delay τ. In the so-called Ikeda nonlinear optical cavities, self-pulsations

are predicted at $f_{EC}/2$ [149]. Oscillations at f_{EC} can also be obtained in laser diodes from the beating between two external cavity modes [150]. For short delays ($\tau \ll 1/f_{RO}$), the system can reach therefore high frequencies [151]. With longer delays, harmonics of $\frac{2n+1}{2} f_{EC}$ have been reported in nonlinear optical cavities [149, 152] and have been also observed in systems with OF [153, 154]. However, the frequency of these harmonics remains much more lower than f_{RO}. More recently, self-pulsations at frequencies larger than f_{RO} have been reported in polarization rotated OF although with a long f_{EC} [155].

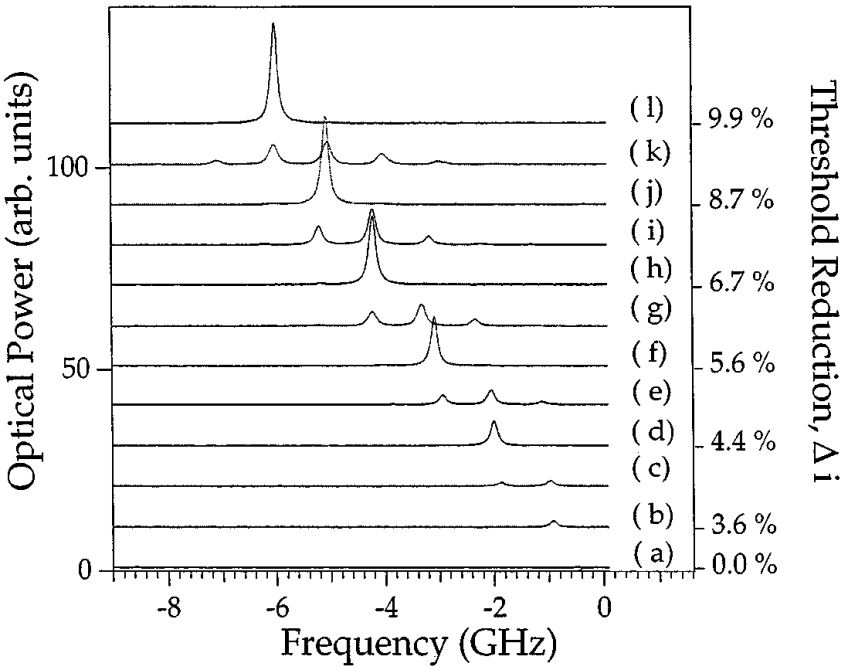

Figure 5.1: Optical spectrum of a laser subjected to COF, showing external cavity modes. The feedback strength is measured using the threshold reduction. Figure taken from Ref. [34].

A new kind of self-pulsations was theoretically predicted in 2003: a laser with phase-conjugate feedback (PCF) [156] could present self-pulsing states [38], where the frequency oscillates at a multiple of $f_{EC} = 1/\tau$. Hence, these solutions were named external cavity modes (ECMs), by analogy with the steady-state external cavity modes of the conventional optical feedback (COF). Figure 5.1 presents the optical spectra of a laser subjected to COF, for increas-

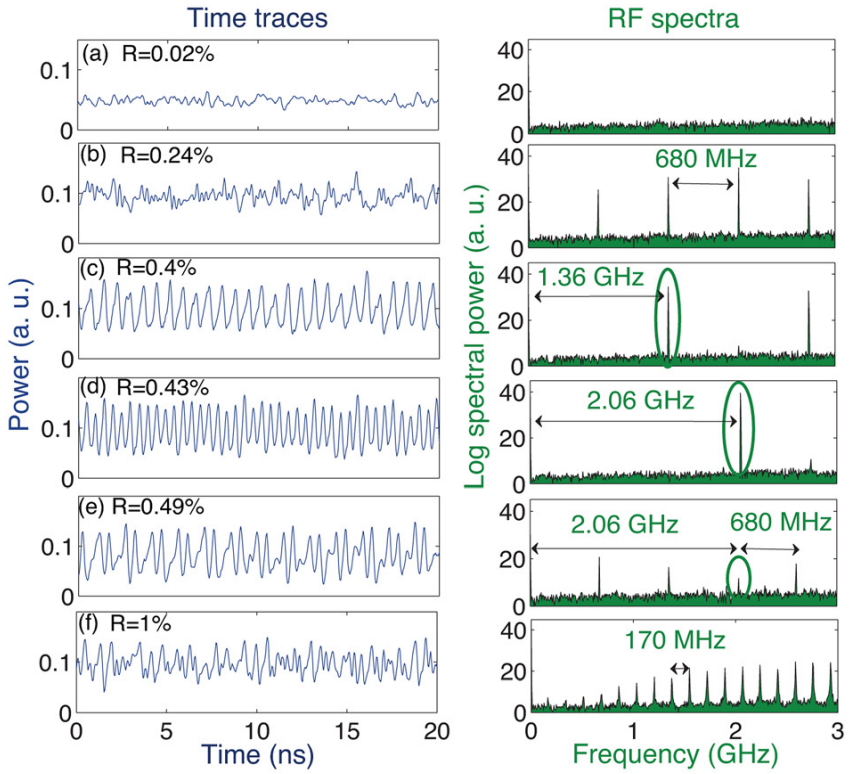

Figure 5.2: Time traces and corresponding radio-frequency (RF) spectra of a laser subjected to PCF, for five values of feedback strength R. In (c) and (d), the laser output power oscillates at two and three times the frequency of the external cavity f_{EC} = 680 MHz. Figure taken from Ref. [54].

ing feedback strengths. The linewidth of the laser will settle on a multiple of f_{EC} at some given values of feedback strength. Between such steady states (spectra b, d, f, h, j and l in Fig. 5.1), the laser has a chaotic behavior (c, e, g, i and k) [34]. In PCF, a similar phenomenon occurs but not with steady dynamics. For some values of feedback strength, the output power will oscillate and the peak at the frequency of the external cavity will be visible in the radio-frequency spectrum (RF spectrum). The experimental evidence of such-induced harmonic self-pulsations (ECMs) was given by our group in 2014 [54]. Such ECMs from PCF are presented in Fig. 5.1: the laser output power oscillates at 2 f_{EC} (time traces c in Fig. 5.1) or 3 f_{EC} (time traces d) [54]. Increasing feedback strength will make the laser oscillate at the next multiple of f_{EC} [58].

Such limit cycle was experimentally observed by our group in two different PCF configurations [52, 54]. At high values of feedback, ECMs always appear. That fact was named ECM crisis [65]: indeed, from a certain threshold of feedback strength, the system will mostly exhibit ECMs and multistability is typically found between ECMs of different frequencies and between ECM dynamics and chaos. Therefore, to know if the destabilization of the laser is related to phase-conjugation and not to parasitic conventional feedback, observing self-pumped states at super-harmonic frequencies of the external cavity frequency is a clear evidence that phase-conjugation occurs in the optical system.

Numerical and theoretical studies have been performed on the emergence of ECMs [58, 65], on the evolution of the frequency with the delay [66] and on the influence of all the laser parameters (α, time delay, carrier lifetime, pump and the dimensions of the mirror) [67].

5.2 Preliminary theoretical predictions

5.2.1 Frequencies of PCF

First, we try to understand the apparition of the ECMs from a numerical point of view, using a simple model. To familiarize with our numerical model, we will compare its results with the analytical results described by a previous study.

The first theoretical studies of the frequency of the external cavity modes on PCF, reported in Refs. [58, 65] used an unfiltered model derived from the Lang-Kobayashi equations. That model is studied in section 1.3.1. Subsequent studies [52, 67] used a filtered model, described in section 1.3.1: the feedback field is filtered by a parameter, named the finite penetration depth τ_r. It can be understood as the time it takes the light to penetrate the nonlinear crystal used for generating the PCM and it is directly proportional to the length of the crystal. The equation in its normalized form can be written (section 1.3.1):

$$\dot{Y} = (1 + i\alpha)YZ + \kappa U \tag{5.1}$$

$$T\dot{Z} = P - Z - (1 + 2Z)|Y|^2 \tag{5.2}$$

$$\tau_r \dot{U} = Y^*(t-\tau) - U \tag{5.3}$$

Where Y is the complex normalized electric field of the laser output, Z the normalized carrier population inversion, U the normalized feedback field of the PCF, τ_r the finite penetration depth mentionned above and T the ratio of the carrier and photon lifetimes. For analyzing PCF frequencies, we will focus our study on the dimensionless feedback strength parameter γ, the time delay τ and the pump current P. Ref. [67] proposed an in-depth study of the influence of each parameter.

The scenario of PCF bifurcations is that the system will first destabilize into ROs through a first Hopf bifurcation. Then, after successive Hopf bifurcations leading to self-pulsing external cavity modes, the laser will restabilize at the frequency of the last Hopf bifurcation [51, 58, 67]. From an analytical point of vue, the frequency σ and the amplitude C of the first Hopf bifurcation are analytically given by [51]:

$$C = \frac{1+2P}{T(1-\alpha^2)} \tag{5.4}$$

$$\sigma = \sqrt{\frac{2P}{T}} = \omega_{RO} \tag{5.5}$$

if we assume $P = O(1)$, $C = O(T^{-1/2})$, $\tau = O(T)$, $\tau_r \geq O(T^2)$ and $\sigma = O(T^{-1/2})$, T being the carrier lifetime ratio and α the linewidth enhancement factor.

In Eq. 5.5, σ is equal to ω_{RO}, the relaxation oscillations frequency: the first Hopf bifurcation does not correspond to an ECM but to the well-known undamping of the relaxation oscillations. The corresponding feedback strength γ is given by [51]:

$$\gamma = |C|\sqrt{1+\alpha^2} = \frac{(1+2P)\sqrt{1+\alpha^2}}{T|\alpha^2-1|} \tag{5.6}$$

Each successive Hopf bifurcation unlocks a new external cavity mode, whose frequency is the next harmonic of f_{EC} of the previous ECM [65]. For increasing feedback strength, the laser then encounters a last subcritical Hopf bifurcation and the system restabilizes into a steady-state. Under the assumptions $P = O(1)$, $C = O(T^{-1/2})$, $\tau = O(T)$, $\tau_r \geq O(T^2)$ and $\sigma = O(T^{-1/2})$, it

is characterized by [51]:

$$C = \sqrt{\frac{P|\alpha^2 - 1|}{T(1+\alpha^2)}} \tag{5.7}$$

$$\sigma = \sqrt{\frac{P(1+\alpha^2)}{T}} = \omega_{RO}\sqrt{\frac{1+\alpha^2}{2}} \tag{5.8}$$

$$\gamma = \sqrt{\frac{P|\alpha^2 - 1|}{T}} \tag{5.9}$$

One can notice that the frequency σ at the last bifurcation, i.e. the highest frequency that the system can reach, is proportional to ω_{RO}.

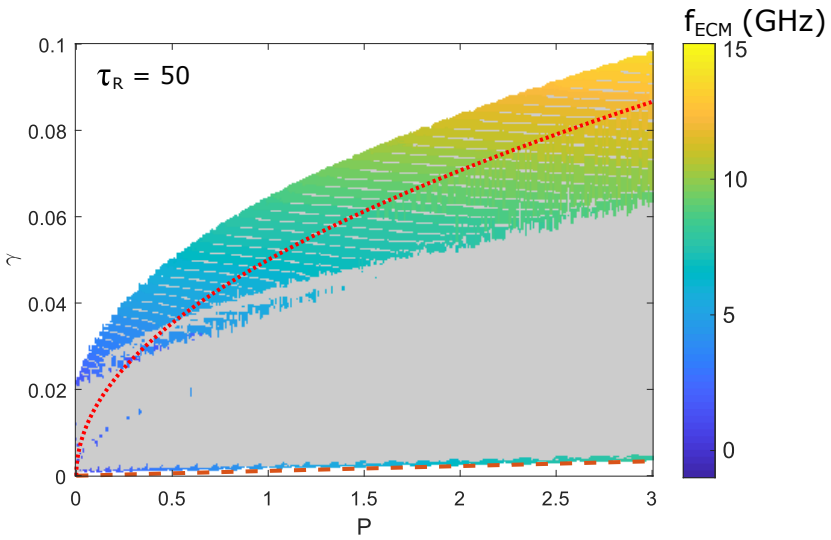

Figure 5.3: Simulated map of f_{ECM} in plane (P, γ), for $\tau_R = 50$. Steady states are indicated in white and chaos in grey. The dashed red line indicates the evolution of the value of the first bifurcation from Eq. 5.6 and the dotted red line, the value of the last Hopf bifurcation, obtained from Eq. 5.9.

Figure 5.3 shows the evolution of f_{ECM} versus γ and α, for $P \in [0,3]$, $\alpha = 2$ $T = 1200$, $\tau_R = 50$ (values used in Ref. [67]) and $\theta = 2500$. To measure f_{ECM}, we use a code that computes the distance between the extrema of the laser output field. If the distance is periodic, the system is pulsing and we report that frequency in our map. If the extrema are non-periodic, we consider the system is chaotic (grey in Fig. 5.4). Our group previously used that code in

Ref. [67]. The analytical positions in the plane (P,γ) of the first and last Hopf bifurcations are represented with, respectively, dashed and dotted red lines.

We observe that the analytical positions of the Hopf bifurcations do not perfectly fit the numerical solutions. However, the value of γ associated with the first Hopf bifurcation still varies quite linearly with P. Similarly, the relation between P and the feedback strength γ leading to the last Hopf bifurcation is close to the square root equation (5.8).

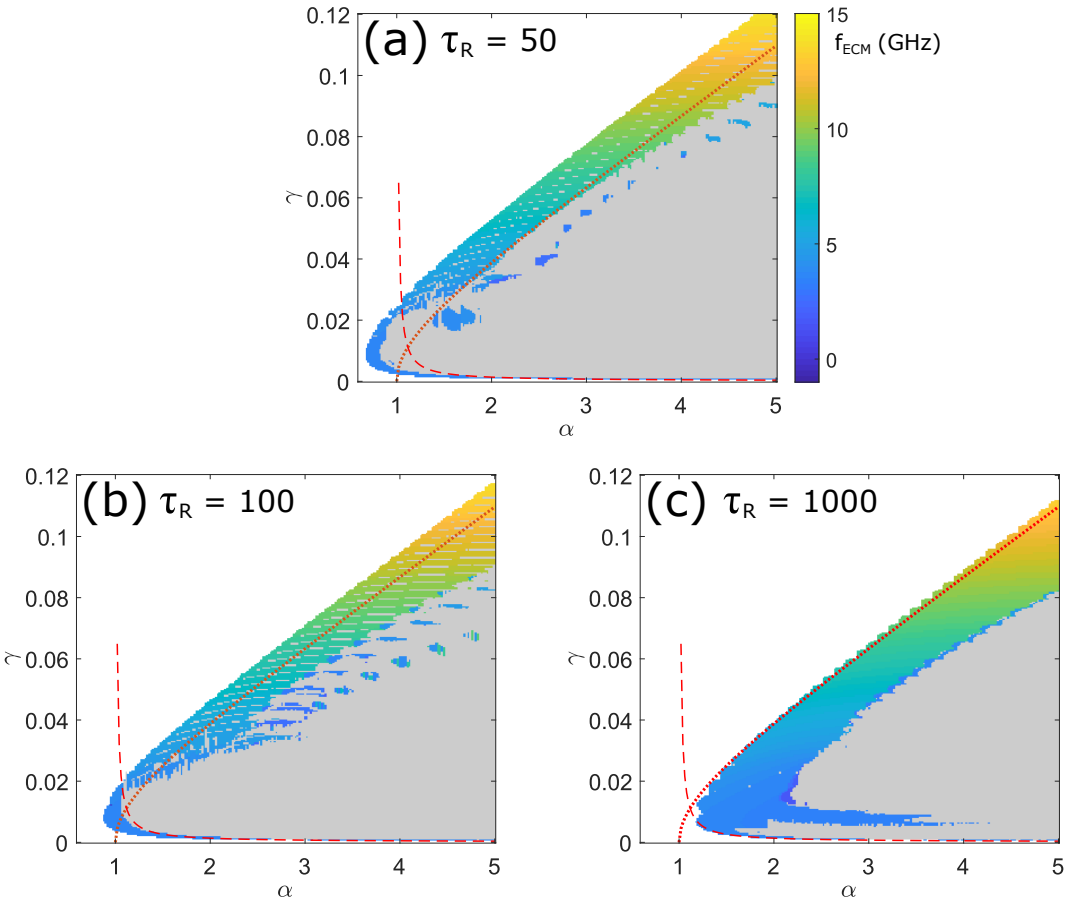

Figure 5.4: Simulated map of f_{ECM} in plane (α, γ), for $\tau_R = 50$ (a), $\tau_R = 100$ (b) and $\tau_R = 1000$ (c). Steady states are indicated in white and chaos in grey. The dashed red line indicates the evolution of the value of the first bifurcation from Eq. 5.6 and the dotted red line, the value of the last Hopf bifurcation, obtained from Eq. 5.9.

We plotted in Fig. 5.4 three maps of f_{ECM} versus γ and α, for $P = 0.6016$,

$T = 1200$ (values used in Ref. [67]), $\theta = 2500$ and $\tau_R \in \{50, 100, 1000\}$. The analytical solutions of the first and last Hopf bifurcations are again displayed with dashed and dotted red lines. These approximations closely fit the numerical values of destabilisation and restabilisation only for $\tau_r = 1000$, that corresponds to a 20 cm long $BaTiO_3$ crystal. The analytical solutions of equations 5.7, 5.8 and 5.9 are obtained for very large feedback strengths, which is not the case for our $5 \times 5 \times 5\ mm^3$ photorefractive crystal used as a phase-conjugate mirror. If we are using that later value, we rather obtain $\tau_r = O(T^{1/2})$ [52]. However, these analytical results remain highly interesting to understand the general bifurcation scenario of the filtered PCF and observe the global influence of each parameter. In particular, the proportionality between the frequency of the last Hopf bifurcation and the frequency of the ROs is an interesting feature to keep in mind during the experimental study of the frequency of the ECMs.

5.2.2 Influence of the feedback strength, of the delay and bistability

As mentioned above, the region of parameters corresponding to the external cavity modes has been previously studied in our group [51, 52, 54, 65, 67].

To understand the questions behind the experimental work that we performed in our thesis, we now report an example of numerical external cavity modes varying the feedback strength and the length of the external cavity. We take the equations 5.1 to 5.3 of filtered PCF, with the following parameters: α, the linewidth enhancement factor, is set to 2, P, the pump parameter above threshold is set to 0.06016 ; $T = 1200$, the ratio of carriers lifetime is set to 1200 and $\tau_r = 50$. That latter value corresponds to a crystal with 5 mm-long edges. All the values are taken from previous studies [52, 67] and also from section 3.3.2. The temporal values T, τ and τ_r are normalized by the photon lifetime, $\tau_p = 1.4$ ps. We take two values of external cavity length $f_{EC} = 1/\tau$, equal to 282 MHz and 1.02 GHz.

Figure 5.5 shows the simulated frequency of the ECMs f_{ECM} versus the dimensionless feedback strength γ. The pale pink and the red lines are plotted for f_{EC} =282 MHz ; the red lines was simulated for increasing γ and the pale

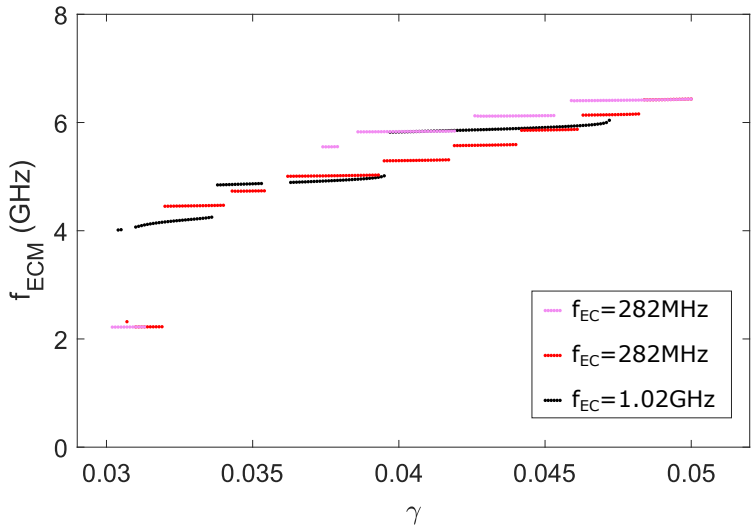

Figure 5.5: Theoretical evolution of the frequency of the ECMs f_{ECM} versus the dimensionless feedback strength γ. Three simulations were performed: the first one (pale pink) at an external cavity frequency f_{EC} equal to 282 MHz and for decreasing γ, the second one (red) at the same f_{EC} and for increasing γ, and the last one (black) at f_{EC} =1.02 GHz and for increasing γ.

pink lines for decreasing γ. The black curve corresponds to f_{EC} =1.02 GHz. First, Fig. 5.5 clearly illustrate the quantification of the frequencies of the ECMs around multiples of f_{EC}, as previously described in Refs. [51, 58]. It is also worth noting that the frequency of ECM varies a little bit from the absolute multiple of f_{EC}. For instance, when f_{EC} =1.02 GHz (black curve), we obtain at γ = 0.04, f_{ECM} =5.83 GHz= $5.72 f_{EC}$ and at γ = 0.047, f_{ECM} =5.9 GHz= $5.78 f_{EC}$.

Secondly, Fig. 5.5 shows that the laser, whatever the value of f_{EC}, oscillates at a frequency close to a similar frequency for different values of f_{EC}. The self-determination of the ECMs was previously described using both simulations and continuation methods: f_{ECM} depends on the feedback strength, and changing the external cavity length will only modify the multiple of f_{EC} at which the laser will oscillate [66]. The great novelty of PCF is that the self-pulsating frequency is much larger than $1/\tau$ and f_{RO} [52].

Figure 5.5 also shows that the system can dwell on different ECMs at the same value of γ and f_{EC}. With other values of γ, both curves will present

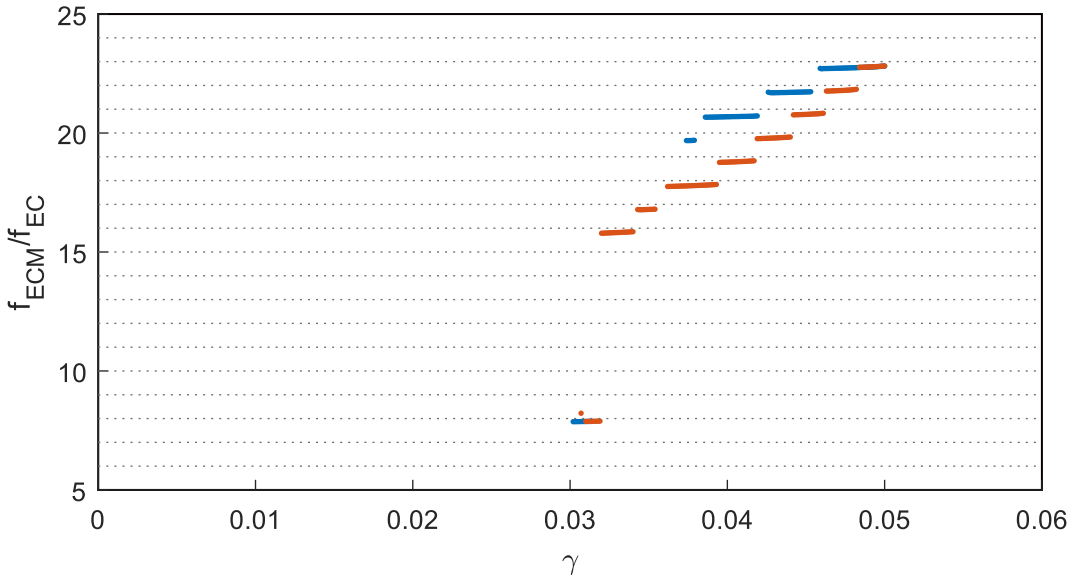

Figure 5.6: Evolution of the ratio f_{ECM}/f_{EC} versus the feedback strength γ. f_{EC}=282 MHz. The simulation was run for increasing γ (blue) and decreasing γ (red).

different kind of dynamics: one will oscillate while the other will be chaotic (no point displayed in the figure). It means various ECMs and chaos are theoretically bistable. It was confirmed using continuation methods in Ref. [65].

Figure 5.6 shows the same results than Fig. 5.5 but f_{ECM} is now divided by f_{EC}. The curve in blue was simulated for increasing γ and the curve in red for decreasing γ. It is highly instructive to see that $\frac{f_{ECM}}{f_{EC}}$ is always inferior to the nearest integer multiple n of f_{EC} (dotted lines). Changing the direction of the tunning of γ does not change that result. Therefore, that observation is not linked to a continuation of the stability at nf_{EC}. Please note that this result remains true if the delay is changed.

5.3 Experimental results about ECMs

In the previous section, we studied some numerical properties of the ECMs: their frequencies, the influence of the feedback strength and the delay and the bistability of the ECMs. Our study will now focus on experimental confirma-

tions of that predictions.

5.3.1 Observation of high-frequency ECMs

The highest frequency experimentally obtained till our work with PCF was 8.15 GHz, corresponding to the 13-th harmonics of $f_{EC} = 625$ MHz [52] .

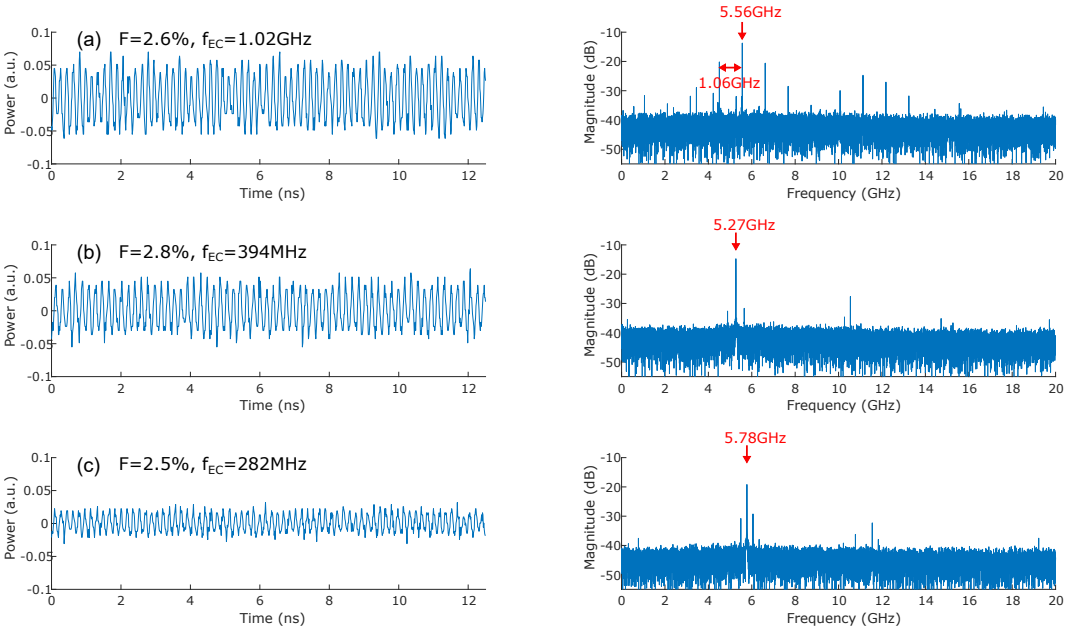

Figure 5.7: Experimental time series (left) and RF spectra (right) for three values of f_{EC} and at a pump current of $40mA$. They are measured at a similar value of feedback strength. In (a), f_{EC} equals 1.02 GHz, in (b) 394 MHz and (c) 282 MHz. The maximum frequency in the spectrum (f_{ECM}) is indicated with a red arrow.

We present below a few external cavity modes we observed with the setup described in section 2.2, i.e. a laser with a "cat" phase-conjugate mirror (PCM). The observed variations of the reflectivity of that mirror enables us to scan the various dynamics of the PCF for different values of reflectivity. The laser is here the SDL-5410, pumped with a current equal to 40 mA. At that value of current, $f_{RO} \approx 2.8$ GHz.

Figures 5.7 and 5.8 present six examples of time series, obtained for six different values of feedback strength and for three given f_{EC}. For each example,

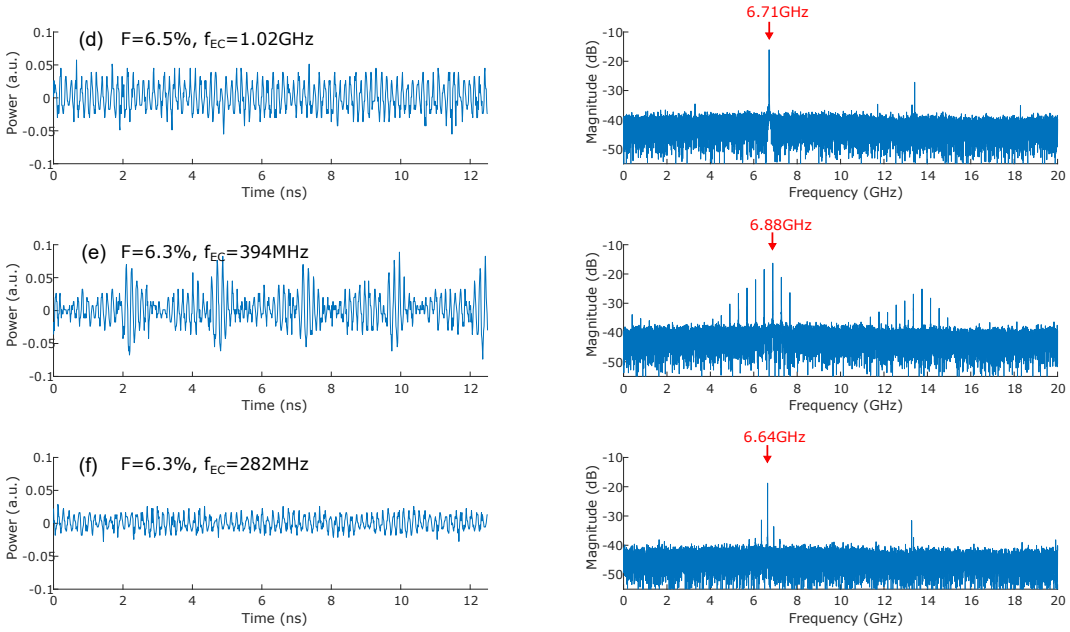

Figure 5.8: Experimental time series (left) and RF spectra (right) for three values of f_{EC} and at a pump current of $40mA$. They are measured at a similar value of feedback strength. In (d), f_{EC} equals 1.02 GHz, in (e) 394 MHz and (f) 282 MHz. The maximum frequency in the spectrum (f_{ECM}) is indicated with a red arrow.

a short piece of the time series is plotted on the left and the spectra corresponding to the full time series is plotted on the right. In Fig. 5.7, the feedback strength F is around 2.5%, a relatively low value, and in Fig. 5.8 F is around 6.5%, a high value.

Fig. 5.7 (a), (b) and (c) are obtained at similar values of feedback strengths but at different values of f_{EC}. They present a similar values of f_{ECM}, respectively 5.563 GHz (5th harmonics of f_{EC} = 1.02 GHz), 5.274 GHz (13th harmonics of f_{EC} = 394 MHz) and 5.776 GHz (20th harmonics of f_{EC} = 282 MHz). Similarly, the frequencies of the ECMs of Fig. 5.8 (d), (e) and (f) are respectively 6.707 GHz (6th harmonics of f_{EC} = 1.02 GHz), 6.877 GHz (17th harmonics of f_{EC} = 394 MHz) and 6.637 GHz (23rd harmonics of f_{EC} = 282 MHz). The offset in the multiples of the f_{EC} is probably related to the interaction dynamics inside the crystal. Indeed, the light may have longer path due to several round-trips in the crystal.

These six ECMs observations are good examples of the diversity of self-pulsing dynamics that can be obtained with our system. Figs. 5.7 (a) and 5.8 (e) display spectra with multiple peaks. Consequently, the corresponding time series, in particular in Fig. 5.8 (e), show modulation of the periodical time series. It corresponds to dynamical states where the system can't remain stable on one frequency and explore the neighboring frequencies. It is highly interesting because it enables us to distinguish the quantification of the ECMs. For instance, in Fig. 5.7 (a) the distance between two peaks in the spectrum is 1.06 GHz, which is close to f_{EC} = 1.02 GHz and in Fig. 5.8 that distance equals 395 MHz= f_{EC}. It is worth noting that in Figs. 5.7 and 5.8, feedback strengths are in the same range for the three different values of delay, and that the frequency of the ECMs are in that case similar. We will further investigate that observation in section 5.3.3.

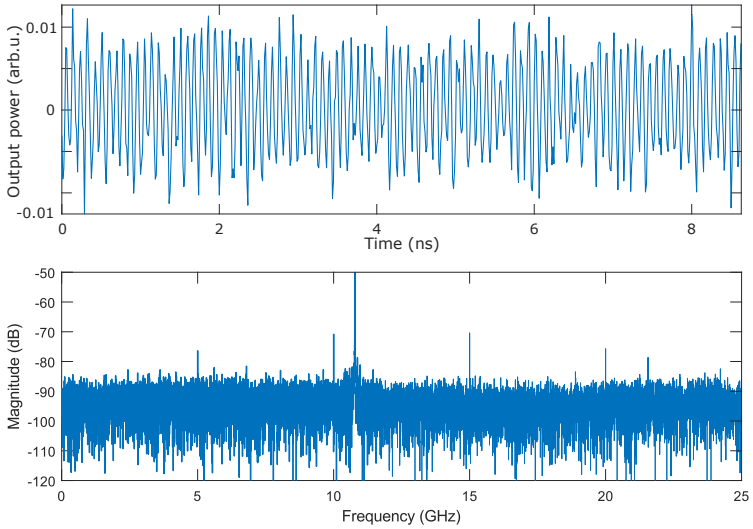

Figure 5.9: Experimental time series (left) and RF spectra (right) of an high frequency ECM.

Although our objective is not to observe the fastest external cavity modes but to qualify their properties, we report in Fig. 5.9 one of the largest ECM frequency ever observed. It was obtained with a SDL-5420 laser pumped at 80 mA and with an external cavity delay of 10.3 ns (f_{EC} =97 MHz). The frequency of the ECM is 11.07 GHz and it is the 114th harmonics of f_{EC}!

5.3.2 Evolution of the frequency of the ECMs versus the feedback strength

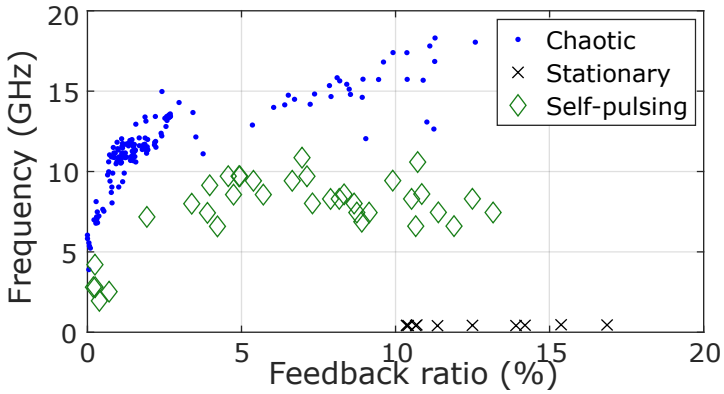

Figure 5.10: Evolution of the chaos bandwidth (blue dots, see chapter 3) and of the frequency of the self-pulsing modes (green diamonds) versus the feedback strength. Steady-states are indicated with black crosses. Figure taken from Ref. [99].

We now report the evolution of the frequency of the external cavity modes with respect to the feedback strength for the JDS-Uniphase SDL-5420 laser, presented in section 2.2.2.2. The laser is pumped with an electric current of 40 mA (f_{RO} = 3.6 GHz). We show in Fig. 5.10:

- the evolution of the frequency of the self-pulsing modes (green diamonds),
- the chaos bandwidth of the chaotic states [99] (blue dots),
- the steady-states (black crosses).

That figure was presented in section 3.3.1 to study the chaos bandwidth but one can make more analysis about the ECMs.

First, the first bifurcation from the steady-state into undamped relaxation oscillations is visible. The frequencies of the first oscillations, for a feedback strength < 0.5%, are around 4 GHz, close to f_{RO} =3.9 GHz. These oscillations are destabilized into chaos as the feedback strength increases. From a feedback strength of 4%, chaotic dynamics became rare and the system display external

cavity modes. From previous results, the frequency of the external cavity modes should increase by steps, each step corresponding to successive harmonics of f_{EC} [65] but the frequencies of the external cavity modes are somewhat mixed together. We will further study that observations in the next section. At high values of feedback strength, i.e. more than 10%, the laser restabilizes (black crosses).

We observe from our experiment that both ECMs and steady-state can coexist. No one studied the question of the subcriticity of the final Hopf bifurcation that leads to restabilization in PCF, since Green and Krauskopf studied the criticity of the Hopf bifurcations leading to ECMs but only in the region of low feedback strength [44]. Noise can also shift the bifurcation points. We can also link that observation to the uncertainty about the actual feedback rate of light coupled back into the laser or to the various possible geometric paths in the laser, which could modify the finite depth penetration inside the crystal and therefore the dynamics.

5.3.3 Influence of the delay on the frequency of the ECMs, and bistability

In that section, we study a still unsolved question: could the ECM frequency be independent of the delay? Indeed, we have reported ECMs oscillating at a multiple of the frequency corresponding to the external cavity length. Such a statement is theoretically predicted in section 5.2.2.

The setup of the experiment, discussed in section 2.2, is reproduced Fig. 5.11. The experimental parameters are the following: the edge-emitting laser diode is the SDL-5410 model, whose caracteristics were given in section 2.2.2.1. The pump current is set at 40 mA, as in section 5.3.1. The measurement arm is made of the Newport 1474-A photodetector and the Teledyne LeCroy 10-Zi-36 oscilloscope, and it enables measurements at frequencies up to 36 GHz. We record 1-μs long time series each third or quarter of second. That rate has been measured by using from the time stamp inscribed in each digital data file generated by the oscilloscope. It is constant for each run of 500 time series. As in sections 3.5.1 and 4.3.1, the PCM was mounted on a rail so that the

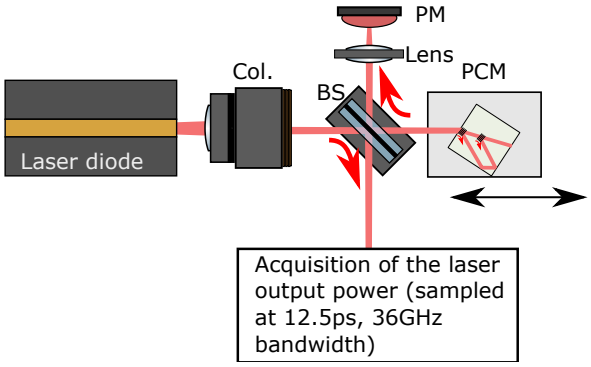

Figure 5.11: Setup of the experiment used in section 5.3.3. Note that the distance between the PCM and the edge-emitting laser can be tuned.

distance between the laser and the PCM can be tuned. We chose three distances: single-trip lengths equal to 14.7 cm, 38.0 cm and 53.2 cm, corresponding to f_{EC}=282 MHz, f_{EC}=395 MHz and f_{EC} = 1.02 GHz.

We plot in Fig. 5.12, f_{ECM} versus the feedback strength, for three values of f_{EC}. We have removed the non-self pulsing dynamics but they represent more than the three quarters of the time series that we recorded. The system generally encounters more or less long chaotic or steady state dynamics between two points presented in Fig. 5.12.

We observe several features. First, the distribution at integer multiples of f_{EC} is clearly visible, particularly for f_{EC} =1.02 GHz (yellow circles). For given values of feedback strength and f_{EC}, many values of f_{ECM} can be reached. However, these values are obtained at different times. The black dotted arrow in the green-bordered inset shows the evolution of f_{ECM} versus the feedback strength for six consecutive times, i.e. without chaotic dynamics in-between. The system reaches f_{ECM} ≈5.56 GHz, i.e. the 5th ECM. For smaller f_{EC} (282 MHz and 395 MHz), the larger number of ECMs did not enable us to observe similar dwelling on an ECM for more than two consecutive time series. These observations, coupled with the fact that many chaotic dynamics are also observed in the range of feedback associated with ECMs, clearly confirm the theoretical predictions of Ref. [65]: there appears a bistability between successive ECMs and between ECMs and chaos.

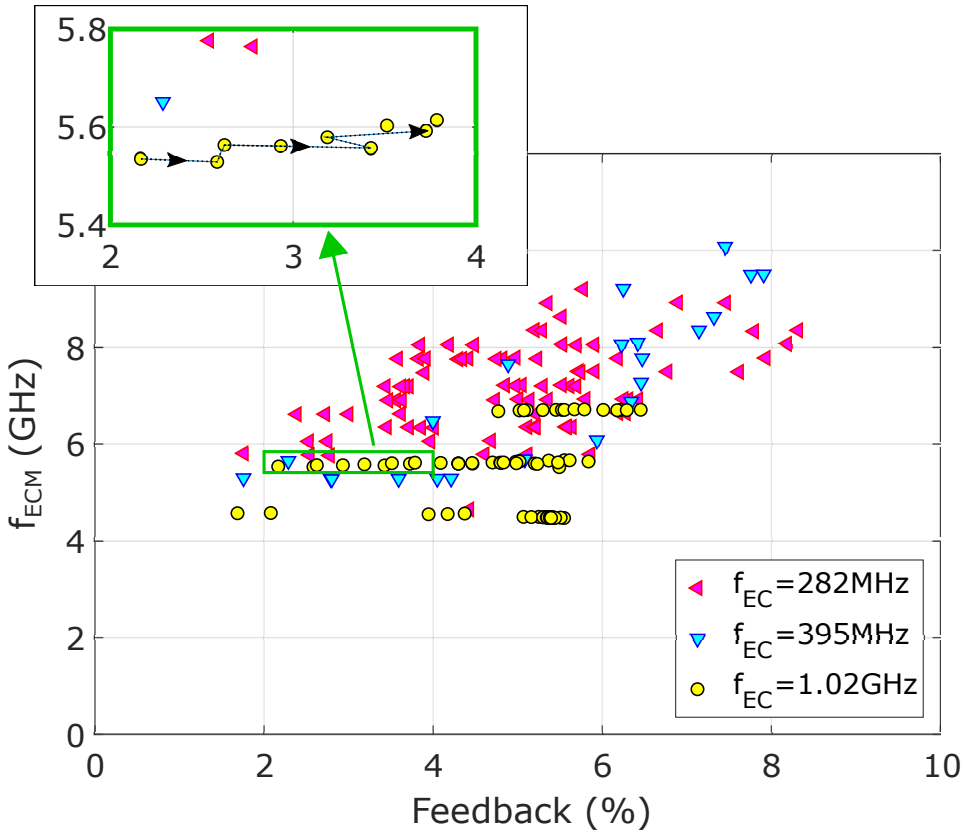

Figure 5.12: Evolution of f_{ECM} versus the feedback strength, for three values of f_{EC} (282 MHz in red triangles, 395 MHz in blue downward pointing triangles and 1.02 GHz in yellow circles). The inset is a zoom on the region delimited by the green rectangle. The black doted arrow in this inset presents the evolution of f_{ECM} and the feedback strength for six time series measured consecutively. The laser pump current was set at 40 mA.

Section 5.2.2 predicted that the frequency of the ECMs was self-determining, i.e. that for a given value of feedback and two values of f_{EC}, the two integer multiples n_1 and n_2 will be chosen so that $n_1 f_{EC,1} \approx n_2 f_{EC,2}$. The aforementioned bistability means that many values of n_1 and n_2 can be reached for a given value feedback. Still, Fig. 5.12 shows clearly that, for a given value of feedback strength, the values of f_{ECM} are in the same range of frequencies whatever is f_{EC}. For f_{EC} =1.02 GHz, the frequencies do not reach the high values obtained for f_{EC} =395 or 282 MHz. It is probably due to the instability

of the higher ECMs for that great value of f_{EC}. That confirms simulations that predicted the system can lock on a stable steady-state for lower values of feedback strength when the time delay is small, i.e. restabilization occurs at lower values of feedback strength [67].

5.3.4 Influence of the pump current on the frequency of the ECMs

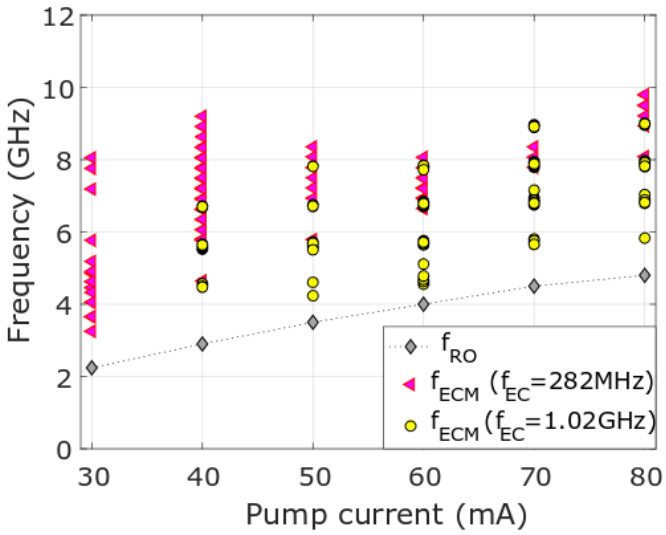

Figure 5.13: Distribution of the frequency of the external cavity modes for increasing pump current, at f_{EC} = 282MHz (red triangles) and f_{EC} = 1.02GHz (yellow circles). Each measured ECM is plotted at the corresponding values of f_{ECM} and pump. The frequency of the relaxation oscillations is indicated with gray diamonds.

We have studied the influence of the feedback strength and of the delay. However, a third experimental parameter can be easily controlled: the electric pump of the laser. To further continue our study, Fig. 5.13 illustrates the evolution of the frequency of the ECMs versus the pump current, for f_{EC} =282 MHz and 1.02 GHz; we compare it with f_{RO}. The experimental setup is the same than in the previous section, in particular the laser is the model SDL-5410. The conclusions are not easy to draw. In some cases high frequency ECMs can

be reached. For instance at a pump of 40 mA and f_{EC} =282 MHz, the frequency of the ECMs is higher than at a pump of 60 mA. Still, the frequencies of the lowest ECM and of the highest ECM globally increase with the pump, as does f_{RO}, thus confirming numerical predictions of section 5.2.1.

5.4 New PCF dynamics

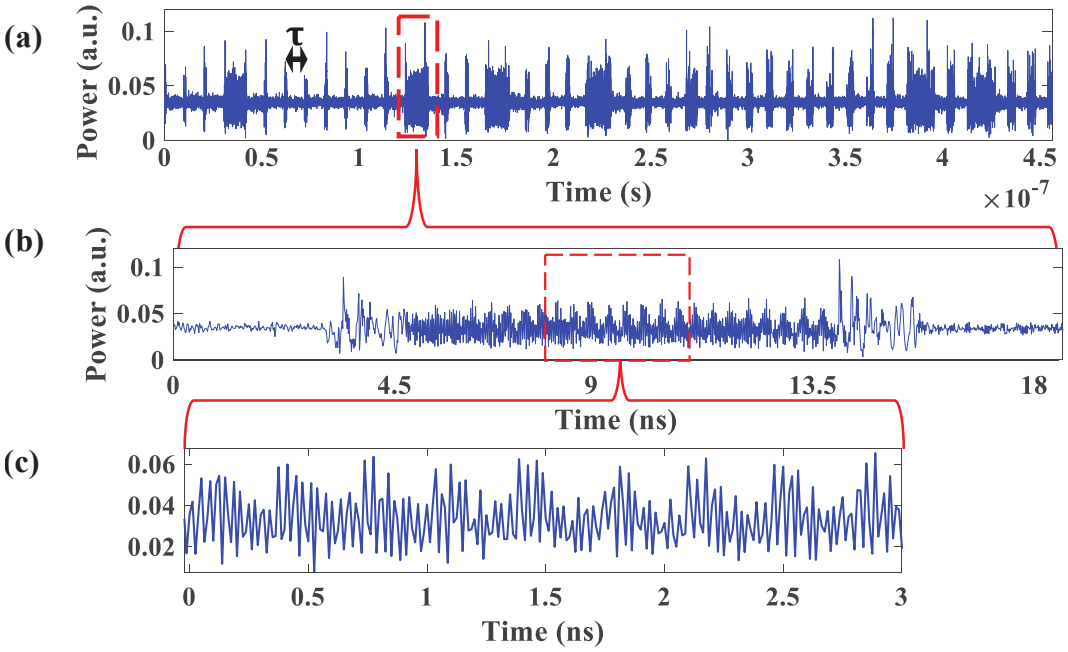

Figure 5.14: Example of time series showing intermittent high frequency pulses. (b) is a zoom on the red square in (a) and (c) is a zoom on the read square in (b).

Last, we observe new dynamics with PCF. Such dynamics were observed in the case of a long feedback (10.3 ns round-trip time). Figure 5.14 shows a time series obtained at feedback strength equal to 3.07%, with the SDL-5420 laser associated to a 10.3 ns external cavity. Similar time series were observed for values of feedback strength between 2.5% and 5%.

Figure 5.14 (a) shows a first feature of this time series: the system shows intermittent behavior, regularly repeated at a rate of τ. A more precise study, with Fourier analysis, shows that the low amplitude parts are ECMs and that

the short pulses are broadband chaotic signals. These time series have a global chaos bandwidth superior to 30 GHz (see chapter 3). The intermittent dynamics that appear irregularly between two chaotic pulses, as shown in Fig. 5.14 (b), are self-pulsations at a frequency around 30 GHz. The inset in Fig. 5.14 (c) shows that this frequency is modulated.

Feedback strength	Frequency of the ECMs	Frequency of the HF part
2.5%	11.26 GHz	33.4 GHz
2.7%	10.98 GHz	31.4 GHz
2.9%	10.98 GHz	30.6 GHz
3.3%	11.08 GHz	29.0 GHz
3.6%	11.08 GHz	30.8 GHz
3.7%	11.17 GHz	32.8 GHz
3.9%	11.17 GHz	32.4 GHz
4.3%	11.08 GHz	28.83 GHz
4.7%	11.47 GHz	29.79 GHz

Table 5.1: Frequencies measured in some time series with intermittent high-frequency (HF) pulses, mixed in ECMs.

In other time traces obtained at other values of feedback strength, the frequency of the ECM is different and so is the frequency of the high-frequency intermittent pulses. The values are presented in table 5.1. There is no clear relation between the frequency of the ECM and the frequency of the high-frequency pulses.

Conclusion

We have analyzed in details the external cavity modes of a PCF system. We confirmed various numerical prediction:

- We confirmed that high-frequency ECMs can be obtained, more than the 100th harmonics of f_{EC} in the case of long cavities ;

- We experimentally observed that the ECMs are self-determining solutions, i.e. the self-pulsation frequency remain constant whatever is the

delay value. This is a remarkable, unexpected feature in a laser with a delayed feedback.

- We demonstrated that the ECMs are bistable. The system will dwell on a given ECM but several ECMs can be obtained at a given feedback strength and the system switches between therefore different self-pulsing dynamics with time.
- We studied the role of the pump current and shows how a larger pump current enables higher frequencies.
- We reported a new dynamics, periodic switching between ECM and chaos with intermittent high-frequency pulses.

These various features are here unveiled experimentally for the first time. They make the PCF system a unique system in the field of delayed feedback lasers.

Chapter 6

Polarization rotated phase-conjugate feedback

One of the interesting aspects of the phase-conjugate feedback is the possibility to generate high-frequency self-pulsing oscillations, the so-called external cavity modes presented in chapter 5. The laser oscillates then at multiples of the external cavity frequency, hence much fater than the standard modulation limit of laser diodes, typically determined by the frequency of relaxation oscillation f_{RO}.

Alternatively, optical feedback can be used to excite new polarization modes. A standard edge-emitting laser diode naturally emits light polarized parallel to the active region. Such lasing modes are named transverse electric (TE) modes. The orthogonal transverse magnetic (TM) modes are strongly suppressed [157]. However, feedback can be used to excite the normally suppressed polarization, by injecting energy into the TM mode through rotation of the polarization of the feedback beam. This was first achieved using a quarter-wave plate, rotating the polarization of the feedback of the TE mode into the one of the TM mode and inversely [158]. In particular, such laser is able to generate square waves at a period equal to twice the feedback time delay τ. The apparition of the square waves can be intuitively described. The TE mode, emitting during a time τ is reinjected into the TM mode. That stimulates the TM mode and depreciates the TE mode for a duration τ. The TE mode will then be stimulated by the

feedback of the TM mode and so on [158]. Although the explanation appears as intuitive, it was later shown that the TE-TM dynamics results from a large set of bifurcations including Hopf bifurcations to square waves [159].

The system called Polarization Rotated Optical Feedback (PROF) therefore exhibits square wave (SW) dynamics: the laser output switches between the two modes at the frequency $\frac{1}{2\tau}$ [160]. It is demonstrated in [155] both experimentally and numerically that the PROF system can exhibit asymmetric oscillations on the plateau of the TM mode (Fig. 6.1). The frequency of these oscillations, f_p is larger than f_{RO} but remains limited to about 2-3 times f_{RO}.

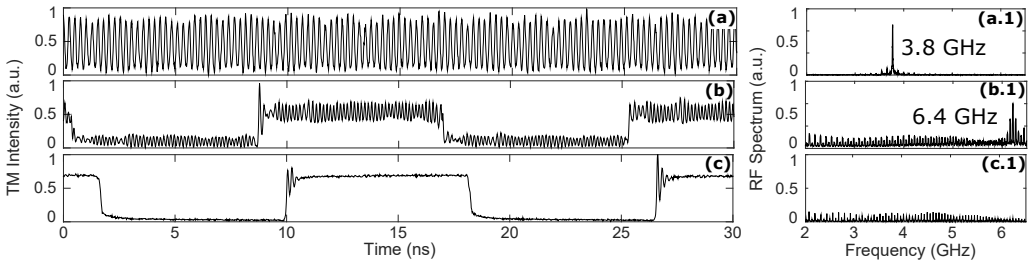

Figure 6.1: Experimental time-series (a-c) of the TM mode dynamics, in PROF configuration, and associated RF spectrums (a.1-c.1). (a) shows undamped relaxation oscillations at 3.8 GHz, (b) the self-pulsing square waves (the TE mode has standard square waves) at a larger value of feedback strength and (c) standard square-waves at a value of feedback strength larger than the one in (a) and (b). Figure taken from Ref. [155].

In this chapter we study the effect of combining the high-frequency external cavity modes from the PCF setup with the switching dynamics of the PROF, and investigate whether this mixing of frequencies enable us to have high frequency switching wave-forms. That study is based on the work done with master student Neco Kriel from Queensland University of Technology under my supervision.

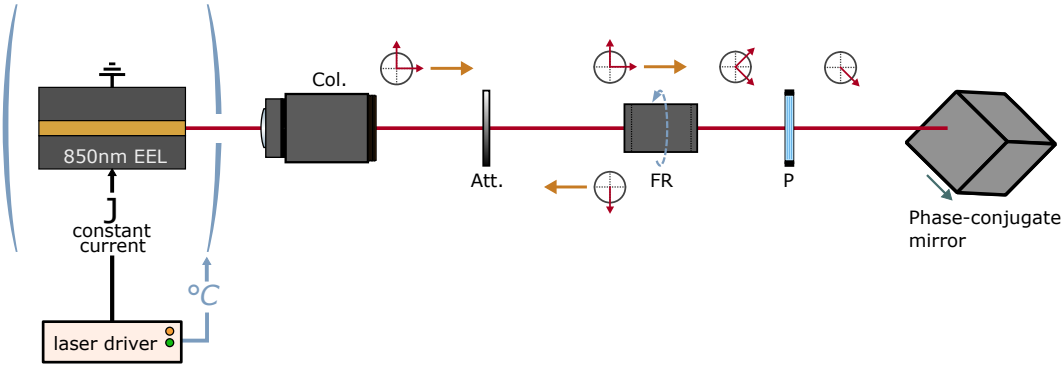

Figure 6.2: Proposed configuration of a PRPCF system. The output beam from an EEL is reflected by a phase-conjugate mirror into the laser. By rotating it by 45-degrees while going backward and going forward, the vertical (TE) polarization is sent back into the horizontal (TM) polarization.

6.1 Configuration

6.1.1 Proposed experimental setup

In this chapter we consider a setup consisting of an edge-emitting laser diode (EEL) with Polarization Rotated Phase Conjugate Feedback (PRPCF), as seen Figure 6.2. Typically this experimental setup is one where the TE-TM light emitted by a laser diode is rotated 45-degrees by a Faraday rotator (FR), followed by a polarizer (Pol.) removing the rotated vertical (TE) polarization. The reflected light is then again rotated by 45-degrees, resulting in a feedback beam, parallel to the TM axis when injected back into the system. A phase conjugate mirror typically reflects only one polarization, and the crystal's c-axis must be parallel to the 45° rotated TE-mode. Finally, an attenuator (Att.) is used to control the feedback strength.

In practice, a half-wave plate can be added between the polarizer and the PCM to avoid tilting the crystal at 45°.

6.1.2 Associated equations

All types of PROF systems with an EEL can be mathematically modelled using a modified Lang-Kobayashi (LK) model [31], and described mathematically

using non-dimensionalised set of rate equations [49, 161, 162]:

$$\dot{E}_1(s) = (1+i\alpha)E_1(s)Z(s) + R\xi_1(s) \tag{6.1}$$

$$\begin{aligned}\dot{E}_2(s) = &\left[(1+i\alpha)\kappa(Z(s)-\beta) - i\Omega\right]E_2(s) \\ &+ \eta\sqrt{\kappa}E_F(s) + R\xi_2(s)\end{aligned} \tag{6.2}$$

$$\begin{aligned}T\dot{Z}(s) = &P - (1+2Z(s))\left(|E_1(s)|^2 + |E_2(s)|^2\right) \\ &- Z(s)\end{aligned} \tag{6.3}$$

The parameters in this model corresponds to an extension of the dimensionless PROF system [49], where τ_R is the finite depth penetration of the PCM, τ_P is the photon lifetime, and $R\xi_1(s)$ and $R\xi_2(s)$ represent the zero-mean and R-variance of the Gaussian white noises present in the system, respectively.

Further, E_F represents the normalized complex field of the feedback wave, where in a PROF system, $E_F = E_1(s-\tau)$, and for a phase-conjugate feedback (PCF) setup, $E_F = {E_1}^*(s-\tau)$. To explain the restabilization of the steady state for high values of feedback ratio, we have to account for a filtered PCF model [52] and therefore we add a fourth equation to our system, (Equation 6.7), in which τ_R is the finite depth penetration. It has been demonstrated that a PCM with $\tau_R \gg 1$ tends to filter out the infinitely high frequencies generated in PCF [50].

$$\dot{E}_1(s) = (1+i\alpha)E_1(s)Z(s) + R\xi_1(s) \tag{6.4}$$

$$\begin{aligned}\dot{E}_2(s) = &\left[(1+i\alpha)\kappa(Z(s)-\beta) - i\Omega\right]E_2(s) \\ &+ \eta\sqrt{\kappa}E_F(s) + R\xi_2(s)\end{aligned} \tag{6.5}$$

$$\begin{aligned}T\dot{Z}(s) = &P - (1+2Z(s))(|E_1(s)|^2 + |E_2(s)|^2) \\ &- Z(s)\end{aligned} \tag{6.6}$$

$$\tau_R\dot{E_F} = {E_1}^*(s-\theta) - E_F \tag{6.7}$$

We consider typical parameter values as defined in Table 6.1, to compare with our own analysis and also to be consistent with the literature on PROF systems [49].

Table 6.1: Definitions and default values used for parameters used in the analysis.

	Default value:	**Parameter definitions:**
P	0.6	Pump parameter
T	250	Carrier-cavity lifetime ratio
θ	$\in [1000, 7000]$	Normalized delay
η	$\in [0, 0.3]$	Feedback ratio
κ	0.96	TM-TE modes gain ratio
β	$\frac{1-\kappa}{2\kappa}$	TM mode additional losses
α	2	Linewidth enhancement factor
Ω	0	TM-TE modes detuning
τ_R	50	PCM finite penetration depth
τ_P	1.4×10^{-12}	Photon lifetime
R	10^{-12}	Variance of noise

6.2 Numerical results

6.2.1 Typical Bifurcation Scenario

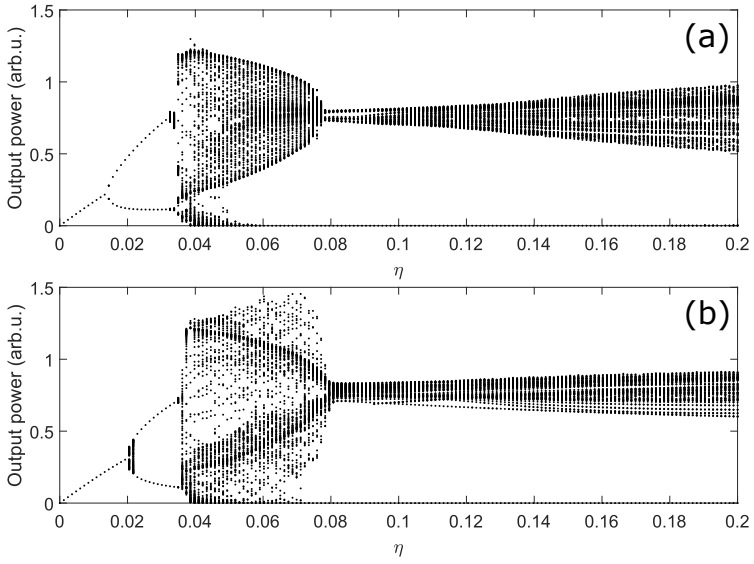

Figure 6.3: Bifurcation diagrams of the TM output power for (a) PROF and (b) PRPCF.

Considering typical parameter values, as defined in Table 6.1, with $\theta = 7000$, $\kappa = 0.96$, and $\alpha = 2$, we give a typical bifurcation diagram for a PRPCF system in Fig. 6.3. For low values of feedback ratio, $\eta \leq 0.02$, we observe steady-state solutions, where both polarizations are lasing, and by increasing the feedback ratio, we observe the output power of the vertical polarization increases, while the horizontal polarization's output power decreases. This result is reported in the PROF system as well, and intuitively makes sense, since as we increase the feedback ratio we are increasing the amount of energy transferred into the normally depressed polarization. Through a Hopf bifurcation, we observe a region, $\eta \in [0.0202, 0.035]$, of mixed-mode undamped oscillations at the relaxation frequency of the laser (f_{RO}).

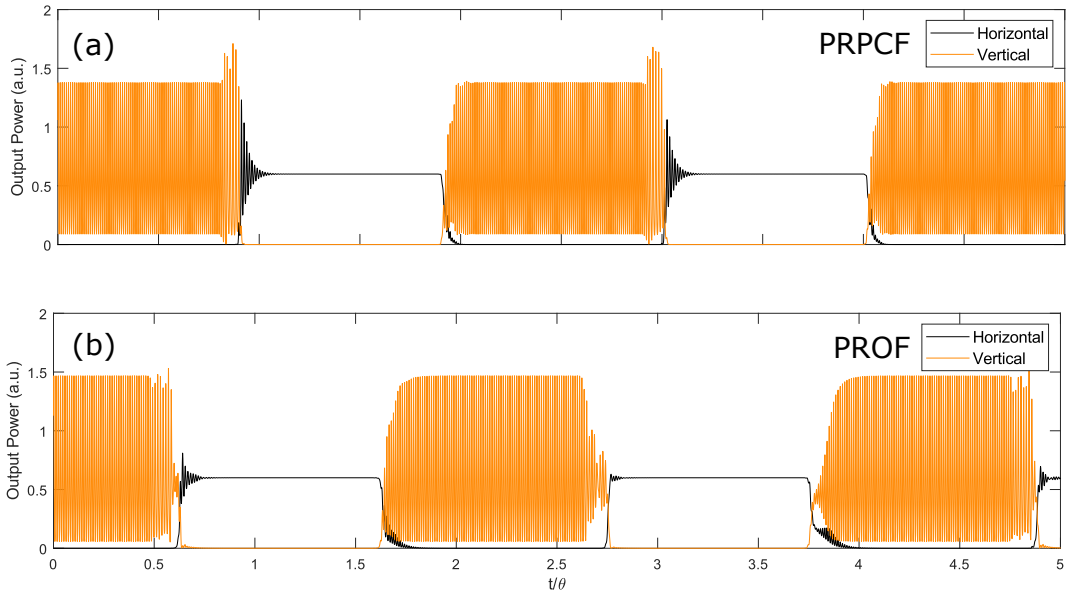

Figure 6.4: Examples of the square-wave (SW) dynamics we observe in a typical setup with (a) PRPCF with $\eta = 0.0498$ and (b) PROF with $\eta = 0.0407$. Time t is normalized by the delay θ =8.9 ns.

Continuing to increase the feedback ratio, we observe a very narrow region of chaos before the transition into SW dynamics. As shown in Fig. 6.4, the TE mode shows fast oscillations on the upper plateau while the ground plateau is steady. Further, the horizontal polarization has a short transient state, with damped oscillations at f_{RO}, and lases with steady dynamics for the duration

of θ. That dynamics is similar to the one obtained in COF, shown in Fig. 6.4 (b). The vertical polarization oscillates at f_P for a duration of θ along the upper plateau, where f_P has previously been studied in PROF systems [155]. In particular, Ref. [155] analytically obtained $f_P = f_{RO}\sqrt{\frac{k}{2}(1+\alpha^2}$. The vertical polarization continues to oscillate after a period of θ, however, the oscillations are damped and the oscillating frequency changes from f_P to f_{RO}.

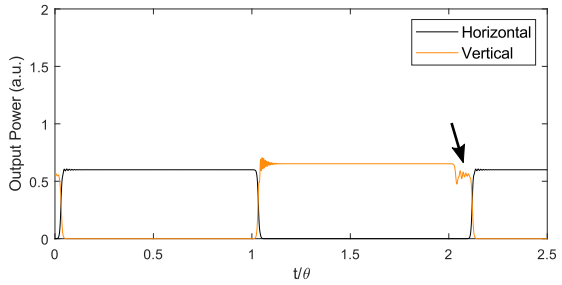

Figure 6.5: Examples of the quasi-steady square-wave (QSW) dynamics we observe in a typical PRPCF setup with $\eta = 0.0995$. Time t is normalized by the delay θ =8.9 ns. The black arrow indicates the secondary plateau.

When we increase the feedback ratio to $\eta \approx 0.082$, the vertical polarization's oscillations stabilizes, resulting in a regime of SW we distinguish from typical SWs, and we name this quasi-steady SWs (QSW), see Fig. 6.5. Particularly, this QSW solution has a secondary, lower plateau acting as transient state at the end of the SW (indicated with a black arrow in Fig. 6.5). This shape of QSWs has also been reported for PROF and is noise-sensitive [49]. Beyond $\eta \geq 0.082$ we only observe QSW solutions. All these bifurcations have been reported for PROF systems [155].

6.2.2 Influence of Parameters on Bifurcation Scenario

We investigate how the regions of parameter space corresponding to different dynamical regimes established earlier for a typical bifurcation scenario changes, when different parameters are varied. Particularly, we use the typical parameters defined in Table 6.1 and investigate the dynamical influence of

varying the delay, $\theta \in [150, 10000]$, and the PCM's finite penetration depth, $\tau_R \in [0, 10000]$.

We observe that the frequencies associated with the PRPCF dynamics are insensitive to changes in the delay parameter (θ), except for cases of very short delay, where $\theta < f_{RO}$. For short delay, we don't observe any SW solutions, since the frequency associated with the delay is too short when compared with . This non-dependency from values of θ is a result that has already been shown to be the case for the PROF system [155]. However, the values of η associated with the bifurcation points vary with the delay θ.

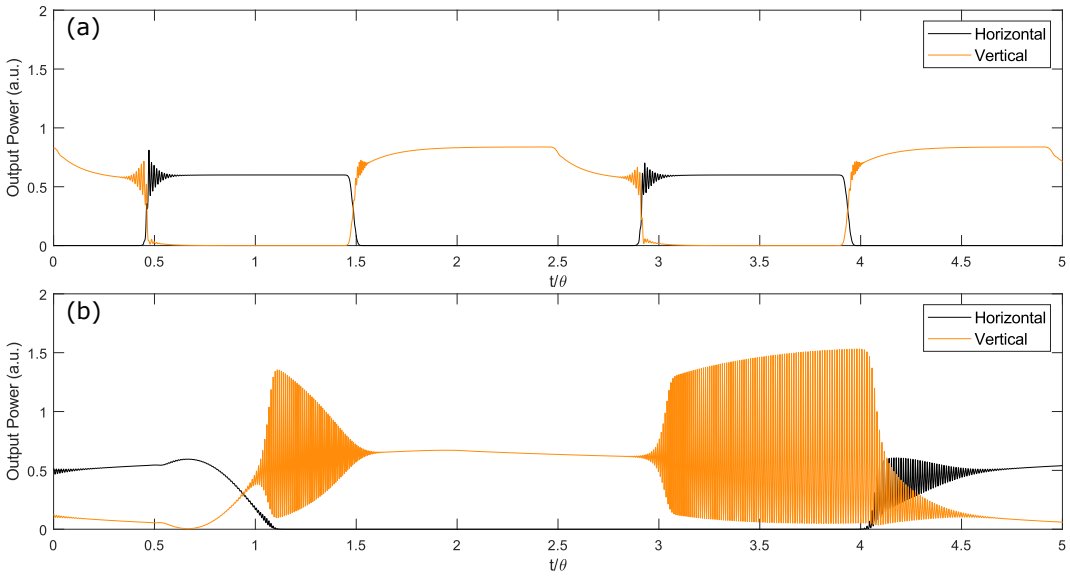

Figure 6.6: Time traces of square waves obtained at large values of finite depth penetration τ_R. (a) $\tau_R = 1000$ and $\eta = 0.28422$ and (b) $\tau_R = 10000$ and $\eta = 0.22042$.

In the case of zero finite penetration depth for the PCM, that is $\tau_R = 0$, we find that the dynamics of PROF and PRPCF systems are very similar. Particularly, for larger values of feedback ratio, higher frequencies appear in the transient states of the upper plateau for the TE mode. For large values of τ_R, when $\tau_R = 1000$, and for values of feedback ratio beyond the Hopf bifurcation point, $\eta \geq 0.0202$, we observe that the SW regimes are modified, and the high frequencies of the square TE mode's signal are filtered, see Fig. 6.6 (a). Further,

when we increase the PCM's finite penetration depth to $\tau_R = 10000$ (Fig. 6.6 (b)), we notice that the filtering now occurs on the TM mode as well. High frequencies dominate the transient state of the upper plateau in the TE and TM modes. Note that $\tau_R = \{1000, 10000\}$ corresponds to a nonlinear medium whose length is not realistic and therefore these values of τ_R are interesting only from a mathematical perspective.

6.2.3 Study of the first bifurcation point

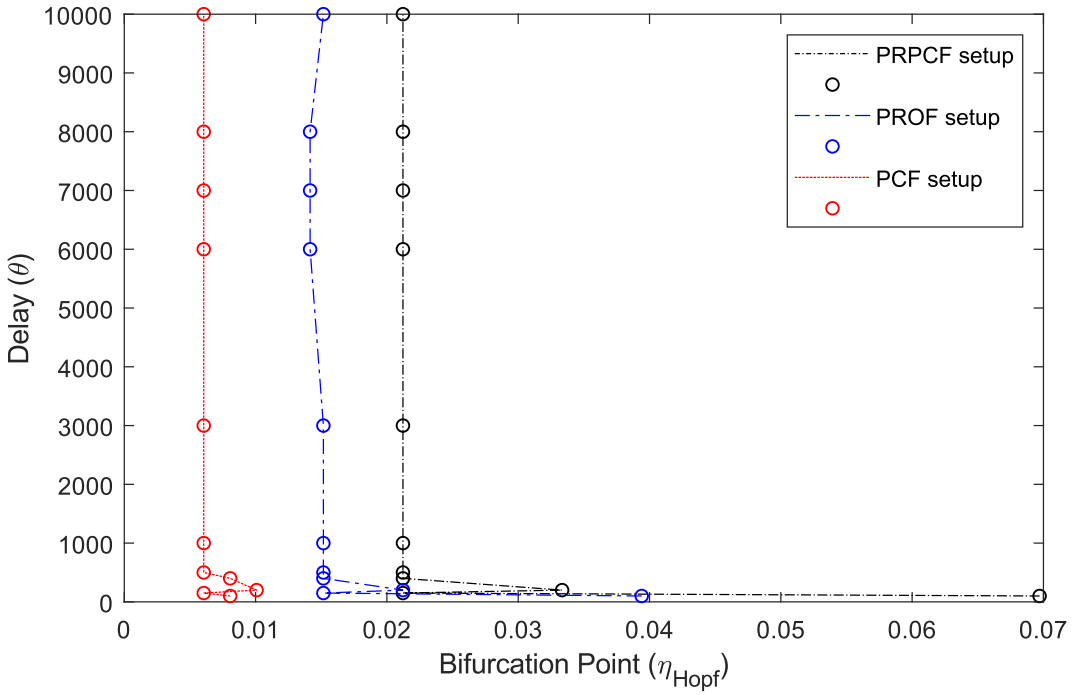

Figure 6.7: Position η_{Hopf} of the first Hopf bifurcation, for various values of θ.

It is interesting to observe the position of the first Hopf bifurcation, i.e. the destabilization of the steady state into undamped relaxation oscillations as it occurs in PCF, PRPCF and PROF.

We present Fig. 6.7 the evolution of η_{Hopf}, the value of feedback strength associated with the first Hopf bifurcation, versus the time delay θ. η_{Hopf} becomes independant of θ when $\theta \gg f_{RO}$, as predicted for PCF in Ref. [51]

and for PROF in Ref. [49]. We have $\eta_{Hopf} \to 0.006$ for PCF, $\eta_{Hopf} \to 0.015$ for PROF and $\eta_{Hopf} \to 0.021$ for PRPCF.

Conclusion

We have studied a new configuration, with phase-conjugate feedback on the depreciated TM mode of the laser diode.

Since both PCF and PROF are known to generate high frequency self-pulsations, with frequency superior to f_{RO}, it was initially thought that combining both setups and therefore suggesting a PRPCF configuration would enable to control and maybe even improve the stability of the high frequency dynamics.

The observations do not confirm the initial claim:

- the resulting dynamics is dominated by square waves with pulsations on the plateau at frequency f_P, which is close to the one observed in PROF without phase-conjugation.
- ECM dynamics of PCF do not appear in the PRPCF system, or in other words the rotated feedback suppresses the dynamical features of the PCF system!
- The instability, to undamped relaxation oscillations and later square waves takes place for about the same feedback strength in PROF and PRPCF and the bifurcation point is about the same independtly of the value of the delay.
- The finite time of the interaction in the nonlinear medium acts like a filter for both the pulsations on the square waves and for the time to switch between the TE/TM modes.

Chapter 7

General conclusion and perspectives

We conclude here our study of the dynamics of a laser diode subjected to PCF. First, we present a summary of the results obtained during this thesis. Then, we give some perspectives for future works about PCF.

7.1 Summary of the results

This thesis studied the effect of phase-conjugate feedback (PCF) on laser diode dynamics, in the more general field of chaotic laser diodes. Previous works, presented in Chapter 1, had shown the specificity of the nonlinear dynamics of a laser diode subjected PCF:

- The chaos obtained from PCF has a larger bandwidth than the one obtained from COF.
- The PCF enables the generation of high-frequency self-pulsing states with a frequency equal to a multiple of the frequency of the external cavity f_{EC}.
- The finite penetration depth in the nonlinear phase-conjugate mirror (PCM) leads to a restabilization of the laser at high values of feedback strength.

Then, in chapter 2, we presented how our experiment was performed. Perform an experiment with PCF requires a careful study of the PCM geometry to obtain interesting values of feedback strength. In particular, we observe a spontaneously varying reflectivity in the PCM and therefore we are able to scan different values of feedback strengths without human intervention during the measurement. The characteristics of the laser diodes were also presented, in particular the evolution of their output power and frequency of the relaxation oscillations f_{RO} with the bias current.

In chapter 3, we introduced the study of the chaos bandwidth and of the spectral flatness. We observed chaos bandwidth larger than 30 GHz and spectral flatness up to 0.75, which indicates a complex chaos. We studied the influence of the feedback strength on these two indicators. We saw a saturation of the chaos bandwidth and of the effective bandwidth and we relates that result to the non-instantaneous response of the PCM. We also observed that the length of the cavity has no influence on the chaos bandwidth and spectral flatness. Last, the study of the influence of the pump current showed that an increase of the pump current increases the chaos bandwidth while the spectral flatness does not significantly varies.

Then, in chapter 4, we continued our analysis of the properties of chaos generated by a laser diode with PCF by calculating the permutation entropy. We reported high values of permutation entropy, superior to 0.93 on a large range of feedback values. The length of the external cavity does not influence the permutation entropy but we experimentally observed a saturation of the permutation entropy at high values of feedback strength. This saturation was also observed in simulations. Last, the permutation entropy values remain high when the pump current varies.

In chapter 5, we focused the study on the external cavity modes of the PCF. We reported high frequencies of ECMs, f_{ECM}, around 11 GHz. We also observed that an increase feedback strength leads to higher values of f_{ECM}. However, while f_{ECM} is always a multiple of f_{EC}, f_{ECM} remains in the same region if the length of the cavity varies while the feedback strength is constant. We also observed that different values of f_{ECM} can be obtained at the same value of feedback strength, which indicates bistability. We observe that increasing

the pump current enables the generation of higher values of f_{EC}. Last, we presented an intermittency between ECMs and higher frequency pulses.

Last, in chapter 6, we introduced a new setup, the polarization rotated phase-conjugate feedback (PRPCF), where the feedback is sent into the normally suppressed orthogonal mode of the laser diode. We numerically report the generation of square waves, and also of square waves with fast oscillations on the high plateau of the TM mode. These phenomena were also observed in conventional polarization rotated optical feedback (PROF) but the bifurcations occur at different values of feedback strength.

7.2 Perspectives

Since 2011, our group has extensively studied the dynamics of PCF. I consider that I have addressed the main questions that remained before my thesis started: the influence of the delay on the chaos and on the ECMs and the bistability of the ECMs. The complexity and large chaos bandwidth of the chaotic signal obtained from PCF was also put in evidence. However, many aspects of the PCF remain unknown.

The following aspects could be considered:

- We have used a photorefractive $BaTiO_3$ crystal with a fixed length to generate the PCF. It may be interesting to study the influence of the length of the crystal on the dynamics, since a smaller crystal would have a lower finite depth penetration time.

- The PCM has spontaneous variations. However, commercial applications require a monitoring of the feedback strength. It would be necessary to stabilize the reflectivity of the PCM. Using another type of PCM, such as phase-conjugation obtained in semiconductor materials may enable a better control of the feedback strength.

- We have not demonstrated the possible applications of the broadband and complex chaos obtained from PCF. It might be interesting to use the

PCF as a real-time random number generator or as the source of light in a chaotic lidar.

- Last, the intermittency between high-frequency pulses and ECMs described in section 5.4 of chapter 5 was not predicted in simulations. Further study could be launched on these dynamics.

References

[1] M. Planck, "Über eine verbesserung der wienschen spektralgleichung," *Verhandlungen der Deutschen Physikalischen Gesselschaft*, no. 2, pp. 202–204, 1900.

[2] A. Einstein, "Über einen die Erzeugung und Verwandlung des Lichtes betreffenden heuristischen Gesichtspunkt," *Verhandlungen der Deutschen physikalischen Gesellschaft*, vol. 322, no. 6, pp. 132–148, 1905.

[3] ——, "Strahlungs-emission und -absorption nach der quantentheorie," *Verhandlungen der Deutschen physikalischen Gesellschaft*, vol. 18, pp. 318–323, 1916.

[4] H. Kopfermann and R. Ladenburg, "Untersuchungen über die anomale dispersion angeregter gase. ii. teil. anomale dispersion in angeregtem neon," *Zeitschrift für Physik*, vol. 48, pp. 26–50, 1928.

[5] J. Hecht, "A short history of laser development," *Applied Optics*, vol. 49, no. 25, p. F99, sep 2010.

[6] T. H. Maiman, "Stimulated Optical Radiation in Ruby," *Nature*, vol. 187, no. 4736, pp. 493–494, aug 1960.

[7] R. N. Hall, G. E. Fenner, J. D. Kingsley, T. J. Soltys, and R. O. Carlson, "Coherent Light Emission From GaAs Junctions," *Physical Review Letters*, vol. 9, no. 9, pp. 366–368, nov 1962.

[8] B. Lax, "Semiconductor Lasers," *Science*, vol. 141, no. 3587, pp. 1247–1255, sep 1963.

[9] J. J. Coleman, "The development of the semiconductor laser diode after the first demonstration in 1962," *Semiconductor Science and Technology*, vol. 27, no. 9, p. 090207, sep 2012.

[10] H. Kroemer, "A proposed class of hetero-junction injection lasers," *Proceedings of the IEEE*, vol. 51, no. 12, pp. 1782–1783, dec 1963.

[11] C. W. Wilmsen, H. Temkin, and L. A. Coldren, *Vertical-cavity surface-emitting lasers: design, fabrication, characterization, and applications*. Cambridge University Press, 2001, vol. 24.

[12] C. Chang-Hasnain, J. Harbison, L. Florez, and N. Stoffel, "Polarisation characteristics of quantum well vertical cavity surface emitting lasers," *Electronics Letters*, vol. 27, no. 2, p. 163, 1991.

[13] M. San Miguel, Q. Feng, and J. V. Moloney, "Light-polarization dynamics in surface-emitting semiconductor lasers," *Physical Review A*, vol. 52, no. 2, pp. 1728–1739, aug 1995.

[14] A. Larsson, "Advances in VCSELs for communication and sensing," *IEEE Journal on Selected Topics in Quantum Electronics*, vol. 17, no. 6, pp. 1552–1567, 2011.

[15] C. K. Kao and G. A. Hockham, "Dielectric-fibre surface waveguides for optical frequencies," *Proceedings of the Institution of Electrical Engineers*, vol. 113, no. 7, pp. 1151–1158, jul 1966.

[16] U. Wandinger, "Introduction to Lidar," in *Lidar*. New York: Springer-Verlag, 2011, pp. 1–18.

[17] N. Takeuchi, H. Baba, K. Sakurai, and T. Ueno, "Diode-laser random-modulation cw lidar," *Applied Optics*, vol. 25, no. 1, p. 63, jan 1986.

[18] J. Reagan, H. Liu, and J. McCalmont, "Laser diode based new generation lidars," in *IGARSS '96. 1996 International Geoscience and Remote Sensing Symposium*, vol. 3, no. 520. IEEE, 1996, pp. 1535–1537.

[19] R. T. Ku, E. D. Hinkley, and J. O. Sample, "Long-Path Monitoring of Atmospheric Carbon Monoxide with a Tunable Diode Laser System," *Applied Optics*, vol. 14, no. 4, p. 854, apr 1975.

[20] E. D. Hinkley, R. T. Ku, K. W. Mill, and J. F. Butler, "Long-path monitoring: advanced instrumentation with a tunable diode laser," *Applied Optics*, vol. 15, no. 7, p. 1653, jul 1976.

[21] G. T. Forrest, "Tunable diode laser measurement of methane, ethane, and water vapor in cigarette smoke," *Applied Optics*, vol. 19, no. 13, p. 2094, jul 1980.

[22] J. Barrow-Green, "Oscar II's prize competition and the error in Poincaré's memoir on the three body problem," *Archive for History of Exact Sciences*, vol. 48, no. 2, pp. 107–131, 1994.

[23] E. N. Lorenz, "Deterministic Nonperiodic Flow," *Journal of the Atmospheric Sciences*, vol. 20, no. 2, pp. 130–141, mar 1963.

[24] A. Uchida, *Optical communications with chaotic lasers*, 2012.

[25] M. Sciamanna and K. A. Shore, "Physics and applications of laser diode chaos," *Nature Photonics*, vol. 9, no. 3, pp. 151–162, mar 2015.

[26] H. Haken, "Analogy between higher instabilities in fluids and lasers," *Physics Letters A*, vol. 53, no. 1, pp. 77–78, may 1975.

[27] F. T. Arecchi, G. L. Lippi, G. P. Puccioni, and J. R. Tredicce, "Deterministic chaos in laser with injected signal," *Optics Communications*, vol. 51, no. 5, pp. 308–314, oct 1984.

[28] R. Broom, "Self modulation at gigahertz frequencies of a diode laser coupled to an external cavity," *Electronics Letters*, vol. 5, no. 23, p. 571, 1969.

[29] K. Konnerth and C. Lanza, "Delay between current pulse and light emission of a gallium arsenide injection laser," *Applied Physics Letters*, vol. 4, no. 7, pp. 120–121, apr 1964.

[30] T. Mukai and K. Otsuka, "New route to optical chaos: Successive-subharmonic-oscillation cascade in a semiconductor laser coupled to an external cavity," *Physical Review Letters*, vol. 55, no. 17, pp. 1711–1714, oct 1985.

[31] R. Lang and K. Kobayashi, "External optical feedback effects on semiconductor injection laser properties," *IEEE Journal of Quantum Electronics*, vol. 16, no. 3, pp. 347–355, mar 1980.

[32] C. H. Henry, "Theory of the linewidth of semiconductor lasers," *IEEE Journal of Quantum Electronics*, vol. 18, no. 2, pp. 259–264, feb 1982.

[33] J. Ohtsubo, "Semiconductor Lasers," *Fundamentals of Light Sources and Lasers*, pp. 313–325, 2004.

[34] A. Hohl and A. Gavrielides, "Bifurcation Cascade in a Semiconductor Laser Subject to Optical Feedback," *Physical Review Letters*, vol. 82, no. 6, pp. 1148–1151, feb 1999.

[35] F. Rogister, P. Mégret, O. Deparis, and M. Blondel, "Coexistence of in-phase and out-of-phase dynamics in a multimode external-cavity laser diode operating in the low-frequency fluctuations regime," *Physical Review A*, vol. 62, no. 6, p. 061803, nov 2000.

[36] A. Uchida, N. Shibasaki, S. Nogawa, and S. Yoshimori, "Transient characteristics of chaos synchronization in a semiconductor laser subject to optical feedback," *Physical Review E*, vol. 69, no. 5, p. 056201, may 2004.

[37] A. Gavrielides, T. Erneux, D. Sukow, G. Burner, T. McLachlan, J. Miller, and J. Amonette, "Square waveforms in edge-emitting diode laser subject to polarization-rotated optical feedback," in *Physics and Simulation of Optoelectronic Devices XIV*, M. Osinski, F. Henneberger, and Y. Arakawa, Eds., vol. 6115, feb 2006, p. 61150M.

[38] G. P. Agrawal and J. T. Klaus, "Effect of phase-conjugate feedback on semiconductor laser dynamics," *Optics Letters*, vol. 16, no. 17, p. 1325, sep 1991.

[39] G. H. M. van Tartwijk, H. J. C. van der Linden, and D. Lenstra, "Theory of a diode laser with phase-conjugate feedback," *Optics Letters*, vol. 17, no. 22, p. 1590, nov 1992.

[40] G. R. Gray, G. P. Agrawal, and D. H. DeTienne, "Mode locking in semiconductor lasers by phase-conjugate optical feedback," *Optics Letters*, vol. 20, no. 11, p. 1295, jun 1995.

[41] B. Krauskopf, G. R. Gray, and D. Lenstra, "Semiconductor laser with phase-conjugate feedback: Dynamics and bifurcations," *Physical Review E*, vol. 58, no. 6, pp. 7190–7197, dec 1998.

[42] W. A. van der Graaf, L. Pesquera, and D. Lenstra, "Stability of a diode laser with phase-conjugate feedback," *Optics Letters*, vol. 23, no. 4, p. 256, feb 1998.

[43] W. Van der Graaf, L. Pesquera, and D. Lenstra, "Stability and noise properties of diode lasers with phase-conjugate feedback," *IEEE Journal of Quantum Electronics*, vol. 37, no. 4, pp. 562–573, apr 2001.

[44] K. Green and B. Krauskopf, "Global bifurcations and bistability at the locking boundaries of a semiconductor laser with phase-conjugate feedback," *Physical Review E*, vol. 66, no. 1, p. 016220, jul 2002.

[45] K. Green, B. Krauskopf, and K. Engelborghs, "Bistability and torus break-up in a semiconductor laser with phase-conjugate feedback," *Physica D: Nonlinear Phenomena*, vol. 173, no. 1-2, pp. 114–129, dec 2002.

[46] K. Green, B. Krauskopf, and G. Samaey, "A Two-Parameter Study of the Locking Region of a Semiconductor Laser Subject to Phase-Conjugate Feedback," *SIAM Journal on Applied Dynamical Systems*, vol. 2, no. 2, pp. 254–276, jan 2003.

[47] J. S. Lawrence, "Diode Lasers with Optical-Feedback , Optical Injection, and Phase-Conjugate Feedback," Ph.D. dissertation, 2000.

[48] T. Erneux, A. Gavrielides, and M. Sciamanna, "Stable microwave oscillations due to external-cavity-mode beating in laser diodes subject to optical feedback," *Physical Review A*, vol. 66, no. 3, p. 033809, sep 2002.

[49] G. Friart, L. Weicker, J. Danckaert, and T. Erneux, "Relaxation and square-wave oscillations in a semiconductor laser with polarization rotated optical feedback," *Optics Express*, vol. 22, no. 6, p. 6905, 2014.

[50] D. H. DeTienne, G. R. Gray, G. P. Agrawal, and D. Lenstra, "Semiconductor laser dynamics for feedback from a finite-penetration-depth phase-conjugate mirror," *IEEE Journal of Quantum Electronics*, vol. 33, no. 5, pp. 838–844, may 1997.

[51] L. Weicker, T. Erneux, D. Wolfersberger, and M. Sciamanna, "Laser diode nonlinear dynamics from a filtered phase-conjugate optical feedback," *Physical Review E*, vol. 92, no. 2, p. 022906, aug 2015.

[52] É. Mercier, L. Weicker, D. Wolfersberger, D. M. Kane, and M. Sciamanna, "High-order external cavity modes and restabilization of a laser diode subject to a phase-conjugate feedback," *Optics Letters*, vol. 42, no. 2, p. 306, jan 2017.

[53] G. R. Gray, D. Huang, and G. P. Agrawal, "Chaotic dynamics of semiconductor lasers with phase-conjugate feedback," *Physical Review A*, vol. 49, no. 3, pp. 2096–2105, mar 1994.

[54] A. Karsaklian Dal Bosco, D. Wolfersberger, and M. Sciamanna, "Superharmonic self-pulsations from a time-delayed phase-conjugate optical system," *Applied Physics Letters*, vol. 105, no. 8, p. 081101, aug 2014.

[55] E. Bochove, "Theory of a semiconductor laser with phase-conjugate optical feedback," *Physical Review A*, vol. 55, no. 5, pp. 3891–3899, may 1997.

[56] É. Mercier, D. Wolfersberger, and M. Sciamanna, "High-frequency chaotic dynamics enabled by optical phase-conjugation," *Scientific Reports*, vol. 6, pp. 1–6, 2016.

[57] ——, "Bifurcation to chaotic low-frequency fluctuations in a laser diode with phase-conjugate feedback," *Optics Letters*, vol. 39, no. 13, p. 4021, jul 2014.

[58] T. Erneux, A. Gavrielides, K. Green, and B. Krauskopf, "External cavity modes of semiconductor lasers with phase-conjugate feedback,"

Physical Review E - Statistical Physics, Plasmas, Fluids, and Related Interdisciplinary Topics, vol. 68, no. 6, 2003.

[59] J. S. Lawrence and D. M. Kane, "Contrasting conventional optical and phase-conjugate feedback in laser diodes," *Physical Review A - Atomic, Molecular, and Optical Physics*, vol. 63, no. 3, pp. 1–10, 2001.

[60] O. K. Andersen, A. P. Fischer, I. C. Lane, E. Louvergneaux, S. Stolte, and D. Lenstra, "Experimental stability diagram of a diode laser subject to weak phase-conjugate feedback from a rubidium vapor cell," *IEEE Journal of Quantum Electronics*, vol. 35, no. 4, pp. 577–582, apr 1999.

[61] M. W. Wright and J. G. McInerney, "Injection locking semiconductor lasers with phase conjugate feedback," *Optics Communications*, vol. 110, no. 5-6, pp. 689–698, sep 1994.

[62] H. Li, T. L. Lucas, J. G. McInerney, M. W. Wright, and R. A. Morgan, "Injection locking dynamics of vertical cavity semiconductor lasers under conventional and phase conjugate injection," *IEEE Journal of Quantum Electronics*, vol. 32, no. 2, pp. 227–235, 1996.

[63] L. Weicker, D. Wolfersberger, and M. Sciamanna, "Stability analysis of a quantum cascade laser subject to phase-conjugate feedback," *Physical Review E*, vol. 98, no. 1, p. 012214, jul 2018.

[64] D. Rontani, É. Mercier, D. Wolfersberger, and M. Sciamanna, "Enhanced complexity of optical chaos in a laser diode with phase-conjugate feedback," *Optics Letters*, vol. 41, no. 20, p. 4637, 2016.

[65] M. Virte, A. Karsaklian Dal Bosco, D. Wolfersberger, and M. Sciamanna, "Chaos crisis and bistability of self-pulsing dynamics in a laser diode with phase-conjugate feedback," *Physical Review A - Atomic, Molecular, and Optical Physics*, vol. 84, no. 4, pp. 1–5, 2011.

[66] É. Mercier, C.-H. Uy, L. Weicker, M. Virte, D. Wolfersberger, and M. Sciamanna, "Self-determining high-frequency oscillation from an external-cavity laser diode," *Physical Review A*, vol. 94, no. 6, p. 061803, dec 2016.

[67] L. Weicker, C.-H. Uy, D. Wolfersberger, and M. Sciamanna, "Mapping of external cavity modes for a laser diode subject to phase-conjugate feedback," *Chaos: An Interdisciplinary Journal of Nonlinear Science*, vol. 27, no. 11, p. 114314, nov 2017.

[68] D. M. Pepper, "Nonlinear optic phase conjugation," *Optical Engineering*, vol. 21, no. 2, pp. 156–183, 1982.

[69] D. M. Pepper, D. A. Rockwell, and G. J. Dunning, "Nonlinear optic phase conjugation," *IEEE Circuits and Devices Magazine*, vol. 7, no. 5, pp. 21–34, sep 1991.

[70] A. A. Zozulya, G. Montemezzani, and D. Z. Anderson, "The Fascinating Behavior of Light in Photorefractive Media," *Optics and Photonics News*, vol. 6, no. 3, p. 6, mar 1995.

[71] G. S. He, "Optical phase conjugation: principles, techniques, and applications," *Progress in Quantum Electronics*, vol. 26, no. 3, pp. 131–191, may 2002.

[72] J.-P. Huignard and A. Brignon, *Overview of Phase Conjugation*. Hoboken, New Jersey: John Wiley & Sons, Inc., 2004, ch. 1, pp. 1–18.

[73] B. Zel'dovich, V. I. Popovichev, V. V. Ragul'skii, and F. S. Faizullov, "Connection Between the Wave Fronts of the Reflected and Exciting Light in Stimulated Mandel'shtam-Brillouin Scattering," *Soviet Journal of Experimental and Theoretical Physics Letters*, vol. 15, no. 3, pp. 109–112, 1972.

[74] B. Y. Zel'dovich, N. Mel'Nikov, N. Pilipetskiĭ, and V. V. Ragul'skii, "Observation of wave-front inversion in stimulated Raman scattering of light," *Soviet Journal of Experimental and Theoretical Physics Letters*, vol. 25, p. 36, 1977.

[75] A. D. Kudriavtseva, A. I. Sokolovskaia, J. Gazengel, N. P. Xuan, and G. Rivoire, "Reconstruction of the laser wave-front by stimulated scatterings in the pico-second range," *Optics Communications*, vol. 26, no. 3, pp. 446–448, sep 1978.

[76] A. Shiratori and M. Obara, "Frequency-stable, narrow linewidth oscillation of red diode laser with phase-conjugate feedback using stimulated photorefractive backscattering," *Applied Physics Letters*, vol. 69, no. 11, pp. 1515–1516, sep 1996.

[77] A. Yariv and D. M. Pepper, "Amplified reflection, phase conjugation, and oscillation in degenerate four-wave mixing," *Optics Letters*, vol. 1, no. 1, p. 16, jul 1977.

[78] T. Bouchet, "Non linear interaction of self-accelerating light beams," Ph.D. dissertation, Physique - Université de Lorraine, 2019, directed by par Wolfersberger, Delphine et Marsal, Nicolas. [Online]. Available: http://www.theses.fr/2019LORR0312

[79] M. Lucente, G. M. Carter, and J. G. Fujimoto, "Nonlinear mixing and phase conjugation in broad-area diode lasers," *Applied Physics Letters*, vol. 53, no. 6, pp. 467–469, 1988.

[80] P. Kürz, R. Nagar, and T. Mukai, "Highly efficient phase conjugation using spatially nondegenerate four-wave mixing in a broad-area laser diode," *Applied Physics Letters*, vol. 68, no. 9, pp. 1180–1182, feb 1996.

[81] E. Gehrig and O. Hess, "Ultrafast active phase conjugation in broad-area semiconductor laser amplifiers," *Journal of the Optical Society of America B*, vol. 18, no. 7, p. 1036, jul 2001.

[82] J. Kaiser, I. Fischer, W. Elsäßer, E. Gehrig, and O. Hess, "Spatially resolved femtosecond pump-probe spectroscopy in broad-area semiconductor lasers," *IEEE Journal of Quantum Electronics*, vol. 42, no. 4, pp. 363–371, 2006.

[83] P. Kürz and T. Mukai, "Frequency stabilization of a semiconductor laser by external phase-conjugate feedback." *Optics letters*, vol. 21, no. 17, pp. 1369–71, 1996.

[84] J. Feinberg, "Self-pumped, continuous-wave phase conjugator using internal reflection," *Optics Letters*, vol. 7, no. 10, p. 486, 1982.

[85] ——, "Asymmetric self-defocusing of an optical beam from the photorefractive effect," *Journal of the Optical Society of America*, vol. 72, no. 1, p. 46, jan 1982.

[86] D. J. Gauthier, P. Narum, and R. W. Boyd, "Observation of deterministic chaos in a phase-conjugate mirror," *Physical Review Letters*, vol. 58, no. 16, pp. 1640–1643, 1987.

[87] T. Rauch, C. Denz, and T. Tschudi, "Analysis of irregular fluctuations in a self-pumped BaTiO3phase-conjugate mirror," *Optics Communications*, vol. 88, no. 2-3, pp. 160–166, 1992.

[88] P. M. Jeffrey and R. W. Eason, "Lyapunov exponent analysis of irregular fluctuations in a mirror , establishing transition to chaotic behavior," *Optical Society of America.*, vol. 11, no. 3, pp. 476–480, 1994.

[89] M. Goetz, J.-M. Vanzo, and G. Kugel, "Temporal behaviour of the phase conjugate wave obtained by means of a BaTiO3crystal in a CAT configuration," *Optical Materials*, vol. 4, no. 2-3, pp. 308–313, 1995.

[90] S. Itoh, Y. Uesu, N. Oh-hori, and S. Odoulov, "Reduction of the specular reflectivity from Feinberg's Cat conjugator operating in auto-oscillation mode," *Applied Physics B: Lasers and Optics*, vol. 68, no. 5, pp. 953–957, may 1999.

[91] Y. Zheng, A. Sasaki, X. Gao, and H. Aoyama, "Origin and elimination of dynamic instability in a self-pumped phase-conjugate mirror." *Optics letters*, vol. 20, no. 3, pp. 267–9, 1995.

[92] H. Zhang, X. H. He, E. Chen, Y. Liu, S. H. Tang, D. Shen, and D. Jiang, "High-reflectivity self-pumped phase conjugator using total internal reflection in KNbNO 3 :Fe," *Applied Physics Letters*, vol. 57, no. 13, pp. 1298–1300, sep 1990.

[93] C. Medrano, M. Zgonik, S. Berents, P. Bernasconi, and P. Günter, "Self-pumped and incoherent phase conjugation in Fe-doped KNbO_3," *Journal of the Optical Society of America B*, vol. 11, no. 9, p. 1718, 1994.

[94] D. Rytz, M. S. Keirstead, T. M. Baer, R. R. Stephens, and B. A. Wechsler, "Efficient self-pumped phase conjugation at near-infrared wavelengths using cobalt-doped BaTiO_3," *Optics Letters*, vol. 15, no. 22, p. 1279, nov 1990.

[95] N. Huot, J.-M. C. Jonathan, G. Pauliat, D. Rytz, and G. Roosen, "Self-pumped phase conjugate BaTiO 3 :Rh ring mirror at 1.06 μm: optimization of reflectivity, rise time, and fidelity," F. T. S. Yu and S. Yin, Eds., vol. 3470, no. July, oct 1998, p. 8.

[96] H. Kröse, R. Scharfschwerdt, O. F. Schirmer, and H. Hesse, "Light-induced charge transport in BaTiO3 via three charge states of rhodium," *Applied Physics B Laser and Optics*, vol. 61, no. 1, pp. 1–7, jul 1995.

[97] D. Rytz, B. A. Wechsler, M. H. Garrett, C. C. Nelson, and R. N. Schwartz, "Photorefractive properties of BaTiO_3:Co," *Journal of the Optical Society of America B*, vol. 7, no. 12, p. 2245, dec 1990.

[98] P. Günter, E. Voit, M. Zha, and J. Albers, "Self-pulsation and optical chaos in self-pumped photorefractive BaTiO3," *Optics Communications*, vol. 55, no. 3, pp. 210–214, sep 1985.

[99] G. Bouchez, C.-H. Uy, B. Macias, D. Wolfersberger, and M. Sciamanna, "Wideband chaos from a laser diode with phase-conjugate feedback," *Optics Letters*, vol. 44, no. 4, p. 975, feb 2019.

[100] G. Bouchez, D. Wolfersberger, and M. Sciamanna, "Breaking the Limit of Laser Chaos Bandwidth using Phase Conjugate Feedback," in *2019 Conference on Lasers and Electro-Optics Europe & European Quantum Electronics Conference (CLEO/Europe-EQEC)*, vol. 151162, no. 2015. IEEE, jun 2019, pp. 1–1.

[101] ——, "High-frequency chaotic dynamics of laser diodes with long phase-conjugate feedback." European Semiconductor Laser Workshop 2019, sept 2019.

[102] T. Malica, G. Bouchez, D. Wolfersberger, and M. Sciamanna, "Spatiotemporal complexity of chaos in a phase-conjugate feedback laser system," *Optics Letters*, vol. 45, no. 4, p. 819, 2020.

[103] G. Bouchez, T. Malica, D. Wolfersberger, and M. Sciamanna, "Optimized properties of chaos from a laser diode," *Physical Review E*, vol. 103, no. 4, p. 042207, apr 2021.

[104] A. Karsaklian Dal Bosco, D. Wolfersberger, and M. Sciamanna, "Delay-induced deterministic resonance of chaotic dynamics," *EPL (Europhysics Letters)*, vol. 101, no. 2, p. 24001, jan 2013.

[105] ——, "Extreme events in time-delayed nonlinear optics," *Optics Letters*, vol. 38, no. 5, p. 703, 2013.

[106] É. Mercier, "High-frequency nonlinear dynamics of a laser diode with phase conjugate feedback," Ph.D. dissertation, CentraleSupélec, 2016.

[107] G. Bouchez, T. Malica, D. Wolfersberger, and M. Sciamanna, "Manipulating the chaos bandwidth of a semiconductor laser subjected to phase-conjugate feedback," in *Semiconductor Lasers and Laser Dynamics IX*, K. Panajotov, M. Sciamanna, R. Michalzik, and S. Höfling, Eds. SPIE, apr 2020, p. 36.

[108] K. Hirano, K. Amano, A. Uchida, S. Naito, M. Inoue, S. Yoshimori, K. Yoshimura, and P. Davis, "Characteristics of Fast Physical Random Bit Generation Using Chaotic Semiconductor Lasers," *IEEE Journal of Quantum Electronics*, vol. 45, no. 11, pp. 1367–1379, nov 2009.

[109] N. Oliver, T. Jüngling, and I. Fischer, "Consistency Properties of a Chaotic Semiconductor Laser Driven by Optical Feedback," *Physical Review Letters*, vol. 114, no. 12, p. 123902, mar 2015.

[110] A. Uchida, T. Heil, P. Davis, and T. Aida, "High-frequency broad-band signal generation using a semiconductor laser with a chaotic optical injection," *IEEE Journal of Quantum Electronics*, vol. 39, no. 11, pp. 1462–1467, 2003.

[111] F.-Y. Lin and J. M. Liu, "Chaotic Lidar," *IEEE Journal of Selected Topics in Quantum Electronics*, vol. 10, no. 5, pp. 991–997, sep 2004.

[112] F.-Y. Lin, Y.-K. Chao, and T.-C. Wu, "Effective Bandwidths of Broadband Chaotic Signals," *IEEE Journal of Quantum Electronics*, vol. 48, no. 8, pp. 1010–1014, aug 2012.

[113] F.-Y. Lin and J. M. Liu, "Nonlinear dynamical characteristics of an optically injected semiconductor laser subject to optoelectronic feedback," *Optics Communications*, vol. 221, no. 1-3, pp. 173–180, 2003.

[114] R. Sakuraba, K. Iwakawa, K. Kanno, and A. Uchida, "Tb/s physical random bit generation with bandwidth-enhanced chaos in three-cascaded semiconductor lasers," *Optics Express*, vol. 23, no. 2, p. 1470, jan 2015.

[115] A. Zhao, N. Jiang, S. Liu, C. Xue, J. Tang, and K. Qiu, "Wideband complex-enhanced chaos generation using a semiconductor laser subject to delay-interfered self-phase-modulated feedback," *Optics Express*, vol. 27, no. 9, p. 12336, 2019.

[116] K. Schires, S. Gomez, A. Gallet, G.-h. Duan, and F. Grillot, "Passive Chaos Bandwidth Enhancement Under Dual-Optical Feedback with Hybrid III–V/Si DFB Laser," *IEEE Journal of Selected Topics in Quantum Electronics*, vol. 23, no. 6, pp. 1–9, nov 2017.

[117] A.-B. Wang, Y.-C. Wang, and J.-f. Wang, "Route to broadband chaos in a chaotic laser diode subject to optical injection," *Optics Letters*, vol. 34, no. 8, p. 1144, 2009.

[118] M. Zhang, T. Liu, P. Li, A.-B. Wang, J. Zhang, and Y. Wang, "Generation of broadband chaotic laser using dual-wavelength optically injected Fabry-Pérot laser diode with optical feedback," *IEEE Photonics Technology Letters*, vol. 23, no. 24, pp. 1872–1874, 2011.

[119] L. Qiao, T. Lv, Y. Xu, M. Zhang, J. Zhang, T. Wang, R. Zhou, Q. Wang, and H. Xu, "Generation of flat wideband chaos based on mutual injection of semiconductor lasers," *Optics Letters*, vol. 44, no. 22, p. 5394, nov 2019.

[120] Y. Wang, Z. Jia, Z. Gao, J. Xiao, L. Wang, Y. Wang, Y. Huang, and A. Wang, "Generation of laser chaos with wide-band flat power spectrum in a circular-side hexagonal resonator microlaser with optical feedback," *Optics Express*, vol. 28, no. 12, p. 18507, jun 2020.

[121] Q. Yang, L. Qiao, M. Zhang, J. Zhang, T. Wang, S. Gao, M. Chai, and P. Menjabin Mohiuddin, "Generation of a broadband chaotic laser by active optical feedback loop combined with a high nonlinear fiber," *Optics Letters*, vol. 45, no. 7, p. 1750, 2020.

[122] R. Takahashi, Y. Akizawa, A. Uchida, T. Harayama, K. Tsuzuki, S. Sunada, K. Arai, K. Yoshimura, and P. Davis, "Fast physical random bit generation with photonic integrated circuits with different external cavity lengths for chaos generation," *Optics Express*, vol. 22, no. 10, p. 11727, may 2014.

[123] A. Gray and J. Markel, "A spectral-flatness measure for studying the autocorrelation method of linear prediction of speech analysis," *IEEE Transactions on Acoustics, Speech, and Signal Processing*, vol. 22, no. 3, pp. 207–217, jun 1974.

[124] J.-G. Wu, G.-Q. Xia, and Z.-M. Wu, "Suppression of time delay signatures of chaotic output in a semiconductor laser with double optical feedback," *Optics Express*, vol. 17, no. 22, p. 20124, oct 2009.

[125] D. Rontani, A. Locquet, M. Sciamanna, and D. S. Citrin, "Loss of time-delay signature in the chaotic output of a semiconductor laser with optical feedback," *Optics Letters*, vol. 32, no. 20, p. 2960, oct 2007.

[126] T. Malica, G. Bouchez, D. Wolfersberger, and M. Sciamanna, "Evolution of the spatiotemporal complexity in a phase-conjugate feedback laser system," in *Semiconductor Lasers and Laser Dynamics IX*, K. Panajotov, M. Sciamanna, R. Michalzik, and S. Höfling, Eds., no. April. SPIE, apr 2020, p. 37.

[127] C. Bandt and B. Pompe, "Permutation Entropy: A Natural Complexity Measure for Time Series," *Physical Review Letters*, vol. 88, no. 17, p. 174102, apr 2002.

[128] C. E. Shannon, "A Mathematical Theory of Communication," *Bell System Technical Journal*, vol. 27, no. 3, pp. 379–423, jul 1948.

[129] M. Staniek and K. Lehnertz, "Parameter selection for permutation entropy measurements," *International Journal of Bifurcation and Chaos*, vol. 17, no. 10, pp. 3729–3733, oct 2007.

[130] M. Riedl, A. Müller, and N. Wessel, "Practical considerations of permutation entropy: A tutorial review," *European Physical Journal: Special Topics*, vol. 222, no. 2, pp. 249–262, 2013.

[131] M. Zanin, L. Zunino, O. A. Rosso, and D. Papo, "Permutation Entropy and Its Main Biomedical and Econophysics Applications: A Review," *Entropy*, vol. 14, no. 8, pp. 1553–1577, aug 2012.

[132] X. Li, G. Ouyang, and D. A. Richards, "Predictability analysis of absence seizures with permutation entropy," *Epilepsy Research*, vol. 77, no. 1, pp. 70–74, oct 2007.

[133] D. Jordan, G. Stockmanns, E. F. Kochs, S. Pilge, and G. Schneider, "Electroencephalographic Order Pattern Analysis for the Separation of Consciousness and Unconsciousness," *Anesthesiology*, vol. 109, no. 6, pp. 1014–1022, dec 2008.

[134] C. Bian, C. Qin, Q. D. Y. Ma, and Q. Shen, "Modified permutation-entropy analysis of heartbeat dynamics," *Physical Review E*, vol. 85, no. 2, p. 021906, feb 2012.

[135] L. Zunino, B. M. Tabak, F. Serinaldi, M. Zanin, D. G. Pérez, and O. A. Rosso, "Commodity predictability analysis with a permutation information theory approach," *Physica A: Statistical Mechanics and its Applications*, vol. 390, no. 5, pp. 876–890, mar 2011.

[136] L. Zunino, M. Zanin, B. M. Tabak, D. G. Pérez, and O. A. Rosso, "Forbidden patterns, permutation entropy and stock market inefficiency," *Physica A: Statistical Mechanics and its Applications*, vol. 388, no. 14, pp. 2854–2864, jul 2009.

[137] P. M. Saco, L. C. Carpi, A. Figliola, E. Serrano, and O. A. Rosso, "Entropy analysis of the dynamics of El Niño/Southern Oscillation during the

Holocene," *Physica A: Statistical Mechanics and its Applications*, vol. 389, no. 21, pp. 5022–5027, nov 2010.

[138] C. Bandt, "Ordinal time series analysis," *Ecological Modelling*, vol. 182, no. 3-4, pp. 229–238, mar 2005.

[139] Y. Cao, W.-w. Tung, J. B. Gao, V. A. Protopopescu, and L. M. Hively, "Detecting dynamical changes in time series using the permutation entropy," *Physical Review E*, vol. 70, no. 4, p. 046217, oct 2004.

[140] M. C. Soriano, L. Zunino, O. A. Rosso, I. Fischer, and C. R. Mirasso, "Time Scales of a Chaotic Semiconductor Laser With Optical Feedback Under the Lens of a Permutation Information Analysis," *IEEE Journal of Quantum Electronics*, vol. 47, no. 2, pp. 252–261, feb 2011.

[141] V. S. Udaltsov, L. Larger, J.-P. Goedgebuer, A. Locquet, and D. S. Citrin, "Time delay identification in chaotic cryptosystems ruled by delay-differential equations," *Journal of Optical Technology*, vol. 72, no. 5, p. 373, may 2005.

[142] O. A. Rosso, R. Vicente, and C. R. Mirasso, "Encryption test of pseudo-aleatory messages embedded on chaotic laser signals: An information theory approach," *Physics Letters A*, vol. 372, no. 7, pp. 1018–1023, feb 2008.

[143] S. Xiang, W. Pan, B. Luo, L. Yan, X. Zou, N. Jiang, L. Yang, and H. Zhu, "Conceal time-delay signature of chaotic vertical-cavity surface-emitting lasers by variable-polarization optical feedback," *Optics Communications*, vol. 284, no. 24, pp. 5758–5765, dec 2011.

[144] J.-G. Wu, Z.-M. Wu, G.-Q. Xia, and G.-Y. Feng, "Evolution of time delay signature of chaos generated in a mutually delay-coupled semiconductor lasers system," *Optics Express*, vol. 20, no. 2, p. 1741, jan 2012.

[145] L. J. Quintero-Rodríguez, I. E. Zaldívar-Huerta, Y. Hong, C. Masoller, and M. W. Lee, "Permutation entropy analysis of the output of a laser diode under stimulated Brillouin scattering optical feedback," *Optics Express*, vol. 29, no. 17, p. 26787, aug 2021.

[146] J. Tiana-Alsina, J. M. Buldú, M. C. Torrent, and J. García-Ojalvo, "Quantifying stochasticity in the dynamics of delay-coupled semiconductor lasers via forbidden patterns," *Philosophical Transactions of the Royal Society A: Mathematical, Physical and Engineering Sciences*, vol. 368, no. 1911, pp. 367–377, jan 2010.

[147] J. Tiana-Alsina, M. C. Torrent, O. A. Rosso, C. Masoller, and J. Garcia-Ojalvo, "Quantifying the statistical complexity of low-frequency fluctuations in semiconductor lasers with optical feedback," *Physical Review A*, vol. 82, no. 1, p. 013819, jul 2010.

[148] J. P. Toomey and D. M. Kane, "Mapping the dynamic complexity of a semiconductor laser with optical feedback using permutation entropy," *Optics Express*, vol. 22, no. 2, p. 1713, jan 2014.

[149] K. Ikeda, K. Kondo, and O. Akimoto, "Successive higher-harmonic bifurcations in systems with delayed feedback," *Physical Review Letters*, vol. 49, no. 20, pp. 1467–1470, 1982.

[150] D. Pieroux, T. Erneux, B. Haegeman, K. Engelborghs, and D. Roose, "Bridges of Periodic Solutions and Tori in Semiconductor Lasers Subject to Delay," *Physical Review Letters*, vol. 87, no. 19, p. 193901, oct 2001.

[151] A. A. Tager and K. Petermann, "High-Frequency Oscillations and Self-Mode Locking in Short External-Cavity Laser Diodes," *IEEE Journal of Quantum Electronics*, vol. 30, no. 7, pp. 1553–1561, 1994.

[152] F. A. Hopf, D. L. Kaplan, H. M. Gibbs, and R. L. Shoemaker, "Bifurcations to chaos in optical bistability," *Physical Review A*, vol. 25, no. 4, pp. 2172–2182, apr 1982.

[153] I. Fischer, O. Hess, W. Elsässer, and E. Göbel, "High-Dimensional Chaotic Dynamics of an External Cavity Semiconductor Laser," *Physical Review Letters*, vol. 73, no. 16, pp. 2188–2191, oct 1994.

[154] W. Loh and C. Tang, "Successive higher-harmonic bifurcations of a polarization self-modulated external cavity semiconductor laser," *Optics Communications*, vol. 85, no. 2-3, pp. 283–290, sep 1991.

[155] C.-H. Uy, L. Weicker, D. Rontani, and M. Sciamanna, "Sustained oscillations accompanying polarization switching in laser dynamics," *Optics Express*, vol. 26, no. 13, p. 16917, jun 2018.

[156] K. Vahala, K. Kyuma, A. Yariv, S. Kwong, M. Cronin-Golomb, and K. Y. Lau, "Narrow linewidth, single frequency semiconductor laser with a phase conjugate external cavity mirror," *Applied Physics Letters*, vol. 49, no. 23, pp. 1563–1565, dec 1986.

[157] I. Hayashi, M. B. Panish, and F. K. Reinhart, "GaAs-AlxGa1-xAs double heterostructure injection lasers," *Journal of Applied Physics*, vol. 42, no. 5, pp. 1929–1941, 1971.

[158] W. H. Loh, Y. Ozeki, and C. L. Tang, "High-frequency polarization self-modulation and chaotic phenomena in external cavity semiconductor lasers," *Applied Physics Letters*, vol. 56, no. 26, pp. 2613–2615, jun 1990.

[159] M. Sciamanna, T. Erneux, F. Rogister, O. Deparis, P. Mégret, and M. Blondel, "Bifurcation bridges between external-cavity modes lead to polarization self-modulation in vertical-cavity surface-emitting lasers," *Physical Review A*, vol. 65, no. 4, p. 041801, apr 2002.

[160] J. Miller, T. Erneux, G. Burner, T. McLachlan, D. W. Sukow, A. Gavrielides, and J. Amonette, "Square-wave self-modulation in diode lasers with polarization-rotated optical feedback," *Optics Letters*, vol. 31, no. 13, p. 2006, 2006.

[161] T. Heil, I. Fischer, W. Elsäßer, B. Krauskopf, K. Green, and A. Gavrielides, "Delay dynamics of semiconductor lasers with short external cavities: Bifurcation scenarios and mechanisms," *Physical Review E*, vol. 67, no. 6, p. 066214, jun 2003.

[162] G. Friart, G. Verschaffelt, J. Danckaert, and T. Erneux, "All-optical controlled switching between time-periodic square waves in diode lasers with delayed feedback," *Optics Letters*, vol. 39, no. 21, p. 6098, nov 2014.